

Carnegie Mellon University  
CARNEGIE INSTITUTE OF TECHNOLOGY

**THESIS**

SUBMITTED IN PARTIAL FULFILLMENT OF THE REQUIREMENTS  
FOR THE DEGREE OF: **DOCTOR OF PHILOSOPHY**

**TITLE**

---

---

**PRESENTED BY**

---

**ACCEPTED BY THE DEPARTMENT OF**

---

\_\_\_\_\_  
ADVISOR, MAJOR PROFESSOR

\_\_\_\_\_  
DATE

\_\_\_\_\_  
DEPARTMENT HEAD

\_\_\_\_\_  
DATE

**APPROVED BY THE COLLEGE COUNCIL**

\_\_\_\_\_  
DEAN

\_\_\_\_\_  
DATE

**On nondiffusive thermal transport and phonon mean-free-path-dependent  
contributions to thermal conductivity**

Submitted in partial fulfillment of the requirements for  
the degree of  
Doctor of Philosophy  
in  
Mechanical Engineering

Keith T. Regner

B.S., Mechanical Engineering, Virginia Polytechnic Institute and State University

M.S., Mechanical Engineering, Virginia Polytechnic Institute and State University

Carnegie Mellon University  
Pittsburgh, PA

January 2016

## **ACKNOWLEDGMENTS**

I thank my advisor Prof. Jon Malen for being a committed teacher, dedicated advisor, helpful mentor, exemplary role model, and friend. I thank Prof. Alan McGaughey for his support and helpful input and feedback in various projects and situations. I also thank Prof. Elias Towe in the Electrical and Computer Engineering and Materials Science and Engineering Departments at Carnegie Mellon University and Prof. Chris Dames in the Mechanical Engineering Department at University of California, Berkeley for serving on my committee.

I thank Dr. Zonghui Su, Dr. Daniel Sellan, Prof. Cristina Amon, Shubhadiya Majumdar, Justin Freedman, and Lien Chin Wei for their contributions to our publications and acknowledge the financial support of the NSF (CAREER Award no. ENG-1149374 and GOALI CBET Thermal Transport Processes Award no. 1133394) and the Army Research Office (Physical Properties of Materials Award no. W911NF-14-0350). I also thank the staff at Carnegie Mellon University for their assistance and guidance, specifically in the Nanofabrication Facility, Materials Characterization Facility, and Mechanical Engineering Machine Shop.

Finally, I thank my lab mates from the Malen and McGaughey groups for providing a collaborative and encouraging environment and my friends and family, specifically my mom and dad, for their love and support.

# On nondiffusive thermal transport and phonon mean-free-path-dependent contributions to thermal conductivity

Keith T. Regner

## ABSTRACT

Nondiffusive thermal transport occurs when length or time scales of a system are on the order of the mean free paths (MFPs) or lifetimes of the energy carriers. As a result, a local equilibrium temperature cannot be defined and the thermal transport properties of the system can no longer be taken as the bulk values. When system boundaries are decreased below energy carrier MFPs, nondiffusive transport can be described with a reduced, effective thermal conductivity. Heat dissipation in light emitting diodes and transistors is adversely impacted by reductions in thermal conductivity, while thermoelectric energy conversion devices benefit. In my PhD, I studied the physics governing nondiffusive thermal transport.

In this dissertation I describe my contributions in nondiffusive thermal transport to the scientific community. First, I describe the development of broadband frequency domain thermorefectance (BB-FDTR), an experimental technique used to observe nondiffusive thermal transport in materials by creating length scales comparable to energy carrier MFPs. I use BB-FDTR to induce nondiffusive thermal transport in Si-based materials at device operating temperatures. I relate my measurements to the thermal conductivity accumulation function, a fundamental physical quantity that describes cumulative contributions to thermal conductivity from energy carriers with different MFPs. Using a first order interpretation of my data I show that  $40\pm 5\%$  of the thermal conductivity of crystalline silicon at a temperature of 311 K comes from phonons with  $\text{MFP} > 1 \mu\text{m}$ . Additional BB-FDTR measurements on a 500 nm thick amorphous silicon film indicate propagating phonon-like modes that contribute more than  $35\pm 7\%$  to thermal conductivity at a temperature of 306 K, despite atomic disorder.

I also describe the development of multiple models that are used to refine the interpretation of BB-FDTR measurements and better understand nondiffusive thermal transport measurements. First, I

solve the Boltzmann transport equation (BTE) analytically to explain how and why measurements of thermal conductivity change as a function of experimental length scales in BB-FDTR. My solution incorporates two experimentally defined length scales: thermal penetration depth and heating laser spot radius. Comparison of the BTE result with that from conventional heat diffusion theory enables a mapping of MFP-specific contributions to the measured thermal conductivity based on the experimental length scales. The result is used to re-interpret nondiffusive thermal conductivity measurements of silicon with first principles-based calculations of its thermal conductivity accumulation function.

Next, I develop a solution to the two-temperature diffusion equation in axisymmetric cylindrical coordinates to model heat transport in thermoreflectance experiments. The solution builds upon prior solutions that account for two-channel diffusion in each layer of an N-layered geometry, but adds the ability to deposit heat at any location within each layer. I use this solution to account for non-surface heating in the transducer layer of thermoreflectance experiments that challenge the timescales of electron-phonon coupling. I use the model to refit BB-FDTR measurements of silicon and conclude that spectrally dependent phonon transmission at the transducer/silicon interface affects the shape of the measured accumulation function.

Finally, I extend my solution to the BTE to a practical application: resistive-switching memory (RRAM). I model thermal transport in RRAM in the set state where the conductive filament (CF) is approximated by an infinitely long cylinder embedded in crystalline rutile  $\text{TiO}_2$ , a prototypical RRAM material. I determine the phonon MFP spectrum in  $\text{TiO}_2$  and find that MFPs are similar to the CF radius, indicating thermal transport is nondiffusive. I develop an analytical solution to the BTE to model the nondiffusive thermal transport in the  $\text{TiO}_2$  and find that the surface temperature rise of the CF predicted by the BTE is larger than that predicted by the heat diffusion equation (e.g.,  $5\times$  larger for a 1 nm CF radius in a device at a temperature of 300 K). To model thermal transport in RRAM with the heat diffusion equation, I propose a suppressed, effective  $\text{TiO}_2$  thermal conductivity to more accurately predict the CF temperature.

# TABLE OF CONTENTS

LIST OF TABLES .....	vii
LIST OF FIGURES AND ILLUSTRATIONS .....	viii
1. INTRODUCTION .....	1
I. Thermal conductivity accumulation function.....	2
A. Mathematical description.....	2
B. $k_{\text{accum}}$ for Debye dispersion and power law scattering .....	4
C. Theoretical prediction of phonon mode properties and $k_{\text{accum}}$ .....	5
II. Experimental methods to measure $k_{\text{accum}}$ .....	6
A. Transient thermal grating.....	7
B. Time domain thermoreflectance .....	8
C. Broadband frequency domain thermoreflectance .....	9
D. Comparison of techniques .....	10
III. Relating $k_{\text{exp}}$ and $k_{\text{accum}}$ .....	11
A. Step function suppression function.....	12
B. Experiment-specific suppression function from the BTE.....	13
IV. Importance of $k_{\text{accum}}$ .....	16
A. Universality of $k_{\text{accum}}$ .....	17
B. Applying bulk $k_{\text{accum}}$ measurements to nanostructures.....	17
V. Organization of the dissertation .....	18
2. BROADBAND FREQUENCY DOMAIN THERMOREFLECTANCE .....	20
I. Overview .....	20
II. Experimental setup.....	21
A. Sample preparation .....	28
B. Determining pump and probe laser spot size.....	29
III. Analytical modeling.....	30
A. Planar heating on a semi-infinite medium .....	30
B. Planar heating in a layered sample.....	33
C. Including spatially Gaussian surface heating.....	35
D. Sensitivity .....	37
IV. Fitting BB-FDTR data with the heat diffusion equation .....	39
A. Fitting procedure.....	40
B. Effect of fitting window size .....	42
C. Uncertainty in $k$ vs. $L_p$ measurements.....	43
V. Summary.....	44
3. NONDIFFUSIVE THERMAL TRANSPORT IN Si-BASED MATERIALS.....	46
I. Overview .....	46
II. Sample preparation .....	47
A. Transducer layer .....	48
B. Amorphous silicon.....	49
III. Heating frequency dependent thermal conductivity .....	50
A. Modeling the diffusive to ballistic transition.....	52
B. Experimental phonon mean free path spectra.....	54
C. Temperature-dependent MFP spectra in c-Si .....	57
IV. Summary.....	59
4. INTERPRETING NONDIFFUSIVE BB-FDTR MEASUREMENTS WITH THE BTE .....	65
I. Overview .....	65

II.	Suppression function in a planar geometry .....	66
III.	Suppression function in a spherical geometry .....	75
IV.	Relating experiments and $k_{\text{accum}}$ using the suppression function .....	81
V.	Summary .....	85
5.	ELECTRON-PHONON NON-EQUILIBRIUM IN THE TRANSDUCER .....	87
I.	Overview .....	87
II.	Two-temperature formulation .....	88
III.	Sensitivity analysis .....	98
IV.	Fitting BB-FDTR data .....	105
V.	Summary .....	113
6.	APPLYING THE BOLTZMANN TRANSPORT EQUATION TO RRAM .....	114
I.	Overview .....	114
II.	Phonon mean free path spectrum in $\text{TiO}_2$ .....	115
III.	Analytical solution to the Boltzmann transport equation .....	116
IV.	Effective thermal conductivity in RRAM .....	118
V.	Predicting conductive filament temperature .....	119
VI.	Summary .....	120
7.	OUTLOOK AND CONCLUSION .....	121
I.	Direct interpretation of experiments using the BTE .....	121
II.	Clarifying the role of the transducer/interface .....	122
III.	Alloys and nanograined materials .....	124
IV.	Electron-dominated materials .....	125
V.	Beyond 3-D materials .....	125
VI.	Conclusion .....	127
	REFERENCES .....	128

## LIST OF TABLES

Table 1.1. Advantages and disadvantages of the techniques outlined to measure $k_{\text{exp}}$ vs. $L_c$ . .....	11
Table 2.1. Component list for schematics in Fig. 2.1. ....	23
Table 2.2. Nominal values for fitting and the sensitivity analysis and the uncertainty ranges used to generate the shaded error regions in Fig. 2.7. ....	38
Table 3.1. Phase lag data from BB-FDTR experiments shown with constant $k$ fits, and the parameters used in the fits for each sample. ....	60
Table 5.1. Nominal values for the parameters used in the sensitivity analysis. ....	99
Table 5.2. Room temperature values of “consistent parameters” used in the modeling/fitting of data for each sample measured. Italicized parameters are the transducer parameters that differ between “consistent parameters” and “best-fit parameters” for SiO <sub>2</sub> and platinum. ....	108

## LIST OF FIGURES AND ILLUSTRATIONS

Fig. 1.1. Thermal conductivity accumulation functions for silicon at $T = 300$ K ( $k_{\text{bulk}} = 145$ W/m-K) from the gray model [41], BvKS model [38], Holland model [44], Eq. (1.7), first principles [45], and molecular dynamics [37]. These data were previously compiled by Yang and Dames [41].	5
Fig. 1.2. Schematics highlighting $L_c$ (as $L_g$ , $L_p$ , or $r_o$ ) in (a) transient thermal grating (b) time domain thermorefectance and (c) broadband frequency domain thermorefectance. These three techniques are used to measure thermal conductivity $k_{\text{exp}}$ as a function of the relevant experimental length scales $L_c$ indicated in the figure.	7
Fig. 1.3. Suppression functions derived for TTG, TDTR, and BB-FDTR. These are used in Eq. (1.8) to interpret measurements of $k_{\text{exp}}$ vs. $L_c$ . Also shown is the step function interpretation from Eq. (1.9).	16
Fig. 2.1. (a) Schematic of traditional FDTR. (b) Schematic of BB-FDTR. The pump beam undergoes intensity modulation at frequency $f_1$ and gets focused on the sample. EOM2 induces an additional modulation in the reflected probe beam, heterodyning the thermal signal, allowing for higher heating frequencies at a lower measuring frequency, increasing the measurement range of $k_{\text{accum}}$ . (c) Schematic of BB-FDTR with alternate location for EOM2. In this configuration, the heterodyning occurs at the sample surface but the thermal phase response cannot be isolated. Labels identifying the make and models of the components can be found in Table 2.1.	22
Fig. 2.2. Normalized temperature and phase response from traditional FDTR with an unamplified photo diode from 200 kHz to 200 MHz and an amplified photo diode up to the bandwidth of the photo diode and BB-FDTR experiments with an amplified photo diode for c-Si at $T = 311$ K. In the low frequency regime, the data from traditional FDTR and BB-FDTR are the same and indicate no effect from using different photo diodes. As the frequency increases ( $f_1 > 20$ MHz), signal to noise ratios decrease in traditional FDTR. Heterodyning the signal allows for large signal to noise ratios up to a heating frequency of 200 MHz.	27
Fig. 2.3. A knife-edge is used to determine the beam profile. The data are fit with a cumulative normal distribution function to find the $1/e^2$ radius of the pump and probe beams. These values are used to find the effective spot size $r_{\text{spot}}$ .	30
Fig. 2.4. Semi-infinite slab with thermal conductivity $k$ and volumetric heat capacity $C$ subject to a planar, periodic surface heat flux.	31
Fig. 2.5. N-layered material with each layer having thermal conductivity, heat capacity, and thickness $k_n$ , $C_n$ , and $t_n$ subject to periodic, planar surface heating. An interface conductance $G_n$ exists between layers $n$ and $n+1$ .	33
Fig. 2.6. (a) Sensitivity to a 1% change in nominal parameters found in Table 2.2, as defined by Eq. (2.20). The effect on the sensitivity from (b) decreased interface thermal conductance and (c) decreased substrate thermal conductivity.	39
Fig. 2.7. (a) The phase response data are divided into different windows. Each window is fit to a value of thermal conductivity and plotted at the median frequency of that fitting range. (b) The fitted thermal conductivity and median frequency for each window is used to generate the $k$ vs. $L_p$ .	42
Fig. 2.8. $k$ vs. $L_p$ for intrinsic c-Si ( $T = 311$ K) is shown for 7-point, 13-point, and 19-point fitting windows. Increasing the window size decreases the range of $L_p$ . Relative to the 13-point fits, fitting windows of 7 and 19 points do not change the shape of $k$ vs. $L_p$ .	43
Fig. 2.9. $k$ vs. $L_p$ for c-Si at $T = 311$ K is shown with a $\pm 0.2^\circ$ constant phase shift in the measured phase response. The largest effect comes at longer $L_p$ , with a maximum $\pm 3\%$ deviation from the original $k$ vs. $L_p$ .	44

Fig. 3.1. Fitting the measured XRR data yield values of 8 nm and 54 nm for the chromium adhesion layer and the gold layer on c-Si. .... 49

Fig. 3.2. Theta/2theta XRD scans on an a-Si film on a c-Si substrate and a blank c-Si substrate. The broad hump in the a-Si scan verifies the amorphicity of the a-Si film. .... 50

Fig. 3.3. a) Phase-lag vs. modulation frequency data for intrinsic c-Si and SiO<sub>2</sub> shown with a constant thermal conductivity fit over the entire experimental frequency range. Fitting SiO<sub>2</sub> yields a thermal conductivity value of 1.4±0.2 W/m-K, and window fitting produces a heating frequency-independent thermal conductivity. Fitting c-Si over the entire frequency range yields a fitted thermal conductivity below bulk (99±6 W/m-K) and window fitting shows a modulation frequency-dependent thermal conductivity. b) Illustration of diffusive and ballistic transport. At low heating frequencies, when the thermal penetration depth is greater than the phonon MFPs, there is diffusive thermal transport and a bulk value of thermal conductivity is measured. At high heating frequencies, the thermal penetration depth decreases below the MFPs of some phonons, which travel ballistically through the thermally affected zone (white arrows). These ballistic phonons do not contribute to the measured value of thermal conductivity..... 51

Fig. 3.4. a) Spatial variation of the temperature oscillation amplitude for diffusive transport [corresponding to the lowest heating frequency in (b) and (c)] and ballistic transport [corresponding to the highest heating frequency in (b) and (c)] from the Fourier law (dashed line) and from the lattice Boltzmann method solution to the BTE for a gray material (solid line), all for a periodic surface heat flux. b) Amplitude of the surface temperature oscillation and c) perceived thermal conductivity plotted vs. normalized penetration depth. When  $L_p > \text{MFP}$ , the Fourier and BTE predictions match and BB-FDTR experiments measure a bulk thermal conductivity. When  $L_p < \text{MFP}$ , the Fourier law under-predicts the surface temperature oscillation amplitude, which is perceived as a reduced thermal conductivity, here and in BB-FDTR experiments. .... 53

Fig. 3.5. MFP spectra for intrinsic c-Si, doped c-Si, a-Si (500 nm film), amorphous SiO<sub>2</sub>, and platinum near room temperature. The thermal conductivity of SiO<sub>2</sub> is independent of  $L_p$ , suggesting that the MFPs of energy carriers are shorter than 60 nm. The MFP spectrum of platinum is independent of  $L_p$  due to short electron mean free paths (~10 nm) and strong electron-phonon coupling in the metal. The MFP spectrum of intrinsic c-Si and doped c-Si increase with  $L_p$  and show that micron-long MFPs contribute significantly to bulk thermal conductivity at  $T = 300\text{K}$ . Doped c-Si has a lower slope compared to intrinsic c-Si because phonons contribute to thermal conductivity with shorter MFPs. The MFP spectrum of the 500 nm a-Si film shows that propagating phonons with MFPs larger than 100 nm contribute 35±7% to its thermal conductivity (for a-Si the maximum value is used for normalization). .... 55

Fig. 3.6. The MFP spectra for 500 nm, 1 μm, and 2 μm thick films of a-Si. All curves are normalized to the maximum value of the 500 nm thick film (1.7 W/m-K). The plateau of the MFP spectra increase with increasing film thickness, suggesting phonons with MFPs larger than the film thickness are contributing significantly to thermal conductivity..... 57

Fig. 3.7. MFP spectra for intrinsic c-Si at  $T = 81, 155, 311,$  and  $417\text{ K}$  compared to MFP predictions from first principles calculations. Inset shows the temperature dependence of thermal interface conductance between the gold/chromium transducer and the intrinsic c-Si sample. The spectrum of phonon MFPs relevant to thermal conductivity shifts to lower values with increasing temperature due to increased phonon-phonon scattering. At  $T = 300\text{ K}$ , phonons with  $\text{MFP} > 1\ \mu\text{m}$  contribute 40±5% to bulk thermal conductivity. Comparison with predictions from Minnich et al. (Ref. [19]) and Esfarjani et al. (Ref. [45]) are favorable at all temperatures. .... 59

Fig. 4.1. Schematic diagrams for (a) the 1-D planar system and (b) the spherically symmetrical system, both with oscillating surface temperatures. Here,  $\mu$  is the directional cosine,  $\mu = \cos \theta$ . The parameters  $\epsilon$  and  $\rho$  are the phonon emissivity and reflectivity. .... 69

Fig. 4.2. 1-D planar geometry with temporally oscillating surface temperature and  $\varepsilon = 1 - \rho = 1$ . (a) Magnitude of the spatial temperature profiles from the diffusion and BTE solutions for  $\Lambda/L_p = 1$ . The BTE solution has two distinct regions that correspond to two distinct thermal resistances. (b) Magnitude of the thermal resistances  $R_{\text{diff},x}$  and  $R_{\text{BTE},x} = R_\varepsilon + R_{i,x}$  plotted as a function of  $\Lambda/L_p$  and  $\tau \Omega$  ..... 73

Fig. 4.3. 1-D planar geometry with temporally oscillating surface temperature and  $\varepsilon = 1 - \rho = 1, 0.5,$  and  $0.1$ . (a) Magnitude of the thermal resistance from the diffusion and BTE solutions vs.  $\Lambda/L_p$  and  $\tau \Omega$ . The BTE predicts a higher thermal resistance than the diffusion solution, which can be accounted for by reducing the effective thermal conductivity in the diffusion solution. (b) Magnitude of the suppression function plotted as a function of  $\Lambda/L_p$  and  $\tau \Omega$ . These curves are compared to the  $P_1$  solution to the BTE for parallel, black, isothermal plates and to the step function suppression function [71,73,75]..... 74

Fig. 4.4. Spherical particle embedded in an infinite medium with oscillating temperature at the surface of the sphere ( $r = r_o$ ) with  $\varepsilon = 1 - \rho = 1$ . (a) Magnitude of the thermal resistance from the diffusion and BTE solutions vs.  $\Lambda/L_p$  and  $\tau \Omega$ . (b) Magnitude of the suppression function plotted as a function of  $\Lambda/L_p$  and  $\tau \Omega$  for different values of  $\Lambda/r_o$ . For  $\Lambda/r_o = 0$ , the results collapse to the 1-D planar case shown in Figs. 4.3(a) and 4.3(b)..... 79

Fig. 4.5. Spherical particle embedded in an infinite medium with oscillating temperature at the surface of the sphere ( $r = r_o$ ) with  $\varepsilon = 1 - \rho = 1$ . (a) Magnitude of the thermal resistance from the diffusive and BTE solutions vs.  $\Lambda/r_o$  for different values of  $\Lambda/L_p$ . (b) Magnitude of the suppression function plotted as a function of  $\Lambda/r_o$  for different values of  $\Lambda/L_p$ . (c) Comparison of Eq. (4.17) when  $\Lambda/L_p = 0$  for a particle with radius  $r_o$  and a particle with radius  $3r_o$ , the exact solution for a sphere with steady-state heating from Ref. [17], and the suppression function found numerically by solving the spectral BTE for a Gaussian-shaped laser spot from Ref. [72]. Using a particle radius of  $3r_o$  in Eq. (4.17) compares well with numerical results from Ref. [72]. ..... 80

Fig. 4.6. Comparison of thermal conductivity measurements and predicted  $k_{\text{exp}}$  for silicon. (a)  $k_{\text{accum}}$  from first principles calculations (solid lines) is transformed into predicted  $k_{\text{exp}}$  vs.  $3r_o$  (dashed lines) by Eq. (4.2) using the suppression function from Eq. (4.17). A value of  $\varepsilon = 0.88$  results in the best fit to TDTR measurements at  $T = 300$  K and  $T = 80$  K from Ref. [72] with a heating frequency of  $10^6$  Hz. Predicted  $k_{\text{exp}}$  vs.  $3r_o$  for a heating frequency of  $10^7$  Hz with  $\varepsilon = 0.88$  is shown for comparison. In TDTR, the transducer/substrate interface is aluminum/silicon. (b)  $k_{\text{accum}}$  from first principles calculations is transformed into  $k_{\text{exp}}$  vs.  $L_p$  by Eq. (4.2) using the suppression function from Eq. (4.17). A value of  $\varepsilon = 0.6$  results in the best fit to BB-FDTR measurements (circles) at  $T = 300$  K and  $T = 80$  K from Ref. [73]. In BB-FDTR, the transducer/substrate interface is chromium/silicon. Predicted  $k_{\text{exp}}$  vs.  $L_p$  with  $\varepsilon = 0.88$  is compared to TDTR measurements from Ref. [71] (diamonds). ..... 83

Fig. 5.1. Schematic of the two-temperature model for an N-layered sample with arbitrarily valued and located input heat fluxes in each layer. .... 89

Fig. 5.2. Formulating the boundary conditions in (a) layer n on either side of the input heat flux at  $z = d_{n-1} + \delta_n$  and (b) layers n and n+1, on either side of the  $n^{\text{th}}$  interface corresponding to  $z = d_n$ . .... 94

Fig. 5.3. Sensitivity analysis. The phase response from the one- and two-temperature solutions (a-c), the sensitivity analysis for the two-temperature solution (d-f), and the difference in the sensitivity of  $\varepsilon$  between the two-temperature (when  $g_{\text{tr}} = 2.2 \times 10^{16} \text{ W m}^{-3} \text{ K}^{-1}$ ) and one-temperature (when  $g_{\text{tr}} = \infty$ ) solutions (g-i) using values of  $\varepsilon$  from Table 5.1 (a,d,g), values of  $\varepsilon$  from Table 5.1 with  $G = 60 \text{ MW m}^{-2} \text{ K}^{-1}$  (b,e,h), and values of  $\varepsilon$  from Table 5.1 with  $k_{\text{sub,ph}} = 13 \text{ W m}^{-1} \text{ K}^{-1}$  (c,f,i). ..... 101

Fig. 5.4. Temperature phase response is generated using the two-temperature model with (a,c)  $g_{\text{tr}} = 2.2 \times 10^{16} \text{ W m}^{-3} \text{ K}^{-1}$  and (b,d)  $g_{\text{tr}} = 22 \times 10^{16} \text{ W m}^{-3} \text{ K}^{-1}$ . These phase data are then window fit with a

solution to the one-temperature model ( $g_{tr} = \infty$ ) using the nominal value of  $G$  (a,b) and a value of  $G$  determined by fitting the high frequency phase data (c,d)..... 103

Fig. 5.5. (a) BB-FDTR phase data for SiO<sub>2</sub> and platinum from Ref. [73] modeled with the two-temperature model using parameters from Ref. [78], parameters that are consistent between each sample (“consistent parameters” shown in Table 5.2), and parameters for each sample that result in the best fit (“best-fit parameters”). (b) BB-FDTR phase data for silicon at  $T = 300$  K from Ref. [73] are window fit using the transducer parameters from (a). BB-FDTR phase data for a gold/chromium/aluminum/silicon sample are measured and fit with the two-temperature model. The thermal conductivity is independent of heating frequency compared to the gold/chromium/silicon sample. .... 111

Fig. 6.1. (a)  $k_{bulk}$  vs.  $T$  data are fit with the Born-von Karman-Slack model to find  $\Lambda(\omega)$ . (b)  $k_{accum}/k_{bulk}$  at  $T = 300$  and  $500$  K from Eq. (6.1) using the result from (a). (c) RRAM geometry is approximated as an infinite cylinder in a semi-infinite insulator. The BTE is solved for the non-equilibrium phonon distribution function in the insulator with temporally periodic surface heating. (d)  $S$  determined from Eq. (6.5). (e)  $k_{eff}$  vs. CF radius for TiO<sub>2</sub> at  $T_{\infty} = 300$  and  $500$  K due to nondiffusive effects found using  $k_{accum}$  [from (b)] and  $S$  [from (d)]. (f) Change in surface temperature and reset voltage of a CF in TiO<sub>2</sub> when accounting for nondiffusive effects..... 116

Fig. 7.1. The normalized thermal conductivity accumulation function for silicon at  $T = 300$  K [Eq. (1.11)] plotted with the interface thermal conductance accumulation function [Eq. (7.4)] vs. the ratio of  $\Lambda^*$  and  $\Lambda_{min}$  of the substrate ( $\Lambda_{min}$  in silicon is  $27$  nm at  $T = 300$  K) for different transducer Debye temperatures. .... 124

## 1. INTRODUCTION

Over the past two decades dramatic progress has been made in the efficiency and market viability of devices with nanoscale features, such as thermoelectrics [1-6], photovoltaics [7-10], and LEDs for solid-state lighting [11-16]. One of the primary reasons for this rise is increased understanding of nanoscale thermal transport processes and the effects of nanostructuring on the thermal properties of the materials and devices. As material or device dimensions decrease and become commensurate to energy carrier mean free paths (MFPs) the bulk thermal transport properties of the system, such as thermal conductivity  $k$ , reduce. The implications of this reduction are two-fold; it can be exploited in systems where low thermal conductivity is desired (e.g., thermoelectric materials), but is detrimental when high thermal conductivity is preferred (e.g., solid state lighting).

In the nonmetallic crystals used for solid-state devices, phonons are the primary energy carriers responsible for thermal transport. A comparison between phonon MFPs and the characteristic length scale of the system  $L_c$  (e.g., device size, characteristic material length scale, heat source size) determines the regime of heat transfer. If  $L_c$  is much larger than the MFPs of energy carrying phonons then heat transport is purely diffusive and spatial temperature and heat flux profiles can be determined using the heat diffusion equation and the bulk thermal conductivity  $k_{\text{bulk}}$  of the material. In the case where  $L_c$  is a boundary length scale that is less than the MFPs of phonons, such as in a nanostructured device, then heat transport is nondiffusive. In this case, reduced spatial dimensions force phonons to scatter at boundaries in a shorter distance compared to the bulk material, resulting in a reduced thermal conductivity of the device. When instead  $L_c$  is a heat source length scale less than the MFP of phonons (e.g., nanoscale-sized heater on a macroscopic substrate), heat transport in the substrate is nondiffusive since thermal gradients occur over length scales comparable to phonon MFPs. In this situation, spatial temperature and heat flux profiles within the substrate cannot be determined from the heat diffusion equation, although the bulk thermal conductivity of the substrate does not change. Instead, a reduced, apparent thermal conductivity is often used to describe observations of nondiffusive thermal transport [17-19].

Numerous theoretical, computational, and experimental studies have focused on the reduction of  $k$  due to decreasing system boundaries [20-34] or heat source length scales [17,18,35,36], many of which have attempted to estimate an effective or average phonon MFP in a material. The classic example is silicon, in which the spectrum-averaged phonon MFP (i.e., the gray MFP) can be determined as 41 nm from kinetic theory [37]. Other studies yielded average phonon MFPs in materials such as carbon nanotubes and graphene [25,33], diamond thin films [20,21], silicon thin films using harmonic Joule heating [18,24], and sapphire using ultrafast coherent soft x-ray beams [35]. Trends between  $k$  and  $L_c$ , however, indicate that phonons with different MFPs make different contributions to  $k_{\text{bulk}}$ , rendering an average MFP inadequate. These pioneering experiments led researchers to a more accurate physical description that defines cumulative contributions to  $k$  per unit MFP, known as the thermal conductivity accumulation function  $k_{\text{accum}}$  [38].

## I. Thermal conductivity accumulation function

The thermal conductivity accumulation function quantifies the cumulative MFP-dependent contributions of energy carriers to  $k_{\text{bulk}}$  of a material. Its use as a theoretical and mathematical tool is important as it provides insight into nanoscale thermal transport that moves beyond simple interpretations based on a spectrum-averaged phonon MFP. The following is an introduction and mathematical framework of  $k_{\text{accum}}$  for phonons.

### A. Mathematical description

To explain phonon MFP-dependent contributions to thermal conductivity,  $k_{\text{accum}}$  for an isotropic material is derived. We begin with the kinetic theory integral for the thermal conductivity of an isotropic bulk material [39,40]

$$k_{\text{bulk}} = \sum_{\text{p}} \int_0^{\infty} \frac{1}{3} C_{\omega} v(\omega) \Lambda(\omega) d\omega, \quad (1.1)$$

where  $\omega$  is the phonon frequency,  $C_\omega$  is the volumetric heat capacity per unit phonon frequency,  $v$  is the group velocity,  $\Lambda$  is the phonon MFP, and  $p$  indexes the phonon polarization. The volumetric heat capacity per unit phonon frequency of a nonmetallic, crystalline solid is defined as

$$C_\omega = \frac{\partial}{\partial T} D(\omega) g_{\text{BE}} \hbar \omega = \frac{q(\omega)^2}{2\pi^2} \frac{dq(\omega)}{d\omega} \hbar \omega \frac{\partial g_{\text{BE}}}{\partial T}. \quad (1.2)$$

Here,  $D(\omega)$  is the density of states,  $g_{\text{BE}}$  is the Bose-Einstein distribution,  $T$  is temperature,  $\hbar$  is the reduced Planck constant, and  $q(\omega)$  is the polarization-dependent phonon wave vector. The 3-D density of states is  $D(\omega) = [q(\omega)^2/2\pi^2][dq(\omega)/d\omega]$ , where  $dq(\omega)/d\omega = v(\omega)^{-1}$ . Substituting into Eq. (1.1) and simplifying yields

$$k_{\text{bulk}} = \sum_p \int_0^\infty \frac{1}{3} \frac{q(\omega)^2}{2\pi^2} \hbar \omega \frac{\partial g_{\text{BE}}}{\partial T} \Lambda(\omega) d\omega. \quad (1.3)$$

Transforming the integral from  $\omega$  to  $\Lambda$  and rearranging yields [41]

$$k_{\text{bulk}} = \int_0^\infty k_\Lambda d\Lambda = \int_0^\infty \sum_p -\frac{1}{3} \frac{q(\Lambda)^2}{2\pi^2} \hbar \omega(\Lambda) \frac{\partial g_{\text{BE}}}{\partial T} \Lambda \frac{d\omega(\Lambda)}{d\Lambda} d\Lambda, \quad (1.4)$$

where  $k_\Lambda$  is the contribution to  $k$  per unit MFP. The accumulation function follows from Eq. (1.4) by restricting the upper limit of integration such that

$$k_{\text{accum}}(\Lambda^*) = \int_0^{\Lambda^*} k_\Lambda d\Lambda = \int_0^{\Lambda^*} \frac{1}{3} C_\Lambda(\Lambda) v(\Lambda) \Lambda d\Lambda. \quad (1.5)$$

Eq. (1.5) states that phonons with MFP between 0 and  $\Lambda^*$  contribute  $k_{\text{accum}}(\Lambda^*)$  to the bulk thermal conductivity of the material [38].

To determine  $k_{\text{accum}}$ , we must know the dispersion relationship,  $\omega(q)$ , and the frequency dependence of the scattering term,  $\Lambda(\omega)$ . The choice of these quantities can yield solutions for  $k_{\text{accum}}$  of various materials; as an example the solution for Debye solids dominated by power law scattering is presented in the following subsection.

## B. $k_{\text{accum}}$ for Debye dispersion and power law scattering

To obtain an analytical solution for  $k_{\text{accum}}$ , a triply degenerate Debye dispersion may be assumed  $\omega(q) = v_s q$ , where  $v_s$  is the speed of sound in the material, and the scattering term can be described with a power law expression  $\Lambda(\omega) = B\omega^{-n}$ , where  $B$  is a constant that depends on temperature [41]. These assumptions to determine thermal conductivity have been collectively referred to as a modified Callaway Model [41]. In the high temperature limit  $g_{\text{BE}} = k_{\text{B}}T/\hbar\omega$  where  $k_{\text{B}}$  is the Boltzmann constant and the expression for  $k_{\text{accum}}$  becomes

$$k_{\text{accum}}(\Lambda^*) = \int_{\Lambda_{\text{min}}}^{\Lambda^*} \frac{k_{\text{B}}}{6\pi^2 n v_s^2} \left(\frac{B}{\Lambda}\right)^{\frac{3}{n}} d\Lambda, \quad (1.6)$$

where the lower limit of the integral is the minimum MFP  $\Lambda_{\text{min}} = B\omega_{\text{BZE}}^{-n}$  as defined by the frequency at the Brillouin zone edge (BZE)  $\omega_{\text{BZE}}$ . Evaluating this integral yields

$$k_{\text{accum}}(\Lambda^*) = \frac{k_{\text{B}}\omega_{\text{BZE}}^3 \Lambda_{\text{min}}}{6\pi^2 v_s^2 (3-n)} \left[ 1 - \left(\frac{\Lambda_{\text{min}}}{\Lambda^*}\right)^{\frac{3}{n}-1} \right]. \quad (1.7)$$

In the high temperature limit, Umklapp processes are the dominant resistive scattering mechanism and have been modeled with  $n = 2$  [39,42,43]. Equation (1.7) for silicon at a temperature of 300 K (in the high temperature limit where  $n = 2$ , and phonon properties are taken from Refs. [41] and [27]) is shown in Fig. 1.1 as a function of  $\Lambda^*$  and normalized by the bulk thermal conductivity  $k_{\text{bulk}} = 145$  W/m-K. Incorporating additional scattering terms (e.g., boundary, impurity, etc.) or more realistic dispersion (e.g., Born-von Karman) complicates the analytical solution but solutions are straightforward using numerical methods.

Using different scattering and dispersion models yields different accumulation functions for the same material. To highlight this difference,  $k_{\text{accum}}$  is determined for silicon at  $T = 300$  K using the Holland [44], Born-von Karman-Slack (BvKS) [38], and gray [41] models and compared with results from molecular dynamics [37] and first principles calculations [45] in Fig. 1.1. Clearly, the shape of  $k_{\text{accum}}$  strongly depends on the type of model used and experimental measurement of  $k_{\text{accum}}$  is crucial.

Nonetheless, the more sophisticated models show a broad distribution of MFPs spanning approximately four orders of magnitude.

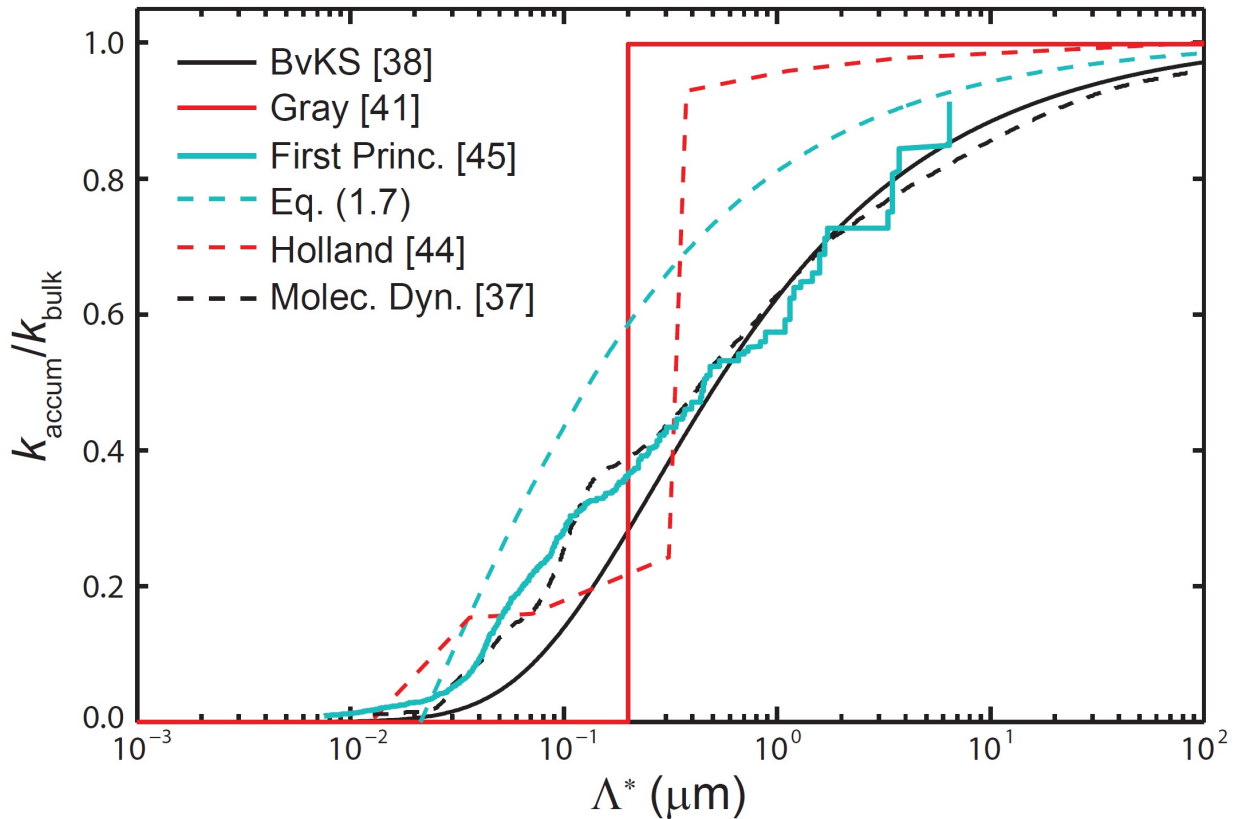


Fig. 1.1. Thermal conductivity accumulation functions for silicon at  $T = 300$  K ( $k_{\text{bulk}} = 145$  W/m-K) from the gray model [41], BvKS model [38], Holland model [44], Eq. (1.7), first principles [45], and molecular dynamics [37]. These data were previously compiled by Yang and Dames [41].

### C. Theoretical prediction of phonon mode properties and $k_{\text{accum}}$

The phonon mode-dependent contributions to the thermal conductivity of a crystalline semiconductor, needed to build  $k_{\text{accum}}$ , can be predicted using lattice dynamics calculations [46,47]. The required inputs are the second- and third-order force constants. A major advance in this field was made in 2007, when Broido et al. demonstrated that when force constants are obtained from first principles calculations, excellent agreement is found with experimental measurements of  $k$  for silicon and germanium [48]. Subsequent work has found similarly good agreement for a range of materials [45,49,50].

Harmonic lattice dynamics calculations are first used to obtain the mode frequencies (i.e., the phonon dispersion), from which the heat capacity and group velocities are calculated [51]. Under the relaxation time approximation, anharmonic lattice dynamics calculations are then used to predict the phonon lifetimes, and from these, the MFPs. In some materials, the relaxation time approximation is not valid and an iterative solution to the linearized phonon Boltzmann transport equation (BTE) can be used to obtain better estimates of the lifetimes/MFPs [49,52,53]. Given the MFPs of all phonon modes in the Brillouin zone, it is straightforward to build  $k_{\text{accum}}$ , as shown in Fig. 1.1 for silicon.

## II. Experimental methods to measure $k_{\text{accum}}$

Quantifying contributions to thermal conductivity by specific phonons has long been of experimental interest [17,20,21]. One convenient method involves estimating an average phonon MFP that dominates heat transport. This value is determined from experimental observations of nondiffusive heat transport, which can be induced by varying the sample thickness or heater dimensions [18,20,21,24,35,54]. This average phonon MFP, however, has limited utility and application since phonons with a wide range of MFPs significantly contribute to thermal transport.

Only recently have experimental techniques been developed and used for specifically studying  $k_{\text{accum}}$  based on measurements of bulk materials. Notably, techniques using neutron scattering [55] and x-ray free-electron laser pulses [56] have shown promise for measuring mode-dependent properties. At the benchscale, however, the focus has been on transient thermal grating (TTG), time domain thermoreflectance (TDTR), and broadband frequency domain thermoreflectance (BB-FDTR). These techniques involve systematically varying the length scale over which thermal gradients occur  $L_c$  within a range comparable to phonon MFPs, while simultaneously measuring the apparent thermal conductivity  $k_{\text{exp}}$  (i.e., thermal conductivity is measured as a function of  $L_c$ ). Schematics highlighting  $L_c$  in each technique are shown in Fig. 1.2. ***One major accomplishment resulting from my time at CMU was the invention and development of BB-FDTR, as described in Chapter 2 (and K. T. Regner, S. Majumdar, and J. A. Malen, Instrumentation of Broadband Frequency Domain Thermoreflectance for Measuring***

*Thermal Conductivity Accumulation Functions, Review of Scientific Instruments, vol. 84, pp. 064901, 2013*). In the following subsections, a summary of each technique is given and a more thorough description of BB-FDTR can be found in Chapter 2 of this dissertation.

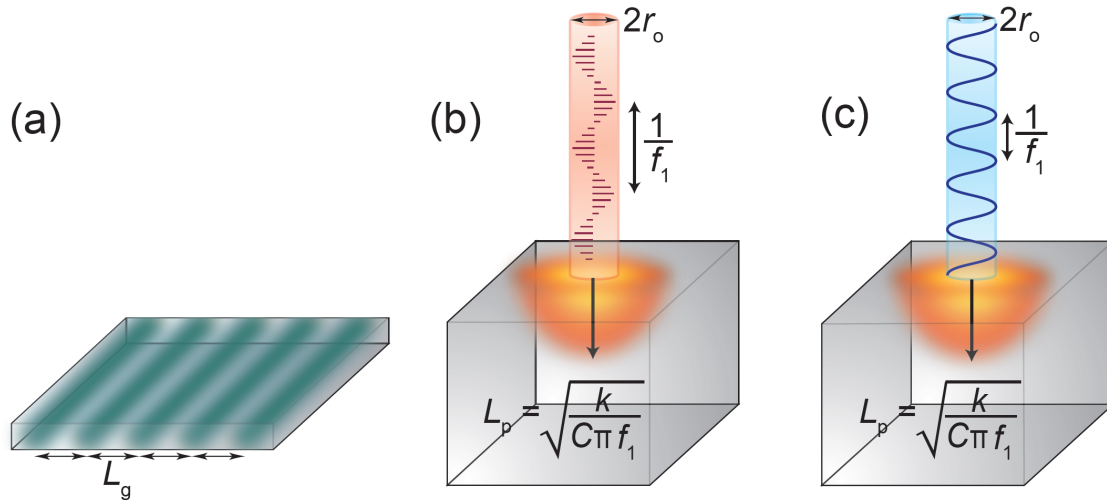


Fig. 1.2. Schematics highlighting  $L_c$  (as  $L_g$ ,  $L_p$ , or  $r_o$ ) in (a) transient thermal grating (b) time domain thermoreflectance and (c) broadband frequency domain thermoreflectance. These three techniques are used to measure thermal conductivity  $k_{\text{exp}}$  as a function of the relevant experimental length scales  $L_c$  indicated in the figure.

### A. Transient thermal grating

In TTG, two laser pulses are crossed at the sample surface causing optical interference. The interference pattern creates a spatially periodic intensity profile that is focused on the sample, creating a spatially periodic temperature profile with period  $L_c = L_g$ , as illustrated in Fig. 1.2(a). The spatially periodic temperature profile causes the temperature-dependent indices of refraction to vary with a spatially periodic profile such that an optical grating is created. A probe beam is simultaneously diffracted by this optical grating. Transient heat diffusion and counter-propagating surface acoustic waves create time-dependent diffraction decay. A detector measures the time-dependent intensity of the diffracted light, which is used to determine the in-plane thermal diffusivity of the sample [57-62].

By changing the grating period induced by the pump laser,  $k_{\text{exp}}$  was determined as a function of  $L_g$  for free-standing thin films [63-65]. The authors found that thermal conductivity decreases with

decreasing grating period when phonon MFPs exceed  $L_g$ . The relationship between  $k_{\text{exp}}$  vs.  $L_g$  for thin films and  $k_{\text{accum}}$  for bulk materials requires a thorough analysis that will be discussed later in this dissertation.

## **B. Time domain thermoreflectance**

TDTR is a non-contact, laser-based thermal conductivity measurement technique that uses time delayed laser pulses to both heat and measure the surface temperature of a sample. The sample is prepared by coating the surface with a thin metal film, which acts as a thermoreflectance transducer. In a TDTR experiment, a pump pulse is absorbed by the transducer, causing the surface temperature to rapidly increase. As heat diffuses into the sample, the surface temperature decays. The change in surface temperature is monitored by observing the intensity of the reflected probe pulse, which changes based on the thermoreflectance of the transducer. By varying the time delay between the pump and probe pulses, the temporal surface temperature can be resolved and fitted to a solution of the heat diffusion equation in a layered structure for the unknown thermal conductivity of the sample [66-70]. It should be noted that the existence of the transducer layer introduces an interface thermal conductance  $G$  into the analysis, which is another unknown fitting parameter.

To increase the signal to noise ratio, the pump pulse train intensity is modulated sinusoidally at a secondary frequency  $f_1$  using an electro-optic modulator that enables lock-in detection. The sinusoidal surface heat flux results in an oscillating thermal wave into the solid. The thermal penetration depth  $L_p = \sqrt{k/C\pi f_1}$  is the characteristic spatial decay length of the temperature profile and is defined as the depth into the material where the temperature amplitude drops  $e^{-1}$  of the surface temperature. Here,  $C$  is volumetric heat capacity. Consequently, TDTR has several inherent timescales due to the use of a pulsed laser, including (i) the laser pulse width (<0.5 ps), (ii) the delay time between pump and probe pulses (>100 ps), (iii) the time between laser pulses (~10 ns), and (iv) the secondary modulation frequency ( $1/f_1 \sim 100$  ns).

Two relevant length scales act as  $L_c$  in TDTR and are shown in Fig. 1.2(b): (i) the thermal penetration depth  $L_p$ , which arises from the intensity modulation of the heating laser and (ii) the radius of the heating laser  $r_o$ , which is defined as the  $e^{-2}$  radius of the Gaussian shaped laser beam. TDTR measurements of  $k_{exp}$  as a function of both  $L_p$  and  $r_o$  have been reported for different materials [19,71,72]. The interpretation of the results to relate  $k_{exp}$  vs.  $L_c$  to  $k_{accum}$  will be discussed in the following section.

### C. Broadband frequency domain thermorefectance

BB-FDTR is a technique closely related to TDTR, but in practice requires different equipment and interpretation [73-75]. I give a brief description of the technique here for completeness, but a more detailed description follows in Chapter 2. In BB-FDTR, the intensity of a continuous wave (CW) pump laser is modulated sinusoidally at frequency  $f_1$  and focused on the sample, which is coated with a metal transducer layer. The periodic heat flux causes the surface temperature to oscillate at  $f_1$ . A CW probe laser monitors the periodic surface temperature response based on the thermorefectance of the transducer. The periodic change in the thermorefectance of the sample surface induces intensity modulation at  $f_1$  in the reflected probe beam, which contains information about  $k$  of the sample. The phase of the reflected probe beam with respect to the pump beam is used to determine  $k_{exp}$  vs.  $L_p$  by fitting it to the solution to the heat diffusion equation over a range of  $f_1$  [73-76]. The relevant length scales at the sample in a BB-FDTR experiment are illustrated in Fig. 1.2(c)

Since  $L_p$  is inversely proportional to the heating frequency, it is desirable to modulate the heat flux (pump) at high frequencies to measure a greater range of  $k_{exp}$  vs.  $L_p$ . Theoretically, the upper bound of  $f_1$  is unlimited due to the use of CW lasers. Realistically, however, ambient and coherent noise drastically reduce the signal to noise ratio when  $f_1 > 20$  MHz [74]. To overcome this limitation a heterodyne procedure is used to increase the signal to noise ratio at larger heating frequencies ( $f_1$  can be modulated up to 200 MHz using CW lasers with a heterodyne procedure) [74]. *Another major accomplishment resulting from my time at CMU is the measurement of  $k_{exp}$  vs.  $L_p$  for Si-based materials at device operating temperatures using BB-FDTR, and is described in Chapter 3 (and K. T.*

*Regner, D. P. Sellan, Z. Su, C. H. Amon, A. J. H. McGaughey, and J. A. Malen, Broadband Phonon Mean Free Path Contributions to Thermal Conductivity Measured Using Frequency Domain Thermoreflectance, Nature Communications, vol. 4, pp. 1640, 2013).*

#### **D. Comparison of techniques**

The advantages and disadvantages of each technique are summarized in Table 1.1. Specifically, TDTR is a widely used technique that can easily be adapted to measure  $k_{\text{exp}}$  vs.  $L_p$  or  $r_o$  with minor modifications. Relative to TDTR, the use of CW lasers in FDTR results in a single timescale ( $1/f$ ) associated with laser heating. The heterodyne procedure employed by BB-FDTR broadens the range of this timescale [73,74]. Recently, Collins et al. showed that the complex TDTR signal could be decomposed in the frequency domain to extract data up to 1 GHz, therein exceeding the highest frequency measured by BB-FDTR [77]. The existence of a transducer layer in TDTR and BB-FDTR complicates the interpretation of  $k_{\text{exp}}$  vs.  $L_c$  and introduces an additional fitting parameter into the analysis, i.e., the interface conductance between the transducer and sample  $G$ . TDTR may be better suited to accommodate this additional fitting parameter since the data as a function of delay time between pump and probe pulses in TDTR can be used to isolate  $G$ , while  $k$  is extracted from timescales commensurate to the secondary modulation frequency  $f_1$ . A further complication is the complex electron-phonon dynamics in the transducer that influences the signal at high frequency and is more pronounced in metals that have weak electron-phonon coupling (e.g., the gold transducers, used in BB-FDTR [77,78]). Finally, while TDTR and BB-FDTR are sensitive to cross-plane thermal conductivity, TTG is unique in that it is capable of taking in-plane measurements and is not complicated by a transducer.

Table 1.1. Advantages and disadvantages of the techniques outlined to measure  $k_{\text{exp}}$  vs.  $L_c$ .

Technique	Pros	Cons	Ref.
TTG	<ul style="list-style-type: none"> <li>• Capable of measuring in-plane anisotropy</li> <li>• No transducer required, which simplifies interpretation of results</li> </ul>	<ul style="list-style-type: none"> <li>• Grating period (<math>L_g</math>) limited by the diffraction limit of light</li> </ul>	[63-65]
TDTR	<ul style="list-style-type: none"> <li>• Robust, common technique can be easily modified to measure <math>k_{\text{exp}}</math> vs. <math>L_c</math></li> <li>• Incorporation of multiple length scales (<math>r_o</math> and <math>L_p</math>)</li> <li>• Multiple timescales (pump/probe delay time and <math>f_i</math>) may facilitate the extraction of <math>k_{\text{exp}}</math> and <math>G</math></li> </ul>	<ul style="list-style-type: none"> <li>• Spot size (<math>r_o</math>) limited by diffraction limit of light</li> <li>• Interpretation of <math>k_{\text{exp}}</math> vs. <math>L_c</math> is complicated due to the existence of the transducer layer</li> <li>• Additional fitting parameter <math>G</math></li> </ul>	[19,71,72]
BB-FDTR	<ul style="list-style-type: none"> <li>• Heating frequency (<math>f_i</math>) theoretically unlimited</li> <li>• Incorporation of multiple length scales (<math>r_o</math> and <math>L_p</math>)</li> <li>• One timescale is clearly defined due to the use of CW lasers</li> </ul>	<ul style="list-style-type: none"> <li>• Spot size (<math>r_o</math>) limited by diffraction limit of light</li> <li>• Interpretation of <math>k_{\text{exp}}</math> vs. <math>L_c</math> is complicated due to the existence of the transducer layer</li> <li>• Additional fitting parameter <math>G</math></li> </ul>	[73-75]

### III. Relating $k_{\text{exp}}$ and $k_{\text{accum}}$

Experimental techniques to specify  $k_{\text{accum}}$  focus on inducing nondiffusive thermal transport by varying an experimentally controllable length scale  $L_c$  in a range comparable to energy carrier MFPs. Ideally, experiments would be directly interpreted with a solution to the BTE that accurately describes the experiment and inherently considers nondiffusive effects over the full phonon spectrum, but this procedure is not straightforward. Instead, nondiffusive experimental measurements are fit to a solution to the heat diffusion equation, which yields an experimental thermal conductivity  $k_{\text{exp}}$  as a function of  $L_c$ . To obtain  $k_{\text{accum}}$ ,  $L_c$  is related to the MFP-dependent contributions to  $k_{\text{exp}}$  using a suppression function  $S(\Lambda, L_c)$ . Physically, the suppression function describes how phonon contributions to thermal conductivity are

suppressed as a function of experimental length scales. Based on this definition the suppression function can be used to modify the mean-free-path-dependent contributions to  $k_\Lambda$  in Eq. (1.5) so that instead of  $k_{\text{bulk}}$  (when  $\Lambda^* = \infty$ ), one finds the expected thermal conductivity in a specific nondiffusive experiment

$$k_{\text{exp}}(L_c) = \int_0^\infty S(\Lambda, L_c) k_\Lambda d\Lambda. \quad (1.8)$$

The idea of a suppression function was initiated by Maznev et al. [79] (therein referred to as a correction factor), first applied using Eq. (1.8) by Minnich [80], and derived with added formality by Yang and Dames [41].

The suppression function is hence used to map measurements of  $k_{\text{exp}}$  vs.  $L_c$  to the actual  $k_{\text{accum}}$  of the material by quantifying how much a certain phonon will contribute to thermal conductivity in a nondiffusive experiment compared to its contribution in a completely diffusive system (i.e., bulk) [41,72,79-83]. Thus, the suppression function is different for different experimental techniques. The accuracy of Eq. (1.8) depends on the accuracy of  $S(\Lambda, L_c)$  and  $k_\Lambda$ . The accuracy of  $k_\Lambda$  has been improved by first principles-informed lattice dynamics, while the accuracy of  $S(\Lambda, L_c)$  depends on how it is determined (e.g., how the BTE is solved). Suppression functions found using varying degree-of-accuracy solution methods are discussed in the following subsections for the different experimental techniques.

### A. Step function suppression function

The initial interpretation of  $k_{\text{exp}}$  vs.  $L_c$  measurements was that only phonons with  $\Lambda < L_c$  contribute to the measured value of thermal conductivity  $k_{\text{exp}}$ . Mathematically, this takes the form

$$k_{\text{exp}}(L_c) = \int_0^{L_c} k_\Lambda d\Lambda, \quad (1.9)$$

and is equivalent to  $S(\Lambda, L_c)$  being a step function from 1 to 0 at  $\Lambda/L_p = 1$ . Eq. (1.9) equivalently states that measurements of  $k_{\text{exp}}$  vs.  $L_c$  are equal to  $k_{\text{accum}}$  vs.  $\Lambda$ .

In 2007, Koh and Cahill were the first to use this interpretation to experimentally probe  $k_{\text{accum}}$  in bulk semiconductor alloys using TDTR measurements of  $k_{\text{exp}}$  vs.  $L_p$  [71]. Similarly, Eq. (1.9) is used to interpret BB-FDTR measurements of  $k_{\text{exp}}$  vs.  $L_p$  of Si-based materials shown in Chapter 3 of this

dissertation [73,75]. Minnich *et al.* took a different approach and varied  $r_o$  in TDTR measurements of silicon at cryogenic temperatures. They used Eq. (1.9) to explain contributions to  $k_{\text{exp}}$  from phonons having a MFP less than  $2r_o$  [19]. None of these initial results considered electron-phonon coupling processes within the transducer. Using TDTR, Wilson and Cahill observed suppression in the thermal conductivity of semiconductor alloys but not silicon as a function of  $L_p$ , while they conversely observed suppression in the thermal conductivity of silicon but not semiconductor alloys, as a function of  $r_o$  [78].

## B. Experiment-specific suppression function from the BTE

The suppression function was first considered as a means to interpret TTG measurements where phonon MFPs were on the order of or longer than the grating period [65,79]. The procedure for determining the suppression function involves solving the BTE in an experiment-specific geometry. For TTG, a simplified geometry is an infinite, 1-D slab with an initial, spatially sinusoidal temperature profile. Matching the diffusive prediction of temperature decay rate to that predicted by the BTE requires a reduced value of  $k$ . This value of  $k$  describes nondiffusive transport and results from suppressed contributions from phonons with MFPs commensurate or greater than  $L_c$ .

The suppression function for TTG was determined analytically in Refs. [79,81,82]. To determine analytical solutions, the problem was treated as isotropic and the relaxation time approximation was made. The resulting form of the BTE is

$$\frac{\partial n}{\partial t} + \mathbf{v} \cdot \nabla_{\mathbf{r}} n = \frac{n_e - n}{\tau}, \quad (1.10)$$

where the non-equilibrium distribution function  $n$  is the phonon energy density per unit phonon frequency function,  $n_e$  is the equilibrium distribution function, and  $\tau$  is the lifetime. To generate analytical solutions, typically only one dimension is considered.

To simplify the analysis further, the gray approximation can be assumed (i.e., all phonons have the same MFP). Solving Eq. (1.10) under the gray approximation yields a suppression function that quantifies the contribution to thermal conductance by one phonon mode in a nondiffusive experiment with length scale  $L_c$ , relative to the same phonon mode in a diffusive experiment. Solutions to the gray

BTE, however, are often analytical and thereby are useful tools for understanding trends and providing physical insight to the problem.

Using the gray approximation, Collins *et al.* showed that Eq. (1.10) can be solved analytically using separation of variables to get the BTE-predicted temperature decay rates in TTG, which were compared to the diffusive decay rates to get the suppression function shown in Fig. 1.3 [81]. Hua and Minnich eliminated the gray approximation and determined an analytical solution to the phonon frequency-dependent BTE [82]. Alternatively, Eq. (1.10) can be coupled to the heat diffusion equation and solved as a two-fluid problem. Here, low frequency phonons are described by the BTE, which can describe ballistic, diffusive, and intermediate transport regimes, while high frequency, diffusive phonons are described with the heat diffusion equation [79]. The two-fluid model captures the interaction of low frequency phonons with a thermal reservoir and eliminates the necessity of using the gray approximation. The suppression functions determined using the two-fluid and gray models are compared in Fig. 1.3. It should be noted that eliminating the gray approximation requires material-dependent scattering rates to determine the suppression function. A comparison of gray, two-fluid, and phonon frequency-dependent predictions of  $k_{\text{accum}}$  based on Eq. (1.8), however, suggests that material-dependence of the suppression function is weak (less than 7% variation in  $k_{\text{accum}}$ ) for silicon and PbTe at  $T = 300$  K over TTG grating periods from  $10^{-1}$  to  $10^6$  nm [81].

*Another major accomplishment as a result of my time at CMU is the development of the suppression function for thermoreflectance-based techniques (TDTR and BB-FDTR) and is described in Chapter 4 (and K. T. Regner, A. J. H. McGaughey, and J. A. Malen, Analytical Interpretation of Non-Diffusive Phonon Transport in Thermoreflectance Thermal Conductivity Measurements, Physical Review B, vol. 90, pp. 064302, 2014).* This work was motivated by the rigorous analysis of TTG along with discrepancies between TDTR and BB-FDTR measurements of  $k_{\text{exp}}$  vs.  $L_p$  on silicon at room temperature. In thermoreflectance experiments there are two apparent length scales: the thermal penetration depth  $L_p$  and the heating laser spot radius  $r_o$ , which should both be considered in the determination of the suppression function.

An analytical solution for the suppression function was found by solving Eq. (1.10) (in spherical coordinates) under the gray approximation for a sphere embedded in an infinite medium with a periodically changing temperature at the sphere/medium interface [83]. The solution incorporates suppression from  $L_p$  due to the oscillating nature of the surface temperature and a spot size effect by changing the radius of the embedded sphere. The  $L_p$ -dependence ( $r_o \rightarrow \infty$ ) and the  $r_o$ -dependence ( $L_p \rightarrow \infty$ ) of the suppression function derived in Ref. [83] are shown in Fig. 1.3. Notably the result is a function of the phonon transmission properties at the transducer/substrate interface, which suggests that the transducer affects the observed  $k_{\text{exp}}$ .

To improve accuracy of the suppression function for thermoreflectance techniques, numerical solutions are required to solve the phonon frequency-dependent BTE with Gaussian periodic surface heating. Ding *et al.* did so using a Monte Carlo approach and quantified suppression due to spot size as shown in Fig. 1.3 [72]. The suppression function was used to favorably compare predictions of  $k_{\text{exp}}$  with experimental data using Eq. (1.8). In this work the authors predicted suppression in the cross plane direction, but did not observe it in their experiments. The comparison of suppression functions for TDTR and BB-FDTR using varying degree-of-accuracy solutions is highlighted in Fig. 1.3. Considering the presence of a transducer increases the complexity further [72,84]. Minnich *et al.* solved the frequency-dependent BTE in a double-layer geometry to simulate the presence of a transducer in thermoreflectance measurements and found no heating frequency-dependence to the calculated value of thermal conductivity [84]. Furthermore, it has been suggested that weak electron-phonon coupling in the gold transducer will diminish the reported thermal conductivity suppression as a function of  $L_p$  in silicon. Resolving the physics in the transducer is necessary to refine the interpretation of thermoreflectance measurements. *Another major accomplishment resulting from my time at CMU is the development of a two-temperature model to account for electron-phonon non-equilibrium in the transducer layer and is described in Chapter 5 (and K. T. Regner, L. C. Wei, and J. A. Malen, Interpretation of Thermoreflectance Measurements with a Two-temperature Model Including Non-surface Heat Deposition, Journal of Applied Physics, vol. 118, pp. 235101, 2015).*

The utility of the suppression function is that experimental measurements of  $k_{\text{exp}}$  vs.  $L_c$  can be directly compared to predictions of  $k_{\text{accum}}$  using Eq. (1.8). One way to make this comparison is to predict the experimental measurement using the experiment-specific suppression function and material-dependent  $k_\Lambda$  as inputs to Eq. (1.8), where  $k_\Lambda$  can be obtained from models (e.g., Callaway, BvKS, first principles, etc.). Alternatively,  $k_\Lambda$  can be obtained directly from measurements of  $k_{\text{exp}}$  vs.  $L_c$  using the experiment-specific suppression function. This method involves solving an inverse problem, which was done by Minnich for TTG using convex optimization [80]. Similar approaches could be applied to TDTR and BB-FDTR.

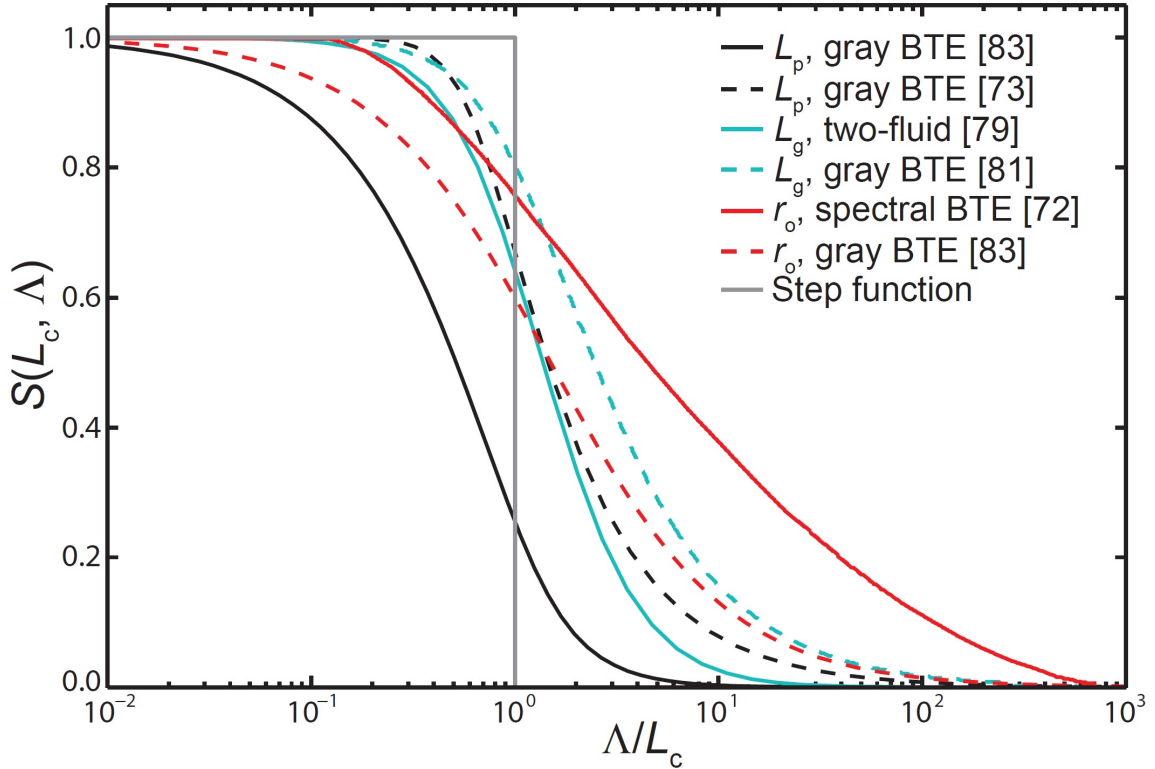


Fig. 1.3. Suppression functions derived for TTG, TDTR, and BB-FDTR. These are used in Eq. (1.8) to interpret measurements of  $k_{\text{exp}}$  vs.  $L_c$ . Also shown is the step function interpretation from Eq. (1.9).

#### IV. Importance of $k_{\text{accum}}$

Accurate experimental measurements of  $k_{\text{accum}}$  are being pursued, but the utility of  $k_{\text{accum}}$  for the engineering of devices should not be overlooked. To maximize the broader impacts of  $k_{\text{accum}}$  it is

important to understand why knowing it is helpful and how to use it as a tool for design. Recent work has explored the importance of  $k_{\text{accum}}$  by identifying the existence of a universal  $k_{\text{accum}}$  for similar materials [75] and by showing how  $k_{\text{accum}}$  can be used to characterize nanostructured devices [41,85,86].

### A. Universality of $k_{\text{accum}}$

Freedman *et al.* measured the thermal conductivity of GaAs, GaN, AlN, and 4H-SiC via BB-FDTR as a function of  $L_p$  for a range of temperatures [75]. They found that when  $k_{\text{exp}}$  for GaAs, GaN, AlN, 4H-SiC and Si was plotted as a function of a normalized experimental characteristic length scale (i.e., the ratio of  $L_p$  to the minimum phonon MFP  $\Lambda_{\text{min}}$ , defined below),  $k_{\text{exp}}$  collapsed to a single universal curve in the high temperature regime where Umklapp scattering is the dominant source of thermal resistance. Assuming a triply degenerate Debye dispersion, the accumulated thermal conductivity of a semiconductor is Eq. (1.7) with  $n = 2$ . After normalizing by  $k_{\text{bulk}}$  [i.e., the upper limit of integration in Eq. (1.6) equals infinity], Eq. (1.7) becomes

$$\frac{k_{\text{accum}}(\Lambda^*)}{k_{\text{bulk}}} = 1 - \frac{1}{\sqrt{\Lambda^*}} \sqrt{B\omega_{\text{BZE}}^{-2}} = 1 - \sqrt{\frac{\Lambda_{\text{min}}}{\Lambda^*}}. \quad (1.11)$$

This result implies that thermal conductivity in small unit cell semiconductors results predominantly from phonons with MFPs 1-200 times the phonon MFP of acoustic phonons at the Brillouin zone edge. The collapse of experimental thermal conductivity measurements suggests that the phonon MFP spectrum is a universal feature of crystalline semiconductors.

### B. Applying bulk $k_{\text{accum}}$ measurements to nanostructures

Knowledge of  $k_{\text{accum}}$  is useful when predicting the thermal conductivity of nanostructures [41,85,86]. Yang and Dames found that if the accumulation function is known for a certain bulk material, then the thermal conductivity accumulation function of a nanostructure,  $k_{\text{nano,t}}$ , made of the same material can be predicted as [41]

$$k_{\text{nano,t}} = - \int_0^\infty k_{\text{accum}}(\Lambda) \frac{dA_t}{d\Lambda} d\Lambda, \quad (1.12)$$

where  $A_t$  is a boundary scattering function that depends only on the ratio between the bulk MFPs in the material and the critical length scale of the nanostructure,  $L_c$ , and the subscript  $t$  represents the type of nanostructure (e.g., wire, film, etc.). The form of the boundary scattering function can be obtained by solving the BTE and was used to evaluate  $k_{\text{nano},t}$  as a function of characteristic nanostructure dimension using predictions for  $k_{\text{accum}}$  from the Callaway, Holland, BvKS, and Gray models along with molecular dynamics and first principles calculations in Ref. [41].

Furthermore, solutions to the BTE in different geometries yield the suppression function for that geometry. Combining the result with the accumulation function yields the effective thermal conductivity of that specific geometry/material combination as a function of the characteristic dimension of the geometry  $L_c$ . As a first order approximation of the heat transport in nanostructures, the predicted, reduced value of effective thermal conductivity can be used in the heat diffusion solution in lieu of the bulk thermal conductivity to more accurately predict temperature profiles inside the nanostructure. *Another major accomplishment as a result of my time at CMU is the use of this procedure to predict the temperature rise of conductive filaments in resistive-switching memory devices, described in Chapter 6 (and K. T. Regner and J. A. Malen, under review at IEEE Electron Device Letters).*

## V. Organization of the dissertation

The preceding sections give a thorough review of the phonon thermal conductivity accumulation function, including (i) how it is formulated, (ii) how it has been measured, (iii) the interpretation of those measurements, (iv) and its importance to designing and engineering devices and materials. In the following chapters I will discuss my specific contributions in detail. In **Chapter 2** I describe BB-FDTR, a technique I developed to observe nondiffusive thermal transport in different materials. In **Chapter 3** I describe how I use BB-FDTR to observe nondiffusive thermal transport in Si-based materials at device operating temperatures. I use the simple interpretation of Eq. (1.8) to relate these measurements of  $k$  vs.  $L_p$  to  $k_{\text{accum}}$  vs. MFP. In **Chapter 4** I formulate an analytical suppression function for thermoreflectance experiments that relates the length scales in these experiments ( $r_o$  and  $L_p$ ) to the MFPs of energy carriers

by solving the BTE. I use this suppression function to re-interpret my results from Chapter 3 using Eq. (1.9). In **Chapter 5** I develop a two-temperature model that is used to account for electron-phonon non-equilibrium that occurs in the transducer layer of thermoreflectance experiments. In **Chapter 6** I extend my BTE analysis to a practical application by developing an analytical solution to the BTE to predict spatial temperature and heat flux profiles in resistive-switching memory devices. I use my solution to predict the temperature rise of conductive filaments that are formed in these devices and find the filaments get hotter than expected due to nondiffusive thermal transport. Finally, in **Chapter 7** I provide future directions for studying nanoscale thermal transport.

## 2. BROADBAND FREQUENCY DOMAIN THERMOREFLECTANCE

### I. Overview

Despite its importance to the fundamental thermal properties of matter, measurement of  $k_{\text{accum}}$  was only first realized in 2007 using TDTR [71]. In this study, Koh and Cahill found that the thermal conductivity of semiconducting alloys depends on the secondary pump pulse modulation frequency  $f_1$  [71]. In this case,  $L_c$  is set by the thermal penetration depth  $L_p$ . In TDTR, however,  $L_p$  is restricted by an upper limit to the modulation frequency of  $\sim 20$  MHz because at least four pulses are required in a modulation cycle and the pulse repetition rate of the common Ti-Sapphire oscillators is 80 MHz. Alternatively,  $L_c$  can be set by the dimensions of nano-patterned heaters to extract the average phonon MFP of the substrate [35], but requires an optically transparent sample. One recent TDTR study observed reduced  $k$  in Silicon for smaller laser spot sizes  $r_o$  and hypothesized that they were making direct measurements of  $k_{\text{accum}}$  with  $L_c = 2r_o$  [19]. In this approach, however, the diffraction limit of light limits possible spot sizes and hence the range of the measurement.

In this chapter, I describe broadband frequency domain thermoreflectance (BB-FDTR), a MFP spectroscopy technique that uses high frequency modulation of CW lasers to vary  $L_p$  and measure an unprecedented range of  $k_{\text{accum}}$  ( $L_p = L_c$ ). This technique is based on frequency domain thermoreflectance [76,87] (FDTR), which is illustrated in Fig. 2.1(a), where a CW pump laser is intensity modulated at frequency  $f_1$  and focused on to the sample surface. This periodic heat flux causes the surface temperature to change periodically at frequency  $f_1$ . The amplitude and phase of the surface temperature with respect to the incident heat flux contains information about the thermal properties of the sample, and is measured with a CW probe laser based on the thermoreflectance of the sample. The temperature response measured by the probe beam is fit to an analytical solution to the heat diffusion equation to obtain a value of thermal conductivity of the sample.

To measure a large range of  $k_{\text{accum}}$ , it is necessary to create a thermal penetration depth in the material that is commensurate to the MFP of the phonons. This range is achieved by using modulation

frequencies that limit the length scale of heat diffusion. Theoretically, since FDTR uses CW lasers, the pump can be modulated at infinite frequency to measure the entire  $k_{\text{accum}}$ . Signal to noise ratios in FDTR, however, decrease at larger heating frequencies due to the decreasing signal size and presence of coherent noise and ambient noise at high frequency. Most early FDTR-based techniques do not modulate the pump laser higher than 2 MHz [88-90], however, Pottier [91] and, more recently, Schmidt et al. [76] and Ong et al. [6] report heating frequencies up to 10 MHz and 20 MHz, respectively.

The BB-FDTR technique produces a high fidelity thermal signal by inducing an additional modulation on the reflected, thermally modulated probe laser at frequency  $f_2$ . Heterodyning the probe laser allows for heating frequencies up to 200 MHz but measurement of the thermal response at a much lower frequency,  $f_1 - f_2$ , where the signal to noise ratio is much larger. Achieving this high frequency measurement is useful for accurately resolving interface thermal conductance, but more uniquely for measuring  $k_{\text{accum}}$  over a broad range with minimal experimental modification (i.e., no changing focusing objectives or optical gratings, no special sample preparation, etc.). Since  $L_p$  and hence the MFPs accessible to BB-FDTR depend on thermal conductivity (through  $L_p = \sqrt{k/\pi C f_1}$ ), its range “adjusts” to the material, unlike spatially fixed cutoff length scales like  $r_0$  and the transient grating period. The following subsections describe the instrumentation and fitting details, a similar alternative approach that I found to be unsuccessful in the lab, and a detailed sensitivity analysis. This work appears in *Review of Scientific Instruments*, vol. 84, pp. 064901, 2013 with contributions from co-authors S. Majumdar and J. A. Malen and is reprinted with permission by the American Physical Society © 2013 [74].

## II. Experimental setup

The experimental setup for BB-FDTR is shown in Fig. 2.1(b) with accompanying Table 2.1 that specifies the make and model of key components. A 488 nm, CW pump laser first travels through an optical isolator (I-488). The optical isolator prevents the back-reflected beam from entering the laser cavity, which causes instabilities in the laser output power. A half wave plate (HWP) is used to vertically polarize the light, which is then focused into an electro-optic modulator (EOM1) that induces a sinusoidal

intensity modulation at frequency  $f_1$  on the transmitted vertically polarized light. High frequency EOMs typically have a small aperture to reduce the capacitance of the crystal, and as a result, a long focal length lens (LN) is used to focus into the EOMs. After exiting EOM1, the pump beam passes through a 488 nm band pass filter (BP-488) and another lens to re-collimate the light. The 488 nm band pass filter ensures that back reflected probe light does not get directly modulated and detected in the signal after multiple reflections. A beam sampler (BS) transmits 90% of the pump beam and is used to co-align the pump beam and probe beam along the same path.

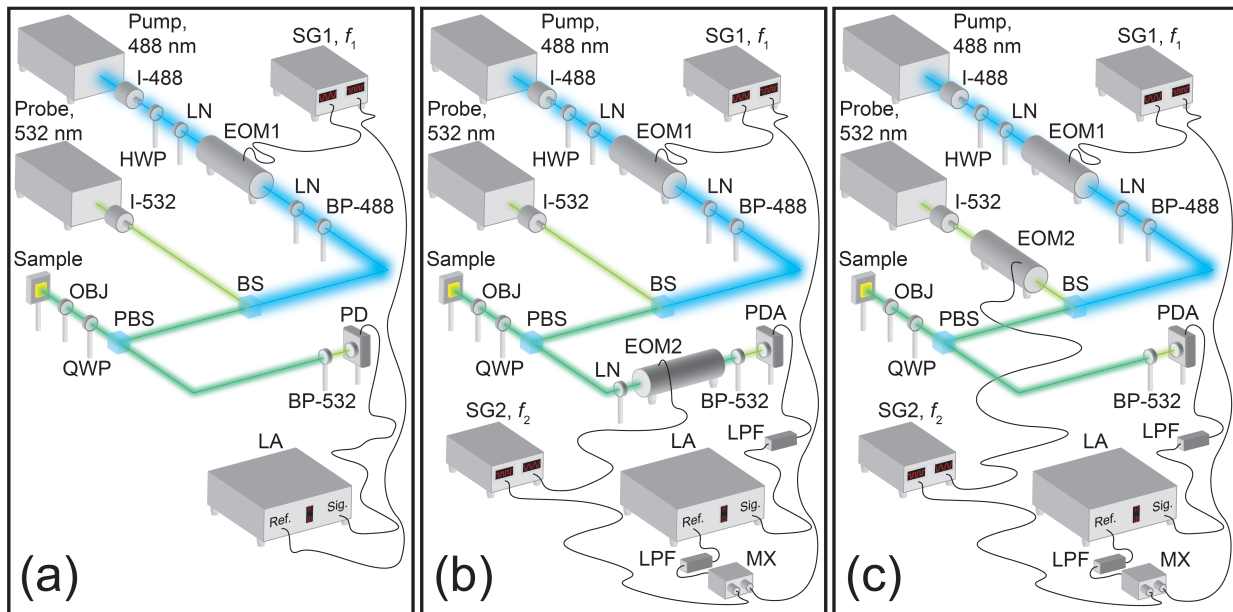


Fig. 2.1. (a) Schematic of traditional FDTR. (b) Schematic of BB-FDTR. The pump beam undergoes intensity modulation at frequency  $f_1$  and gets focused on the sample. EOM2 induces an additional modulation in the reflected probe beam, heterodyning the thermal signal, allowing for higher heating frequencies at a lower measuring frequency, increasing the measurement range of  $k_{accum}$ . (c) Schematic of BB-FDTR with alternate location for EOM2. In this configuration, the heterodyning occurs at the sample surface but the thermal phase response cannot be isolated. Labels identifying the make and models of the components can be found in Table 2.1.

The probe laser (532 nm, CW) passes through its own optical isolator (I-532) before encountering the beam sampler. The beam sampler is oriented such that only 10% of the incoming probe beam continues towards the sample. The co-aligned beams then pass through a polarizing beam splitter (PBS). The polarizing beam splitter allows the vertically polarized pump and probe beams to continue travelling

towards the sample. A 532 nm quarter wave plate (QWP) then circularly polarizes the light and a 20× objective (OBJ) is used to focus the lasers on to the sample surface. Based on the temperature change induced by the pump and the thermorefectance of the transducer, a modulation is induced in the reflectivity of the surface and hence in the reflected probe at  $f_1$ .

Table 2.1. Component list for schematics in Fig. 2.1.

Label	Component	Model/Description
I-532	532 nm isolator	Con-Optics M711A
I-488	488 nm isolator	Con-Optics M711C
BS	Beam sampler	Thor Labs BSF20-B
PBS	Polarizing beam splitter	Thor Labs PBS201
QWP	Quarter wave plate	Thor Labs WPQ05M-532
HWP	Half wave plate	Thor Labs WPH05M-488
LN	Focusing lens	Thor Labs, varying focal lengths
BP-488	488 nm bandpass filter	Thor Labs FL-488-3
BP-532	532 nm bandpass filter	Edmund Optics Techspec 65-155
PDA	Amplified photo diode	Thor Labs PDA36A
PD	Photo diode	Thor Labs DET10A
EOM1/EOM2	Electro-optic modulator	Con-Optics 350-80
	488 nm CW laser	Coherent Genesis MX
	532 nm CW laser	Coherent Verdi G2
OBJ	20x objective	Nikon CF Plan 20x ELWD
LA	Lock-in amplifier	SRS SR830
SG1/SG2	Signal generator	SRS SG384
MX	Electronic mixer	MiniCircuits ZAD-3+
LPF	Low pass filter	TTE LB3-120k-50-65B

When the pump and probe beams reflect from the sample surface, the circular polarization is reversed such that when the beams travel back through the quarter wave plate they become horizontally polarized. The horizontally polarized light is redirected towards the photo diode after passing back through the polarizing beam splitter. At this point, a lens is used to focus the light into EOM2. EOM2 induces an additional sinusoidal intensity modulation on the pump and probe beams at a frequency  $f_2$ . This modulation heterodynes the pump and probe beams [ $\sin(2\pi f_1 t)\sin(2\pi f_2 t)$ ], creating frequency modulation components at  $f_1 - f_2$  and  $f_1 + f_2$ . An optical band pass filter (BP-532) is used to attenuate the

pump beam and an amplified photo diode (PDA) converts the light into an electrical signal. The high frequency component of the signal ( $f_1 + f_2$ ) is filtered out using a low pass filter (LPF) and a lock-in amplifier (LA) measures the amplitude  $R$  and phase  $\phi$  of the signal at  $f_1 - f_2$ . Heterodyning the signal allows for the use of an amplified photo diode; in FDTR, an amplified photodiode cannot be used due to low bandwidth.

The frequency  $f_1 - f_2$  is chosen such that it is less than 102 kHz, allowing for the use of an SR-830 lock-in amplifier (range of 1 mHz to 102 kHz). The SR-830 lock-in amplifier has the advantage over an SR-844 lock-in in that it does not internally mix the signal with a square wave, which causes unwanted detection of the odd harmonics of the signal. The frequencies  $f_1$  and  $f_2$  are set such that  $f_1 - f_2$  is maintained constant at 86 kHz throughout the experiment. This frequency, along with the low pass filter, ensures that higher harmonics do not contribute to the signal since they are out of the SR-830 range. Furthermore, this frequency, at the upper end of the SR-830 range, also minimizes  $1/f$  noise without exceeding the low-pass cutoff of the filter ( $f_{\text{cutoff}} = 120$  kHz).

To make a meaningful measurement at  $f_1 - f_2$ , the lock-in amplifier needs a reference signal at  $f_1 - f_2$ . Since  $f_1 - f_2$  is not directly produced by either of the signal generators (SG) that drive the EOMs, it is generated using an electronic mixer (MX). The electronic mixer multiplies the input signals at  $f_1$  and  $f_2$  (from alternate outputs on signal generators 1 and 2) to create an output signal at  $f_1 + f_2$  and  $f_1 - f_2$ . An identical low pass filter attenuates the high frequency component and the component at  $f_1 - f_2$  is used as the reference for the lock-in amplifier.

EOM1 and EOM2 need high voltage electrical signals to induce modulation in the incoming light. These signals are provided by signal generators 1 and 2 and amplified by the EOM's amplifier. The shape of the voltage signal provided by the signal generator determines the shape of the light modulation. Signal generators 1 and 2 provide sinusoidal waveforms with frequency  $f_1$  and  $f_2$  and a peak-to-peak voltage of 0.2 V. This voltage produces a large thermal signal without significantly increasing the internal temperature of the EOMs, which causes drift in the DC offset. The DC offsets of the EOM amplifiers are carefully tuned to provide the maximum AC signal without waveform distortion.

During the experiment,  $f_1$  and  $f_2$  are concurrently swept by locking the time base of signal generators 1 and 2 and fixing the frequency difference. The measurement frequencies are defined by a heating frequency vector  $\bar{f}_1$  that provides the frequency for signal generator 1 to drive EOM1. The driving frequency of EOM2 is determined such that  $\bar{f}_2 = \bar{f}_1 + 86 \text{ kHz}$ . At each measurement point ( $\bar{f}_1$  is a 60 point vector uniformly spaced on a logarithmic axis between 200 kHz and 200 MHz), the amplitude and phase with respect to the reference are recorded from the lock-in amplifier.

To determine the heating frequency dependent thermal conductivity of the sample the phase difference between the surface temperature and heat flux  $\phi_{\text{thermal}}$  must be isolated. At any particular heating frequency, directly after the light reflects from the sample surface, the phase difference between the pump and the probe will be  $\phi_{\text{thermal}}$  (i.e., if  $\phi_{\text{pump}} = 0$ , then  $\phi_{\text{probe}} = \phi_{\text{thermal}}$ ). Both beams then travel through all the same optical components from the sample to the photo diode and both electrical signals encounter the same electrical components from the photo diode to the lock-in amplifier. Assuming the phase lag added to the signal from the optical components and photo diode is independent of the wavelength of the light, then  $\phi_{\text{pump}} = \phi_{\text{opt/elec}}$  and  $\phi_{\text{probe}} = \phi_{\text{thermal}} + \phi_{\text{opt/elec}}$  at the input of the lock-in amplifier, where  $\phi_{\text{opt/elec}}$  is the phase lag added from the optical and electrical components. The lock-in amplifier measures the phase with respect to the reference such that the measured phase differences  $\phi_{\text{pump,m}} = \phi_{\text{opt/elec}} - \phi_{\text{ref}}$  and  $\phi_{\text{probe,m}} = \phi_{\text{thermal}} + \phi_{\text{opt/elec}} - \phi_{\text{ref}}$ . Therefore,  $\phi_{\text{thermal}}$  can be isolated by subtracting the phase response from two experiments: one where the phase response of the probe is measured with a 532 nm band pass filter installed before the photo diode and another where the phase response of the pump is measured with a 488 nm band pass filter installed before the photo diode (i.e.,  $\phi_{\text{thermal}} = \phi_{\text{pump,m}} - \phi_{\text{probe,m}}$ ).

There are two options for the location of EOM2, (i) before the sample such that the probe beam is modulated before co-aligning with the pump beam [Fig. 2.1(c)], or (ii) after the sample, as in Fig. 2.1(b). When EOM2 is placed before the sample, the probe beam is modulated at  $f_2$  before incidence on the sample. Consequently, the heterodyning occurs at the sample surface, and only the probe beam is

heterodyned (since only the pump is inducing a significant temperature change and only the probe has a high thermorefectance). The phase difference measured in the probe is  $\phi_{\text{probe,m}} = \phi_{\text{thermal}} + \phi_{\text{opt/elec}} - \phi_{\text{ref}}$  and must be measured at  $f_1 - f_2$ . To isolate  $\phi_{\text{thermal}}$  as described above, the experiment is run twice to obtain the phase difference in the pump and subtract the two measurements. When EOM2 is before the sample, however, the pump beam never gets heterodyned, i.e., there is no frequency component at  $f_1 - f_2$ , and the subtraction of  $\phi_{\text{probe,m}}$  and  $\phi_{\text{pump,m}}$  cannot be made to isolate  $\phi_{\text{thermal}}$ . This configuration was the initial configuration and resulted in similar amplitude response but the phase was not resolvable.

To highlight the effectiveness of the heterodyning technique in the high frequency regime, the normalized temperature response and phase response for c-Si at  $T = 311$  K is measured with traditional FDTR and the BB-FDTR setup from  $f_1 = 200$  kHz to 200 MHz and shown in Fig. 2.2. FDTR measurements were made with amplified and unamplified photodiodes. At low frequencies, the phase data measured using each setup are the same with low noise (see inset in Fig. 2.2). At higher frequencies ( $>20$  MHz), however, the signal to noise ratio in the traditional FDTR setup decreases drastically because as the frequency increases, the signal size decreases but ambient and coherent noise increase. Coherent noise comes primarily from the high voltage signal carried by the cables connecting the EOM amplifier and EOM, which broadcasts at the same frequency as the thermal signal and is picked up by the cable carrying the temperature response between the photo diode and lock-in amplifier, which acts as an antenna. BB-FDTR increases the signal to noise ratio by completely eliminating coherent noise (signal is measured at  $f_1 - f_2$  while the EOMs are driven at  $f_1$  and  $f_2$ ) and reducing effects from ambient noise by measuring the signal at a much lower frequency,  $f_1 - f_2$ , and by using an amplified photodiode since  $f_1 - f_2$  is within the bandwidth of the amplified photo diode. Traditional FDTR with the same amplified photo diode up to the bandwidth ( $<10$  MHz) shows the same phase response as BB-FDTR, indicating consistent measurements irrespective of the photo diode. Thus, BB-FDTR yields a measurable signal for heating frequencies up to 200 MHz, an order of magnitude larger than traditional FDTR, and is only limited by the frequency restrictions of the EOMs. It is worth noting, however, that some noise is generated at 86

kHz due to crosstalk between the EOM cables, and spatial separation of the EOM amplifiers seems to be the most effective means of reduction.

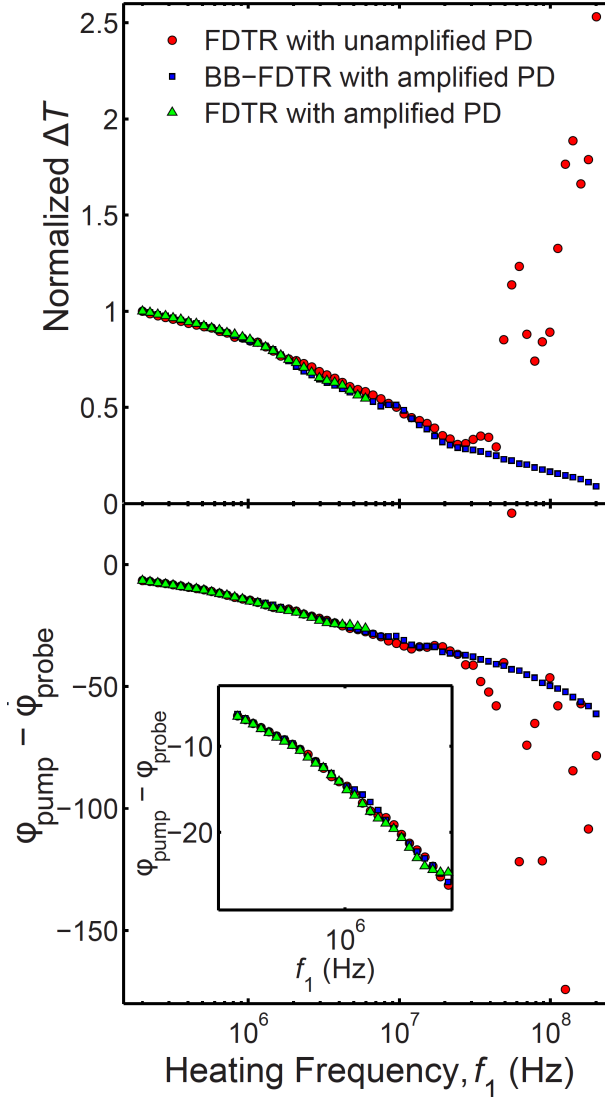


Fig. 2.2. Normalized temperature and phase response from traditional FDTR with an unamplified photo diode from 200 kHz to 200 MHz and an amplified photo diode up to the bandwidth of the photo diode and BB-FDTR experiments with an amplified photo diode for c-Si at  $T = 311$  K. In the low frequency regime, the data from traditional FDTR and BB-FDTR are the same and indicate no effect from using different photo diodes. As the frequency increases ( $f_1 > 20$  MHz), signal to noise ratios decrease in traditional FDTR. Heterodyning the signal allows for large signal to noise ratios up to a heating frequency of 200 MHz.

## A. Sample preparation

To increase signal to noise ratio, samples are sputtered with a thin surface coating, known as a transducer layer. The transducer layer, usually a metal film, reduces optical penetration depth, eliminating volumetric heating in the sample, and can be chosen to maximize the signal size by selecting a transducer material with a highly temperature-dependent reflectivity at the wavelength of the probe laser. The temperature-dependent reflectivity arises from the coefficient of thermorefectance of the transducer layer,  $\beta_{532 \text{ nm}}$ , and is given by  $\beta_{532 \text{ nm}} = [1/\rho_{0,532 \text{ nm}}][d\rho_{532 \text{ nm}}(T)/dT]$ , where  $\rho_{532 \text{ nm}}(T)$  is the temperature-dependent reflectivity and  $\rho_{0,532 \text{ nm}}$  is the nominal reflectivity of the transducer at the probe wavelength at ambient temperature. Thus, the periodic change in reflectivity is  $\rho_{532 \text{ nm}}(T_\omega) = \beta_{532 \text{ nm}}\rho_{0,532 \text{ nm}}T_\omega$ , where  $T_\omega$  is the periodic temperature variation of the sample surface [87]. The measured  $T_\omega$  can be increased by increasing the intensity of the absorbed pump laser, which is accomplished by choosing a transducer material with high absorptivity at the pump laser wavelength (488 nm). For BB-FDTR, gold is the ideal transducer material because it has high absorption at 488 nm and a high coefficient of thermorefectance at 532 nm [92].

The interface thermal conductance  $G$  between the transducer layer and the sample is an unknown, important parameter in the experiment. To increase the sensitivity to  $k_{\text{accum}}$  of the sample,  $G$  must be as large as possible. The gold transducer has a large mismatch in Debye temperature with silicon and their interface has a relatively low  $G$ . Therefore, a chromium adhesion layer is used between the sample and the gold transducer to increase  $G$  based on the similarity of Debye temperatures between chromium and silicon compared to gold and silicon ( $\theta_{\text{Debye,Cr}} = 630 \text{ K}$ ,  $\theta_{\text{Debye,Si}} = 645 \text{ K}$ ,  $\theta_{\text{Debye,Au}} = 170 \text{ K}$ ). For experimental results shown in this chapter, an 8 nm chromium adhesion layer and 56 nm gold transducer layer were deposited onto a single crystal, intrinsic silicon substrate (c-Si,  $<1 \times 10^{12} \text{ cm}^{-3}$  impurity atoms) using a Perkin Elmer 6J sputtering system in the Carnegie Mellon Nanofabrication Facility. Prior to the sputtering process, the native oxide layer on the c-Si substrate was removed with a buffered HF solution. Thicknesses of the chromium and gold layers were measured with x-ray reflectivity (XRR).

## B. Determining pump and probe laser spot size

The spot sizes of the pump and probe beams must be known to analyze the data and are measured using a knife-edge profiling technique. First, a silicon wafer coated with gold is cleaved to create a sharp edge and the sample is mounted on a micromanipulator stage with a resolution of 62.5 nm. To focus the beams at the knife-edge, the BB-FDTR signal is maximized using the lock-in amplifier. After focusing, the modulation is turned off and the pump and probe DC laser intensities reflected from the sample are measured simultaneously as the micromanipulator translates (see Fig. 2.3). Initially, the silicon sample does not interfere with the beam path and no light is reflected into the photodiodes (zero voltage is measured). As the stage translates, the silicon sample enters the beam path and a portion of each beam is reflected into separate photodiodes. Ultimately, when the stage translates far enough, both beams are completely reflected and the maximum voltage is measured.

Since the measured voltage represents a spatial integration of a Gaussian laser beam incident on the photodiode, fitting a cumulative normal distribution function yields a spatial profile of the pump and probe beams at the surface of the silicon sample, as seen in Fig. 2.3. An effective  $1/e^2$  spot size ( $r_{\text{spot}}$ ) is calculate with

$$r_{\text{spot}} = \sqrt{r_{\text{spot,pump}}^2 + r_{\text{spot,probe}}^2/2} \quad , \quad (2.1)$$

where  $r_{\text{spot,pump}}$  and  $r_{\text{spot,probe}}$  are the  $1/e^2$  radii of the pump and probe beams. The data from Fig. 2.3 yield an effective spot radius of 3.5  $\mu\text{m}$ .

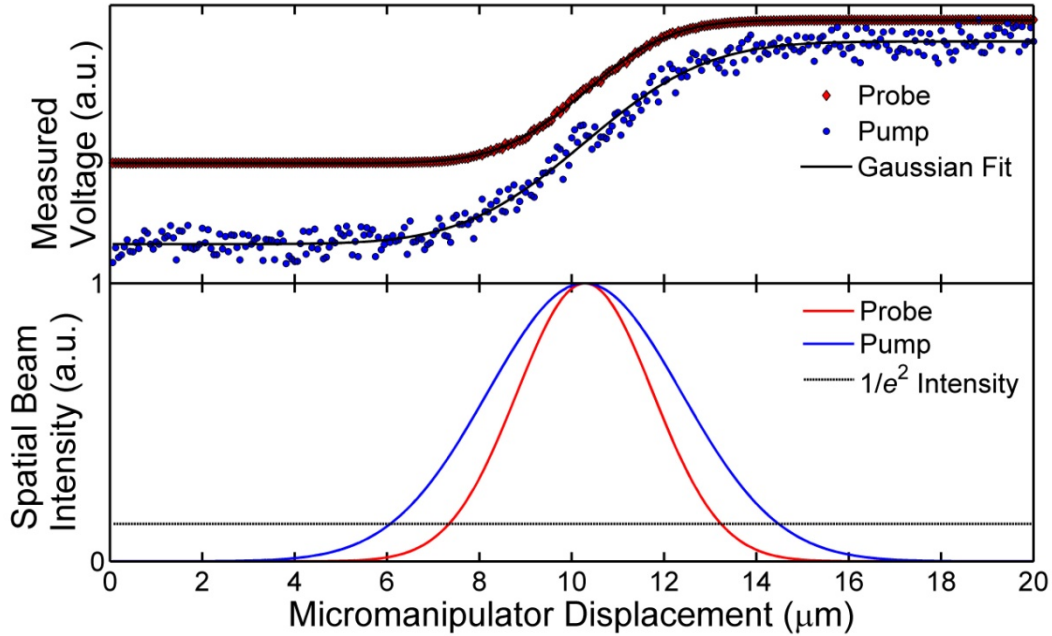


Fig. 2.3. A knife-edge is used to determine the beam profile. The data are fit with a cumulative normal distribution function to find the  $1/e^2$  radius of the pump and probe beams. These values are used to find the effective spot size  $r_{\text{spot}}$ .

### III. Analytical modeling

The phase data measured in a BB-FDR experiment are fit to an analytical solution for the frequency domain temperature response for a multi-layered structure in cylindrical coordinates that was developed by Cahill [70]. It accounts for the Gaussian shape of the heat flux (pump) and calculates an average temperature response based on the Gaussian weighted sampling of the probe beam. In the following subsections the heat transfer problems relevant to BB-FDTR are formulated and solved. First, the simplest problem (i.e., planar heating on a semi-infinite medium) is described. That solution is built upon to ultimately determine the solution that most accurately describes BB-FDTR (i.e., periodic, spatially Gaussian surface heating on a layered structure).

#### A. Planar heating on a semi-infinite medium

First, consider the transient heat conduction problem of periodic, planar heating incident on a semi-infinite medium, as shown in Fig. 2.4. The spatial and temporal temperature profile  $\theta(t, z)$  and heat flux profile  $F(t, z)$  are solved from the transient heat diffusion equation in one dimension given by

$$C \frac{\partial \theta}{\partial t} = k \frac{\partial^2 \theta}{\partial z^2}, \quad (2.2)$$

where  $C$  and  $k$  are the volumetric heat capacity and thermal conductivity of the material. Since the medium is semi-infinite, the temperature as  $z \rightarrow \infty$  approaches the initial temperature of the medium. For simplicity, define  $\theta(t = 0, z) = 0$  and thus  $\theta(t, z \rightarrow \infty) = 0$ . The boundary condition at  $z = 0$  is a periodic surface heat flux  $F_0$  with an angular frequency  $\Omega$  and is given by

$$F_0 = -k \left. \frac{\partial \theta}{\partial z} \right|_{z=0} = H e^{i\Omega t}, \quad (2.3)$$

where  $H$  is the magnitude of the heat flux absorbed by the sample.

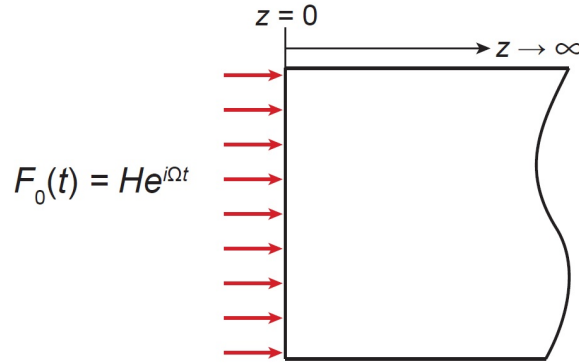


Fig. 2.4. Semi-infinite slab with thermal conductivity  $k$  and volumetric heat capacity  $C$  subject to a planar, periodic surface heat flux.

Since the time dependence of the temperature follows the heating and varies as  $e^{i\Omega t}$ , separation of variables is performed to reduce the governing equation and boundary conditions to

$$\frac{d^2 T}{dz^2} = \frac{i\Omega C}{k} T, \quad (2.4a)$$

$$\hat{F}_0 = -k \left. \frac{\partial T}{\partial z} \right|_{z=0} = H, \quad (2.4b)$$

$$T|_{z \rightarrow \infty} = 0, \quad (2.4c)$$

where  $T(z)$  and  $\hat{F}_0$  are the time-independent temperature profile and surface heating term. The solution for the spatial temperature and heat flux  $q''(z)$  profiles in matrix form is given by

$$\boldsymbol{\Psi}^z = \boldsymbol{\chi} \mathbf{A}^z \mathbf{B}, \quad (2.5a)$$

$$\boldsymbol{\Psi}^z = \begin{bmatrix} T(z) \\ q''(z) \end{bmatrix}, \quad (2.5b)$$

$$\boldsymbol{\chi} = \begin{bmatrix} 1 & 1 \\ \gamma & -\gamma \end{bmatrix}, \quad (2.5c)$$

$$\mathbf{A}^z = \begin{bmatrix} e^{-\lambda z} & 0 \\ 0 & e^{\lambda z} \end{bmatrix}, \quad (2.5d)$$

$$\mathbf{B} = \begin{bmatrix} B^- \\ B^+ \end{bmatrix}, \quad (2.5e)$$

where  $z$  position is indicated by the superscript. Here  $\lambda = \sqrt{\frac{i\Omega C}{k}}$ ,  $\gamma = k\lambda$ , and  $B^-$  and  $B^+$  are constants of integration. To find  $\mathbf{B}$ , the boundary conditions at  $z \rightarrow \infty$  and  $z = 0$  are used. In matrix form, these are

$$\boldsymbol{\chi} \mathbf{A}^{z \rightarrow \infty} \mathbf{B} = \begin{bmatrix} 0 \\ q''(z \rightarrow \infty) \end{bmatrix} = \boldsymbol{\Psi}^{z \rightarrow \infty}, \quad (2.6a)$$

$$\begin{bmatrix} T(z=0) \\ \hat{F}_0 \end{bmatrix} = \boldsymbol{\Psi}^{z=0} = \boldsymbol{\chi} \mathbf{B}. \quad (2.6b)$$

To satisfy these boundary conditions  $\mathbf{B} = \begin{bmatrix} H \\ \gamma \end{bmatrix}$ . Substituting into Eq. (2.5a) yields the spatial temperature and heat flux profiles as

$$\begin{bmatrix} T(z) \\ q''(z) \end{bmatrix} = \begin{bmatrix} 1 & 1 \\ \gamma & -\gamma \end{bmatrix} \begin{bmatrix} e^{-\lambda z} & 0 \\ 0 & e^{\lambda z} \end{bmatrix} \begin{bmatrix} H \\ \gamma \end{bmatrix}. \quad (2.7)$$

The time-dependent temperature and heat flux profiles  $\theta(t, z)$  and  $F(t, z)$  are determined by multiplying Eq. (2.7) with  $e^{i\Omega t}$ .

## B. Planar heating in a layered sample

As described above, in thermoreflectance experiments the sample is usually a layered sample due to the necessity of a transducer layer. In this section, I solve for the spatial temperature and heat flux profiles in a N-layered structure with periodic, planar surface heating where the N<sup>th</sup> layer is semi-infinite, as depicted in Fig. 2.5. After separation of variables, the governing equation for temperature in the n<sup>th</sup> layer is

$$\frac{d^2 T_n}{dz^2} = \frac{i\Omega C_n}{k_n} T_n, \quad (2.8)$$

where the subscript n on  $k_n$ ,  $C_n$ , and  $T_n$  indicates the thermal conductivity, heat capacity, and time-independent temperature of the n<sup>th</sup> layer.

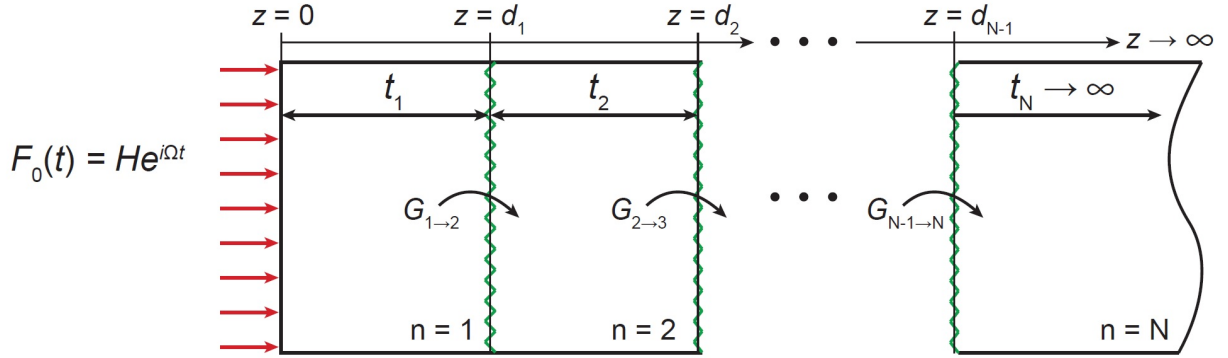


Fig. 2.5. N-layered material with each layer having thermal conductivity, heat capacity, and thickness  $k_n$ ,  $C_n$ , and  $t_n$  subject to periodic, planar surface heating. An interface conductance  $G_n$  exists between layers n and n+1.

Equation (2.8) is solved for the temperature and heat flux profiles in the n<sup>th</sup> layer. The solution is similar to that of Eq. (2.4) and in matrix form is

$$\Psi_n^z = \chi_n \mathbf{A}_n^z \mathbf{B}_n, \quad (2.9a)$$

$$\Psi_n^z = \begin{bmatrix} T_n(z) \\ q_n''(z) \end{bmatrix}, \quad (2.9b)$$

$$\boldsymbol{\chi}_n = \begin{bmatrix} 1 & 1 \\ \gamma_n & -\gamma_n \end{bmatrix}, \quad (2.9c)$$

$$\mathbf{A}_n^z = \begin{bmatrix} e^{-\lambda_n z} & 0 \\ 0 & e^{\lambda_n z} \end{bmatrix}, \quad (2.9d)$$

$$\mathbf{B}_n = \begin{bmatrix} B^- \\ B^+ \end{bmatrix}_n, \quad (2.9e)$$

were  $\lambda_n = \sqrt{\frac{i\Omega C_n}{k_n}}$  and  $\gamma_n = k_n \lambda_n$ . The boundary conditions are used to determine the constants of integration for each layer  $\mathbf{B}_n$ . The boundary conditions for the last and first layers are similar to the single layer case and are

$$\boldsymbol{\chi}_N \mathbf{A}_N^{z \rightarrow \infty} \mathbf{B}_N = \begin{bmatrix} 0 \\ q_N''(z \rightarrow \infty) \end{bmatrix} = \boldsymbol{\Psi}_N^{z \rightarrow \infty}, \quad (2.10a)$$

$$\begin{bmatrix} T_1(z=0) \\ \hat{F}_0 \end{bmatrix} = \boldsymbol{\Psi}_1^{z=0} = \boldsymbol{\chi}_1 \mathbf{B}_1. \quad (2.10b)$$

Additionally, there are boundary conditions at each interface. Particularly, there is an interface thermal conductance between layer  $n$  and layer  $n+1$  ( $G_n$ ), such that the temperature and heat flux profiles on either side of the interface are related by

$$\boldsymbol{\Psi}_n^{z=d_n} = \mathbf{G}_{n \rightarrow n+1} \boldsymbol{\Psi}_{n+1}^{z=d_n} \quad \rightarrow \quad \boldsymbol{\chi}_n \mathbf{A}_n^{z=d_n} \mathbf{B}_n = \mathbf{G}_{n \rightarrow n+1} \boldsymbol{\chi}_{n+1} \mathbf{A}_{n+1}^{z=d_n} \mathbf{B}_{n+1}, \quad (2.11)$$

where  $\mathbf{G}_{n \rightarrow n+1} = \begin{bmatrix} 1 & 1/G_n \\ 0 & 1 \end{bmatrix}$  and is determined by balancing heat fluxes across the interface.

Equations (2.10) and (2.11) are used to determine  $\boldsymbol{\Psi}_N^{z \rightarrow \infty}$  in terms of  $\boldsymbol{\Psi}_1^{z=0}$ . Note that  $\mathbf{A}_n^{z_1} [\mathbf{A}_n^{z_2}]^{-1} = \mathbf{A}_n^{z_1 - z_2}$  and  $\boldsymbol{\mu}_n = \boldsymbol{\chi}_n \mathbf{A}_n^{z=t_n} [\boldsymbol{\chi}_n]^{-1}$  is defined for simplification. The result is

$$\boldsymbol{\Psi}_N^{z \rightarrow \infty} = \left( \prod_{j=2}^N \boldsymbol{\mu}_{2-j+N} [\mathbf{G}_{1-j+N \rightarrow 2-j+N}]^{-1} \right) \boldsymbol{\mu}_1 \boldsymbol{\Psi}_1^{z=0}. \quad (2.12)$$

The resulting form of Eq. (2.12) is

$$\Psi_N^{z \rightarrow \infty} = \overbrace{\begin{bmatrix} p_{11} & p_{12} \\ p_{21} & p_{22} \end{bmatrix}}^{\mathbf{P}} \Psi_1^{z=0}. \quad (2.13)$$

The time-independent, surface temperature at  $z = 0$  is determined as

$$T_1(z = 0) = -\frac{p_{12} \hat{F}_0}{p_{11}}. \quad (2.14)$$

Once the surface temperature is known, the  $\mathbf{B}$  vector for any layer can be determined from Eqs. (2.10) and (2.11). From there it is straightforward to determine the time-independent temperature and heat flux profiles in the  $n^{\text{th}}$  layer using  $\Psi_n^z = \chi_n \mathbf{A}_n^z \mathbf{B}_n$ . The time-dependent temperature and heat flux profiles  $\theta_n(t, z)$  and  $F_n(t, z)$  are determined by multiplying  $T_n(z)$  and  $q_n''(z)$  with  $e^{i\Omega t}$ .

### C. Including spatially Gaussian surface heating

In most thermoreflectance experiments, planar surface heating is not a valid approximation because (i) signal to noise ratio increases with decreasing spot size, making smaller spot sizes more desirable and (ii) often spot size is used as an experimental variable (e.g., determine thermal conductivity as a function of spot size). For these reasons it is important to account for the effect of spot size (i.e., two-dimensional heat transport) when fitting data. In this section, I outline how to determine the temperature profile in an N-layer sample that includes the Gaussian-shaped surface heating profile apparent in laser-based thermoreflectance experiments.

Due to the cylindrical symmetry of the problem, I solve the 2-D heat diffusion equation in cylindrical coordinates [Eq. (2.15a)] with a Gaussian-shaped surface heating profile [Eq. (2.15b)]

$$C_n \frac{\partial \theta_n}{\partial t} = k_n \left[ \frac{\partial^2 \theta_n}{\partial z^2} + \frac{\eta_n}{r} \frac{\partial}{\partial r} \left( r \frac{\partial \theta_n}{\partial r} \right) \right], \quad (2.15a)$$

$$F_0 = -k_1 \left. \frac{\partial \theta_1}{\partial z} \right|_{z=0} = \frac{4H}{r_{\text{spot,pump}}^2} e^{i\Omega t} e^{-2r^2/r_{\text{spot,pump}}^2}. \quad (2.15b)$$

Here,  $\theta_n(t, z, r)$  is a function of time, depth into the layer, and the radial coordinate  $r$ ,  $\eta_n$  is the ratio of the thermal conductivities in the  $r$ - and  $z$ -directions (a value of  $\eta_n = 1$  indicates an isotropic material), and  $r_{\text{spot,pump}}$  is the  $1/e^2$  pump beam radius.

Similar to the preceding analysis, separation of variables is performed. Furthermore, since the problem is cylindrically symmetric a Hankel transform is performed to eliminate the  $r$ -dependence [93]. Doing so simplifies Eq. (2.15) to

$$\frac{d^2 T_n}{dz^2} = \frac{C_n i\Omega + k_n \eta_n \kappa^2}{k_n} T_n, \quad (2.16a)$$

$$\hat{F}_0 = -k_1 \left. \frac{\partial T_1}{\partial z} \right|_{z=0} = H e^{-\kappa^2 r_{\text{spot,pump}}^2 / 8}, \quad (2.16b)$$

where  $T_n(z, \kappa)$  is the time-independent, transformed temperature in the  $n^{\text{th}}$  layer,  $\hat{F}_0$  is the time-independent, transformed surface heating profile, and  $\kappa$  is the Hankel variable. The solution procedure is the same as was done in the preceding section, however, now  $\lambda_n = \sqrt{\frac{C_n i\Omega + k_n \eta_n \kappa^2}{k_n}}$  and  $\hat{F}_0$  is redefined in Eq. (2.16b). The time-independent, transformed surface temperature  $T_0(z, \kappa)$  has the same form as Eq. (2.14) and can be used to determine  $\mathbf{B}$  for any layer to find the time-independent temperature and heat flux profiles in the  $n^{\text{th}}$  layer with  $\boldsymbol{\psi}_n^z = \boldsymbol{\chi}_n \mathbf{A}_n^z \mathbf{B}_n$ .

To determine the surface temperature  $\theta_1(t, z = 0, r)$  I multiply by  $e^{i\Omega t}$  and perform an inverse Hankel transform such that

$$\theta_1(t, z = 0, r) = e^{i\Omega t} \int_0^\infty T_1(z = 0, \kappa) J_0(\kappa r) \kappa d\kappa, \quad (2.17)$$

where  $J_0(\kappa r)$  is the zeroth order Bessel function of the first kind. In a thermorefectance experiment, an unmodulated probe beam measures the weighted average of the temperature distribution over its Gaussian-shaped beam (with a  $1/e^2$  radius  $r_{\text{spot,probe}}$ ). Mathematically, the weighted temperature  $\bar{\theta}_1$  is determined from [70]

$$\bar{\theta}_1(t, z = 0) = \int_0^{\infty} \theta_1(t, z = 0, r) \frac{4}{r_{\text{spot,probe}}^2} e^{-2r^2/r_{\text{spot,probe}}^2} 2\pi r dr . \quad (2.18)$$

Substituting Eq. (2.17) into Eq. (2.18) and rearranging yields a single integral over  $\kappa$ , which must be evaluated numerically

$$\bar{\theta}_1(t, z = 0) = 2\pi e^{i\Omega t} \int_0^{\infty} T_1(z = 0, \kappa) e^{-\kappa^2 r_{\text{spot,probe}}^2/8} \kappa d\kappa . \quad (2.19)$$

Equation (2.19) is the temporal temperature change about the initial temperature of the solid at the surface of the solid weighted over the  $r$ -direction with a Gaussian-shaped weight function.

#### D. Sensitivity

A sensitivity analysis was performed to examine how sensitive Eq. (2.19) is to different input parameters,  $\beta$ , over the frequency range of BB-FDTR (200 kHz to 200 MHz). The model requires nominal values for the transducer layer thickness  $t_{\text{tr}}$ , the transducer layer thermal conductivity  $k_{\text{tr}}$ , the volumetric heat capacity of the transducer layer  $C_{\text{tr}}$ , the thermal conductivity of the substrate  $k_{\text{sub}}$ , the volumetric heat capacity of the substrate  $C_{\text{sub}}$ , the interface conductance between the transducer layer and the substrate  $G$ , and the laser spot radius  $r_{\text{spot}}$ . From Ref. [94], the sensitivity,  $S_{\beta}$ , is the logarithmic derivative of the phase response,  $\Phi$ , with respect to a change in one of the parameters,  $\beta$ , and is defined by

$$S_{\beta} = \frac{d\ln(\Phi)}{d\ln(\beta)} \quad (2.20)$$

$$\beta = t_{\text{tr}}, k_{\text{tr}}, C_{\text{tr}}, k_{\text{sub}}, C_{\text{sub}}, r_{\text{spot}}, G$$

Table 2.2. Nominal values for fitting and the sensitivity analysis and the uncertainty ranges used to generate the shaded error regions in Fig. 2.7.

$\beta$	Nominal Value	Uncertainty Range
$t_{tr}$	64 nm	$\pm 5\%$
$C_{tr}$	2470 kJ/m <sup>3</sup> -K	n/a
$k_{tr}$	110 W/m-K	$\pm 5\%$
$k_{sub}$	143 W/m-K	n/a
$C_{sub}$	1689 kJ/m <sup>3</sup> -K	n/a
$r_{spot}$	3.2 $\mu$ m	$\pm 0.1 \mu$ m
$G$	210 MW/m <sup>2</sup> -K	$\pm 10$ MW/m <sup>2</sup> -K
$\Delta\phi_{thermal}$	n/a	$\pm 0.2^\circ$

The results of the sensitivity analysis about the nominal values (shown in Table 2.2) are shown in Fig. 2.6(a) for a 1% change in  $\beta$ . The sensitivity when  $G = 60$  MW/m<sup>2</sup>-K is shown in Fig. 2.6(b) and the sensitivity when  $k_{sub} = 10$  W/m-K is shown in Fig. 2.6(c). A comparison of Fig. 2.6(a) and 2.6(b) shows that at higher heating frequencies the experiment is more sensitive to  $k_{sub}$  when  $G$  is larger. For this reason the chromium adhesion layer is used to increase  $G$ . A comparison of Fig. 2.6(a) and 2.6(c) shows lower overall sensitivity to  $G$  but reduced sensitivity to  $k_{sub}$  in substrates with lower bulk thermal conductivity. While the heat capacity of the transducer and substrate, the thickness of the transducer, and the thermal conductivity of the transducer are moderately sensitive, they are well known values in the fitting. Additionally, the spot size value used in fitting is the most sensitive at lower heating frequencies, where  $L_p \sim r_{spot,pump}$ . Notably, the heat capacity of the transducer makes the signal insensitive to  $k_{sub}$  above  $\sim 200$  MHz, and future increases in the modulation frequency range need to be paired with thinner transducers to expand the measurement range of  $k_{accum}$ .

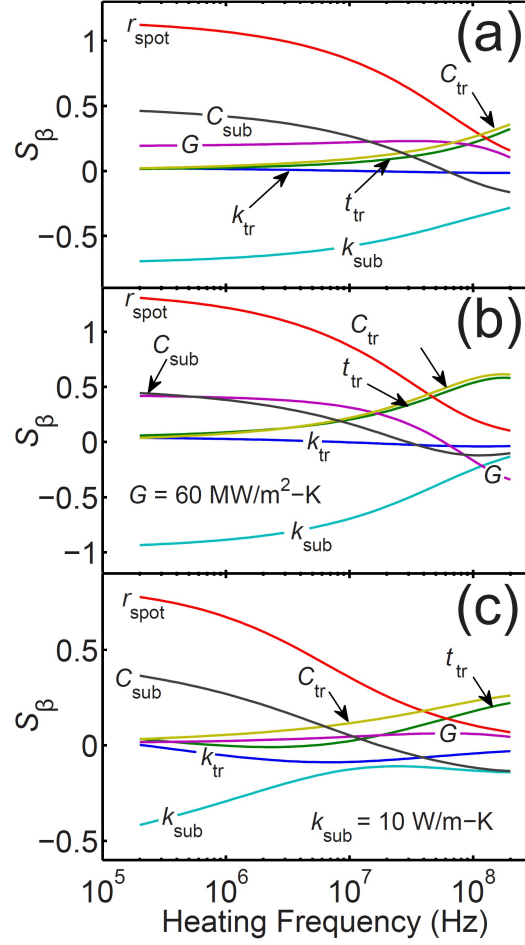


Fig. 2.6. (a) Sensitivity to a 1% change in nominal parameters found in Table 2.2, as defined by Eq. (2.20). The effect on the sensitivity from (b) decreased interface thermal conductance and (c) decreased substrate thermal conductivity.

#### IV. Fitting BB-FDTR data with the heat diffusion equation

The phase response measured in BB-FDTR is fit to the phase response predicted by Eq. (2.19) for  $k_n$  of the substrate (usually  $n = 2$  for the substrate) using a nonlinear regression until the mean square error (variance of the error) is minimized. In the high frequency limit, where  $L_p \ll r_{\text{spot}}$ , the isotherms of the temperature profile will be relatively planar. The temperature response at the surface can be approximated with the 1-D, planar heating solution given by Eq. (2.7) as

$$T_{\text{planar}}(z = 0) = \frac{H}{\sqrt{kC\Omega}} \exp[i(\Omega t - \pi/4)] . \quad (2.21)$$

In this case, the amplitude of the temperature response is inversely proportional to  $\sqrt{k\Omega}$  and the temperature response lags the heat flux by  $\pi/4$  radians in phase. For the two layered transducer/substrate case, the temperature response is still inversely proportional to  $\sqrt{\Omega}$  but the phase is no longer  $\pi/4$ .

In the experiments, the signal to noise ratio can be approximated by the amplitude of the temperature response (i.e., the larger the amplitude the larger the signal to noise ratio). At lower heating frequencies, the signal to noise ratio is larger and increases with decreasing sample thermal conductivity (lower signal to noise ratios at lower temperature due to the temperature dependence of thermal conductivity). At high heating frequencies, the signal size decreases, and the heterodyne approach is critical.

The signal to noise ratio increases with increasing pump power, however, large pump powers can cause unwanted DC heating of the sample. Per Ref. [70], the DC temperature rise of the sample can be estimated by taking the low frequency limit of Eq. (2.19),

$$\Delta T_{\text{DC}} = \frac{A_o}{2\sqrt{\pi}r_{\text{spot}}k_{\text{bulk}}} , \quad (2.22)$$

where  $A_o$  is the laser power absorbed by the sample and  $k_{\text{bulk}}$  is the bulk thermal conductivity of the sample. In BB-FDTR,  $A_o$  was measured to be 3% of the total pump power and 5% of the total probe power. The DC temperature rise is accounted for by adding  $\Delta T_{\text{DC}}$  to the experimental temperature set point, which is controlled by a cryostat. For the data shown in Fig. 2.2, the measurement was performed at  $T = 300$  K and  $\Delta T_{\text{DC}} = 11$  K making the effective measurement temperature 311 K.

## A. Fitting procedure

In this section the procedure for determining  $k$  vs.  $L_p$  is described for an intrinsic c-Si sample at  $T = 311$  K with nominal fitting values shown in Table 2.2. For this sample, XRR is used to measure  $t_{\text{tr}}$  and  $k_{\text{tr}}$  is measured using a four-point resistivity measurement and the Wiedemann-Franz law.  $C_{\text{tr}}$  and  $C_{\text{sub}}$  are assumed to be heating frequency independent and taken as the bulk value for gold and the bulk value for c-Si. This is because the long phonon MFPs probed by BB-FDTR contribute significantly to thermal

conductivity but not to heat capacity (<1%) [45].  $k_{\text{bulk}}$  is determined from Ref. [95] and  $r_{\text{spot}}$  was measured using the knife-edge profiling technique outlined in the preceding section. To determine the value of  $G$ , the last 15 points of the phase data are fit until mean square fitting error is minimized since  $G$  is more sensitive in the high frequency regime (see Fig. 2.6).

Measured phase vs. heating frequency for silicon at  $T = 311$  K is shown in Fig. 2.7(a). The result of fitting these data with Eq. (2.19) for a constant (frequency-independent) value of  $k_{\text{sub}}$  is shown in Fig. 2.7(a). Clearly the fit is poor, with the fitted value of  $k_{\text{sub}} = 99$  W/m-K underestimates the bulk value of silicon by 32%. Because fitting the entire frequency range to a constant value thermal conductivity does not yield the bulk value, the heating frequency dependence of measured thermal conductivity is investigated. To do so, the phase response is divided into sections, as seen in Fig. 2.7(a), and a window fitting scheme is used. If, for example, a fitting frequency range of 13 points is defined, then Window 1 includes points 1 through 13 of the phase data, Window 2 includes points 2 through 14, and Window  $i$  includes points  $i$  through  $i + 12$ . A value for thermal conductivity is fit for each window ( $k_i$ ) using Eq. (2.19) and plotted at the median frequency of each fitting frequency range ( $f_i$ ) as seen in Fig. 2.7(a). Transformation of the  $x$ -axis from frequency to  $L_c = L_{p,i} = \sqrt{k_i/C\pi f_{1,i}}$  yields  $k$  vs.  $L_p$ , shown in Fig. 2.7(b). Relating the data shown in Fig. 2.7(b) to  $k_{\text{accum}}$  is discussed later in this dissertation.

In BB-FDTR experiments, both the normalized amplitude of the surface temperature oscillation and the phase response data are recorded. The phase response data are used when fitting thermal conductivity because it has a higher signal to noise ratio due to the insensitivity to fluctuations in laser power. For every data set, however, one to three points at multiples of 13.5 MHz deviate up to  $20^\circ$  from the expected trend. These spurious points result from interactions between the high-voltage cables that drive EOM1 at  $f_1$  and EOM2 at  $f_2$ . The large noise signal at  $f_1 - f_2$  persists in the probe beam even when the pump laser is turned off, which is evidence that it is directly imposed by EOM2. These points have been removed from the data sets.

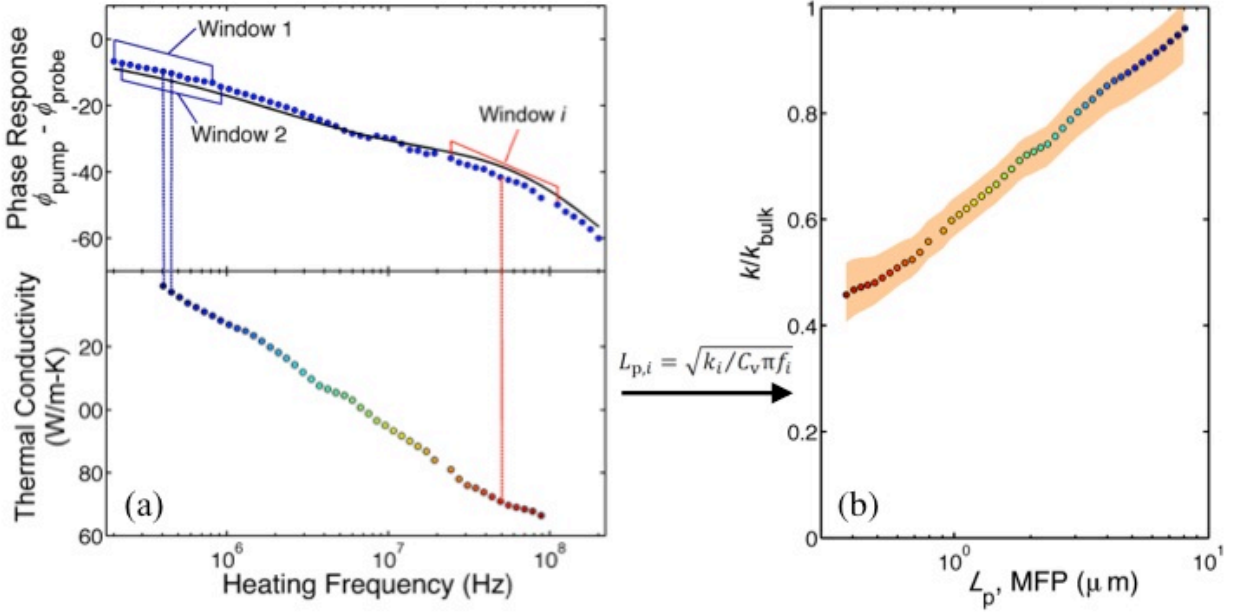


Fig. 2.7. (a) The phase response data are divided into different windows. Each window is fit to a value of thermal conductivity and plotted at the median frequency of that fitting range. (b) The fitted thermal conductivity and median frequency for each window is used to generate the  $k$  vs.  $L_p$ .

## B. Effect of fitting window size

Typically, a fitting frequency range of 13 points is used. This choice is justified to provide enough points for an accurate fit while still allowing for a large range of  $k$  vs.  $L_p$  to be measured. The effect of different fitting frequency ranges is shown in Fig. 2.8, where  $k$  vs.  $L_p$  is plotted with 7-point, 13-point, and 19-point fitting windows. As the fitting window is increased, the curves become smoother but a smaller range of  $L_p$  is probed. Most importantly, however, 7-point, 13-point, and 19-point fitting windows show no discernible change in the shape (slope) of  $k$  vs.  $L_p$ .

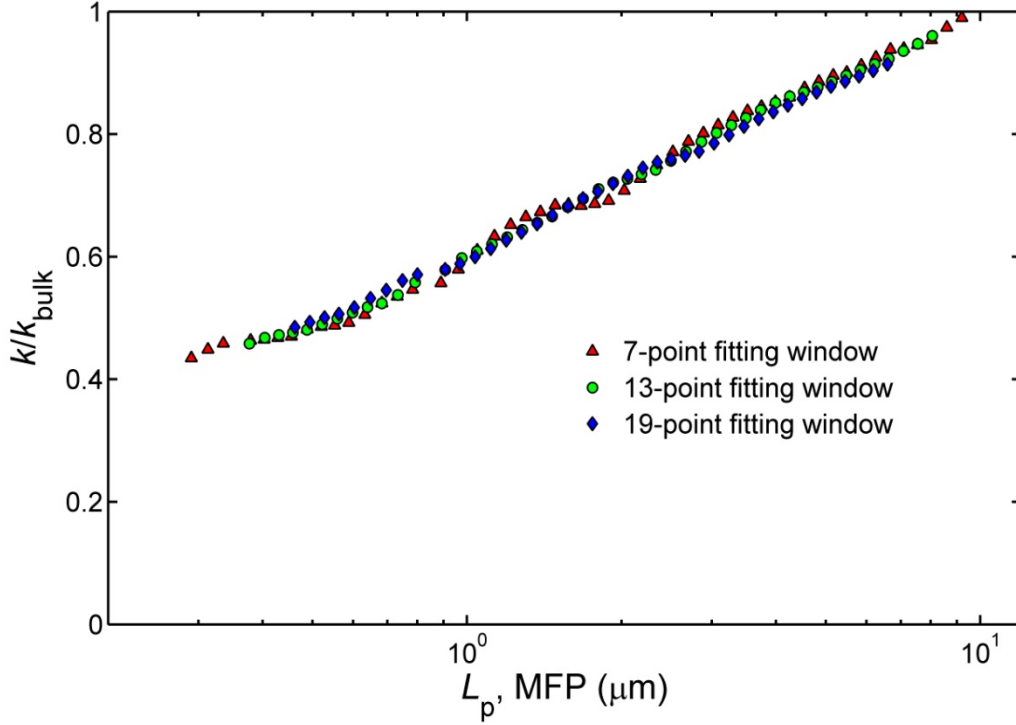


Fig. 2.8.  $k$  vs.  $L_p$  for intrinsic c-Si ( $T = 311$  K) is shown for 7-point, 13-point, and 19-point fitting windows. Increasing the window size decreases the range of  $L_p$ . Relative to the 13-point fits, fitting windows of 7 and 19 points do not change the shape of  $k$  vs.  $L_p$ .

### C. Uncertainty in $k$ vs. $L_p$ measurements

Uncertainty in the measurement  $\Delta k$  is indicated as the shaded region in Fig. 2.7(b) and was calculated as follows,

$$\Delta k = \sqrt{\sum_{\beta} (\Delta k_{\beta})^2}, \quad \Delta k_{\beta} = \frac{\partial k_{\beta}}{\partial \beta} \Delta \beta \quad (2.23)$$

$$\beta = t_{tr}, k_{tr}, r_{spot}, G, \Delta \varphi_{thermal} ,$$

where  $\Delta k_{\beta}$  indicates the uncertainty from the selected modeling parameters  $\beta$ . The uncertainty due to  $\Delta k_{\beta}$  depends on the sensitivity to that parameter  $\partial k_{\beta} / \partial \beta$  and the uncertainty in that parameter  $\Delta \beta$ . Uncertainty ranges for the selected values of  $\beta$  are shown in Table 2.2. The uncertainty associated with  $G$  was determined first by changing the other modeling parameters and fitting the high frequency phase data to minimize mean square error. The effective range of  $G$  used for calculating  $\Delta k$  is  $\pm 10$  MW/m<sup>2</sup>-K.

A DC phase shift to the measured thermal phase response over all frequencies  $\Delta\phi_{\text{thermal}}$  is considered as a source of uncertainty. The effect of this shift on  $k$  vs.  $L_p$  is shown in Fig. 2.9. Since all data are measured at the same frequency ( $f_1 - f_2$ ), there is no reason to believe that there would be a heating frequency dependent shift/error in the measured phase data. Thus, to examine the propagation of an error in the measured phase to  $k$  vs.  $L_p$ , the c-Si ( $T = 311$  K) phase data are refit with a  $\pm 0.2^\circ$  DC shift in phase. The result indicates that  $k$  vs.  $L_p$  is most sensitive to a DC phase shift at low frequencies and decreases with increasing heating frequency. The largest change in  $k$  vs.  $L_p$  is small ( $\pm 3\%$  at the lowest frequency).

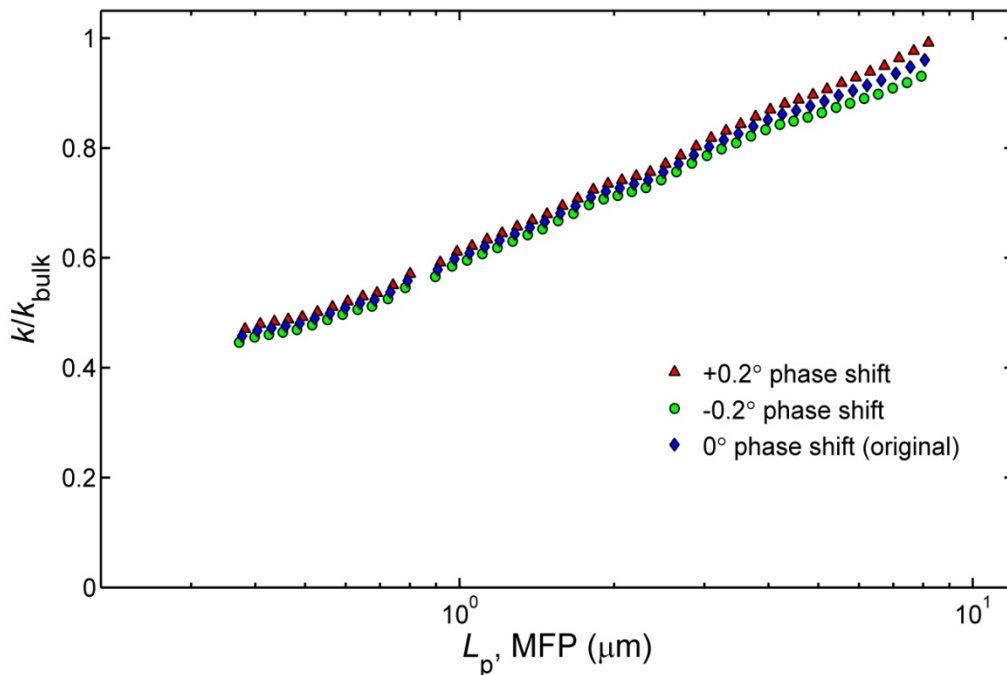


Fig. 2.9.  $k$  vs.  $L_p$  for c-Si at  $T = 311$  K is shown with a  $\pm 0.2^\circ$  constant phase shift in the measured phase response. The largest effect comes at longer  $L_p$ , with a maximum  $\pm 3\%$  deviation from the original  $k$  vs.  $L_p$ .

## V. Summary

Here, I present the instrumentation for BB-FDTR, an experimental technique to induce and observe nondiffusive thermal transport. BB-FDTR uses a heterodyne technique which allows for high heating frequencies in the pump beam but measurement of the thermal signal in the probe beam at a much

lower frequency where high signal to noise ratio is achieved. A window fitting scheme is used, where the unknown fitting variables are the thermal conductivity within that window and the interface thermal conductance between the transducer and sample. The value of  $G$  should be maximized to increase sensitivity to the substrate thermal conductivity. I present measurements of  $k$  vs.  $L_p$  for c-Si at  $T = 311$  K using BB-FDTR. The relationship between  $k$  vs,  $L_p$  and  $k_{\text{accum}}$  is discussed in the following chapters.

### 3. NONDIFFUSIVE THERMAL TRANSPORT IN Si-BASED MATERIALS

#### I. Overview

The thermal conductivity relates the heat flux and temperature gradient in a material through the Fourier Law and results from the cumulative contributions of phonons with a broad range of MFPs. The spectral MFP distribution is critical in nanostructured materials and devices, where size-effects selectively scatter phonons or create non-Fourier conduction based on individual phonon MFPs. Such effects impact heat dissipation in nanoelectronics and photonics, as well as the design of nanostructured thermoelectric materials with reduced thermal conductivity [1-3,19,26,31,41,45,96]. Due to its ubiquity in electronics, crystalline silicon (c-Si) has emerged as the prototypical material of study, yet controversy persists on what phonon MFPs dominate thermal transport, even in the bulk material. Kinetic theory defines the thermal conductivity as  $k = C v_s \Lambda_g / 3$ , where  $\Lambda_g$  is the average (or gray) MFP. For c-Si, kinetic theory yields  $\Lambda_g = 41$  nm at  $T = 300$  K [37]. This gray approximation severely underestimates the MFPs of the phonons that contribute significantly to thermal conductivity because (i) dispersion makes  $v_s$  an overestimate of the average group velocity of acoustic phonons, and (ii) optical phonons contribute to  $C$  but negligibly to bulk  $k$  [97]. Thermal conductivity measurements of thin silicon films indicate that an effective MFP of 300 nm at  $T = 300$  K is more appropriate [24].

To clarify the spectral contributions of phonons to thermal conductivity as a function of MFP, Dames and Chen established the thermal conductivity accumulation function [Eq. (1.5)], which identifies the thermal conductivity due to phonons having MFPs less than  $\Lambda^*$  [38]. To evaluate Eq. (1.5) analytically, models for phonon scattering must be chosen to form expressions for  $C_\Lambda(\Lambda)$  and  $v(\Lambda)$ , examples for which were described in Chapter 1 of this dissertation [44,98]. There is no current consensus on how to select these models, which may be different for different materials. Furthermore, direct calculations of  $k_{\text{accum}}$  at the phonon mode-level by molecular dynamic simulations or lattice dynamics calculations [19,37,45] yield different behaviors for  $k_{\text{accum}}$  than the analytical approaches.

Discrepancies among predictions and a lack of information from conventional thermal conductivity measurements have motivated innovative experimental probing of phonon MFP spectra [19,35,63-65,71]. Koh and Cahill found that the thermal conductivities of InGaP, InGaAs, and SiGe alloys measured by TDTR depend on the surface heat flux modulation frequency  $f_1$  [71]. Koh and Cahill reasoned that phonons with MFPs larger than  $L_p$  travel ballistically and do not contribute to the measured thermal conductivity of the material (i.e., TDTR measures  $k_{\text{accum}}$  where  $\Lambda^* = L_p$ ). Additionally, inquiries to the MFP spectrum have set  $\Lambda^*$  as the heat source dimension through the use of nano-patterned heaters on sapphire [35], the TDTR spot size on c-Si at cryogenic temperatures [19], and the grating period in transient grating experiments [63-65]. Spot size limitations due to the diffraction limit of light and an upper limit to the modulation frequency achievable with pulsed lasers, however, restrict TDTR's ability to probe a broad range of the MFP spectrum. Furthermore, the nano-patterning approach requires an optically transparent sample, while the transient grating observations of nondiffusive transport are as yet limited to thin membranes [63,65]. These experimental limitations motivated the development of BB-FDTR (described in Chapter 2), which allows for fine resolution of an expanded range of  $L_p$ .

In this chapter I describe the preparation and measurement of  $k$  vs.  $L_p$  of different Si-based materials using BB-FDTR. I interpret my results using the reasoning of Koh and Cahill (i.e., that phonons with MFPs larger than  $L_p$  travel ballistically and do not contribute to the measured thermal conductivity of the material) [71]. Under this interpretation,  $k$  vs.  $L_p$  is equivalent to  $k_{\text{accum}}$  vs. MFP. I also show the result of solving the BTE in a system similar to FDTR. As in the experiments, the BTE predicts a heating frequency-dependent thermal conductivity in c-Si at room temperature. This work appears in *Nature Communications*, vol. 4, pp. 1640, 2013 with contributions from co-authors D. P. Sellan, Z. Su, C. H. Amon, A. J. H. McGaughey, and J. A. Malen [73].

## II. Sample preparation

Intrinsic c-Si ( $<1 \times 10^{12} \text{ cm}^{-3}$  impurity atoms), doped c-Si ( $3 \times 10^{19} \text{ cm}^{-3}$  boron atoms), amorphous  $\text{SiO}_2$  (1  $\mu\text{m}$  film thermally grown on c-Si), single crystal platinum, and a-Si (500 nm, 1  $\mu\text{m}$ , and 2  $\mu\text{m}$

films sputtered on c-Si) samples were sputtered with a chromium adhesion layer and a gold transducer. Gold is an ideal transducer because it has high absorption at 488 nm (pump) and a high coefficient of thermoreflectance at 532 nm (probe) [92].

### **A. Transducer layer**

The transducer layer for all samples was prepared by depositing a ~5 nm chromium adhesion layer and ~55 nm of gold using a Perkin Elmer 6J sputtering system. Prior to the sputtering process, the native oxide layers on intrinsic c-Si and doped c-Si samples were removed with a buffered HF solution. The thickness of the transducer layer was measured using XRR. The result of the measurement for intrinsic c-Si is shown in Fig. 3.1. The fit yields values of 8 nm for the chromium adhesion layer and 54 nm for the gold layer, with total thickness  $t_{tr} = 62$  nm. Electron-phonon equilibration length scales are of order 100 nm since the electron-phonon coupling parameter in gold is low. This, combined with an optical extinction length of 20 nm for 488 nm pump light, suggests that the 54 nm gold transducer is isothermal. To include this effect in the analysis its thickness is reduced to 1 nm, its heat capacity is multiplied by 54 so the total heat capacity is invariant, and its thermal conductivity is multiplied by 54 so in-plane heat conduction is not impacted by the reduced thickness. The chromium layer is modeled normally, with no interface resistance between the gold and chromium layers. Modeling thermal transport in the transducer layer will be revisited later in this dissertation. The thermal interface conductance  $G$  for each sample is determined by fitting the 10 highest modulation frequency points of the phase response to minimize the mean square error (MSE). Transducer properties for all samples are shown in Table 3.1.

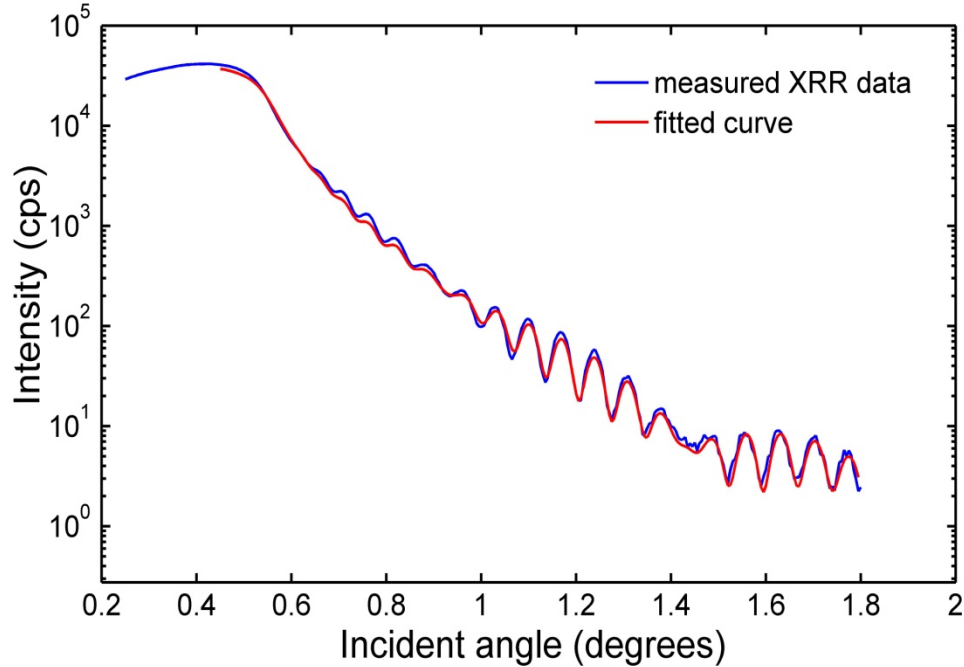


Fig. 3.1. Fitting the measured XRR data yield values of 8 nm and 54 nm for the chromium adhesion layer and the gold layer on c-Si.

## B. Amorphous silicon

The a-Si samples were sputtered on c-Si wafers in a low-pressure, argon-filled chamber. The c-Si wafers were first successively cleaned ultrasonically in acetone, isopropyl alcohol, and deionized water and then submerged in a buffered HF solution to remove the native oxide layer. During the sputtering process, both the target and the wafer were cooled with recycling water. Profilometry was used to measure thicknesses of the a-Si films.

In order to confirm that the a-Si samples are amorphous, low angle x-ray diffraction (XRD) scans were performed on both the a-Si film on the c-Si substrate and the blank c-Si substrate with no film. Conventional theta/2theta scans were completed with a two degree offset to suppress the c-Si substrate peaks and are shown in Fig. 3.2. The scan of the blank c-Si substrate shows a large peak at Si[400] as expected. The scan of the a-Si film shows a broad hump, which is absent in the blank c-Si scan, and a sharp peak at Si[400]. The sharp peak at Si[400] is present from the underlying c-Si substrate because the penetration depth of the x-rays is greater than the a-Si film thickness. The presence of the hump with no additional sharp crystalline peaks, however, is convincing evidence that the a-Si film is amorphous.

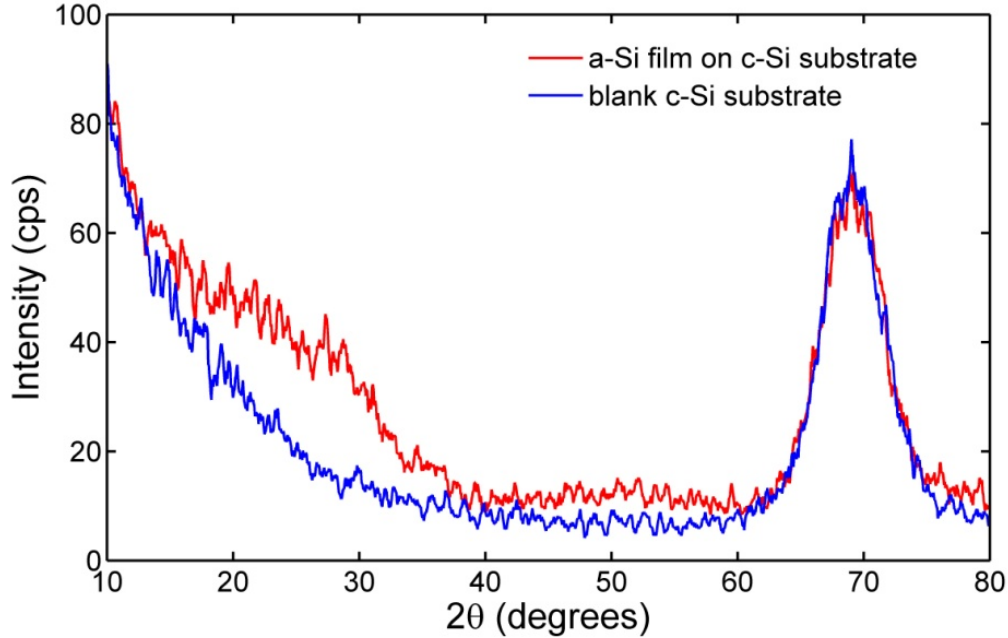


Fig. 3.2. Theta/2theta XRD scans on an a-Si film on a c-Si substrate and a blank c-Si substrate. The broad hump in the a-Si scan verifies the amorphicity of the a-Si film.

### III. Heating frequency dependent thermal conductivity

Phase-lag data from BB-FDTR are fit to the analytical solution of the heat diffusion equation that was described in Chapter 2 [70]. Phase-lag vs. modulation frequency data are shown in Fig. 3.3(a) for intrinsic c-Si ( $T = 311$  K) and SiO<sub>2</sub> at ( $T = 307$  K). Also plotted are the best-fit lines when the entire frequency range is fit to a constant value of thermal conductivity  $k_{\text{constant}}$  (see Table 3.1 for best fits and fitting parameters for all samples considered). For SiO<sub>2</sub>, the constant thermal conductivity fit yields a thermal conductivity of  $1.4 \pm 0.2$  W/m-K, which agrees with bulk values [99] and has a low mean square error (MSE = 0.04). In intrinsic c-Si, however, the constant thermal conductivity fit under-predicts the bulk value (143 W/m-K [95]) as  $99 \pm 6$  W/m-K with a large MSE = 2.4. Consequently, the frequency range is divided into overlapping windows of 13 points, and the thermal conductivity is fit in each section (as described in Chapter 2). When this procedure is done, a frequency-dependent c-Si thermal conductivity is obtained, as shown in Fig. 3.3(b). Window-fitting the phase data for SiO<sub>2</sub>, however, yield a frequency-independent thermal conductivity.

In both cases,  $G$  is assumed to be frequency-independent. This assumption is justified because the relaxation time of electrons in gold is  $3 \times 10^{-14}$  s at  $T = 273$  K [100]. Since the timescale of modulation frequency is minimally five orders of magnitude larger, the electrons and phonons will be in local equilibrium within the transducer over the entire modulation frequency range. Hence, the equilibrium of phonons and electrons at the interface is modulation frequency independent. This assumption is consistent with prior studies [19,71].

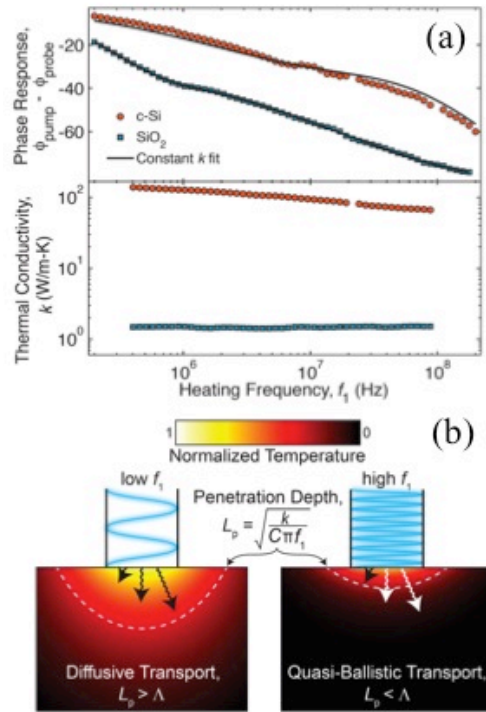


Fig. 3.3. a) Phase-lag vs. modulation frequency data for intrinsic c-Si and SiO<sub>2</sub> shown with a constant thermal conductivity fit over the entire experimental frequency range. Fitting SiO<sub>2</sub> yields a thermal conductivity value of  $1.4 \pm 0.2$  W/m-K, and window fitting produces a heating frequency-independent thermal conductivity. Fitting c-Si over the entire frequency range yields a fitted thermal conductivity below bulk ( $99 \pm 6$  W/m-K) and window fitting shows a modulation frequency-dependent thermal conductivity. b) Illustration of diffusive and ballistic transport. At low heating frequencies, when the thermal penetration depth is greater than the phonon MFPs, there is diffusive thermal transport and a bulk value of thermal conductivity is measured. At high heating frequencies, the thermal penetration depth decreases below the MFPs of some phonons, which travel ballistically through the thermally affected zone (white arrows). These ballistic phonons do not contribute to the measured value of thermal conductivity.

## A. Modeling the diffusive to ballistic transition

To interpret the frequency dependence of the thermal conductivity measurements, the BTE, which simultaneously considers diffusive and ballistic phonon transport, was solved using the lattice Boltzmann method (LBM) [97,101]. The LBM is used to discretize and solve the one-dimensional phonon BTE under the relaxation time approximation and provides the time- and spatial-dependence of phonon occupation numbers. From these phonon occupation numbers, temperature can be calculated using Bose-Einstein statistics. Details of the LBM methodology and numerical recipe are available in Ref. [101].

To use the LBM to solve the BTE for an FDTR-like system, a c-Si film under the gray approximation that is initially set to a uniform temperature of 300 K is considered. The volumetric heat capacity is  $C = 1.66 \text{ MJ/m}^3\text{-K}$ , the speed of sound is  $v_s = 6733 \text{ m/s}$ , and the bulk phonon MFP is  $\Lambda_g = 40 \text{ nm}$ . Similar to the BB-FDTR experiment, a modulated heat flux of amplitude  $q''$  and frequency  $f$  is applied at the free surface ( $z = 0$ ). The heat flux modulation amplitude  $q''$  is chosen such that the maximum surface temperature oscillation amplitude remains below 3 K for all frequencies. The boundary opposite to the heated surface is maintained at  $T = 300 \text{ K}$ . The sample thickness is chosen such that the propagating thermal wave decays to  $T = 300 \text{ K}$  well before it reaches the boundary opposite of the heated surface. It is found that an  $8 \text{ }\mu\text{m}$  sample is sufficiently large for the penetration depths considered. The system is allowed to evolve in time until the steady state temperature oscillation amplitudes and surface temperature oscillation amplitudes are found.

The steady-state temperature oscillation amplitude  $\Delta T$  as a function of sample depth for diffusive and ballistic transport regimes are shown in Fig. 3.4(a),  $\Delta T$  at the surface  $\Delta T_s$  as a function of  $L_p$  is shown in Fig. 3.4(b), and the perceived thermal conductivity based on  $\Delta T_s$  is shown in Fig. 3.4(c). The temperature amplitudes predicted by the Fourier law are plotted for comparison. At low heating frequencies where  $L_p > \text{MFP}$ , the BTE solution matches the Fourier prediction. As frequency increases and  $L_p$  decreases, however, the BTE-predicted  $\Delta T$  becomes larger than that predicted by the Fourier law,

indicating an onset of ballistic phonon transport. In this case, phonons can travel ballistically through the thermally affected zone without scattering, as depicted in Fig. 3.3(b). In the context of the BB-FDTR experiments, the BTE results should be interpreted as an observation of the transition of one phonon mode from diffusive to ballistic transport as the heating frequency is increased. Consistent with the BB-FDTR experiments, the BTE predicts a reduced thermal conductivity compared to bulk as the heating frequency is increased, as shown in Fig. 3.3(c).

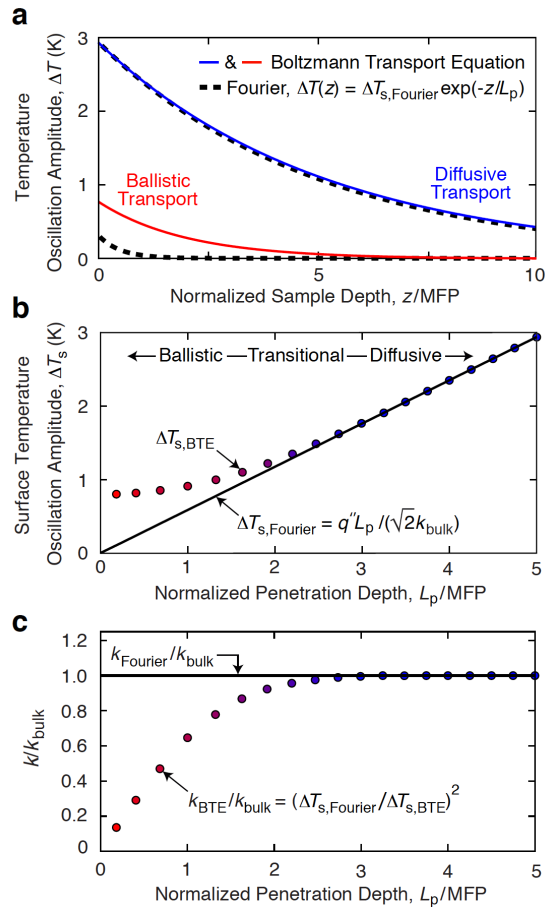


Fig. 3.4. a) Spatial variation of the temperature oscillation amplitude for diffusive transport [corresponding to the lowest heating frequency in (b) and (c)] and ballistic transport [corresponding to the highest heating frequency in (b) and (c)] from the Fourier law (dashed line) and from the lattice Boltzmann method solution to the BTE for a gray material (solid line), all for a periodic surface heat flux. b) Amplitude of the surface temperature oscillation and c) perceived thermal conductivity plotted vs. normalized penetration depth. When  $L_p > \text{MFP}$ , the Fourier and BTE predictions match and BB-FDTR experiments measure a bulk thermal conductivity. When  $L_p < \text{MFP}$ , the Fourier law under-predicts the surface temperature oscillation amplitude, which is perceived as a reduced thermal conductivity, here and in BB-FDTR experiments.

## B. Experimental phonon mean free path spectra

Fitting experimental data (which includes ballistic effects) with a purely diffusive model, results in an effective thermal conductivity. In this study, the interpretation is that this effective thermal conductivity is  $k_{\text{accum}}$  from Eq. (1.5), where only diffusive phonons that have MFP  $< L_p$  contribute (i.e.,  $\Lambda^* = L_p$  is physically imposed). This interpretation is the same as that of Koh and Cahill [71], and consistent with Minnich et al. [19] and Johnson et al. [63,65] who instead used the laser spot diameter and transient grating period as the cutoff dimensions. To generate a phonon MFP spectrum, the measured thermal conductivity at the median frequency of the  $i^{\text{th}}$  fitting window ( $f_{1,i}$ ) is plotted as a function of the corresponding penetration depth,  $L_{p,i} = \sqrt{k_i/C\pi f_{1,i}}$  (see Chapter 2).

Phonon MFP spectra for SiO<sub>2</sub>, intrinsic c-Si, doped c-Si, a-Si (500 nm film), and single crystal platinum near room temperature are compared in Fig. 3.5 (see Table 3.1 for constant thermal conductivity fits and fitting parameters). The thermal conductivities are normalized by their bulk values [95,99,102-104]. Shaded regions indicate uncertainty due to uncertainty in the thickness and thermal conductivity of the gold/chromium transducer, the laser spot size,  $G$ , and the measured phase response (see Chapter 2). For SiO<sub>2</sub> and a-Si, a  $\pm 5\%$  change in film thickness was also considered. In SiO<sub>2</sub>,  $L_{p,i}$  from 60-900 nm yield a constant value of thermal conductivity, which suggests that any phonon-like modes have a MFP spectrum that lies below 60 nm. The thermal conductivity of amorphous materials also has a contribution from non-propagating modes that have been called diffusons [105]. Because these modes do not propagate, there will be no observable transition between diffusive and ballistic transport as the BB-FDTR heating frequency is increased. These frequency-independent data are consistent with measurements of SiO<sub>2</sub> thin films where there was no observed thermal conductivity reduction from bulk due to boundary scattering [99,106]. In platinum, electrons with MFPs  $\sim 10$  nm (Ref. [107]) are the dominant heat carriers and strong electron-phonon coupling ensures that they are in thermal equilibrium with the lattice [108]. Thus, the thermal conductivity of platinum shows no  $L_p$  dependence.

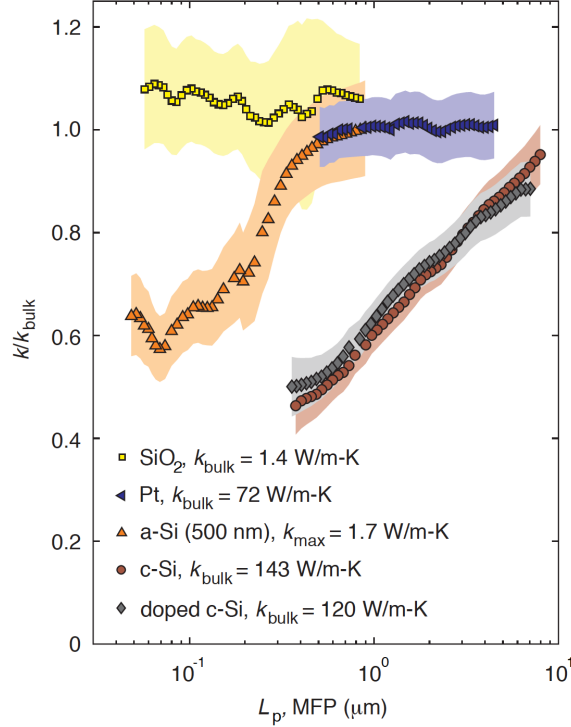


Fig. 3.5. MFP spectra for intrinsic c-Si, doped c-Si, a-Si (500 nm film), amorphous SiO<sub>2</sub>, and platinum near room temperature. The thermal conductivity of SiO<sub>2</sub> is independent of  $L_p$ , suggesting that the MFPs of energy carriers are shorter than 60 nm. The MFP spectrum of platinum is independent of  $L_p$  due to short electron mean free paths ( $\sim 10$  nm) and strong electron-phonon coupling in the metal. The MFP spectrum of intrinsic c-Si and doped c-Si increase with  $L_p$  and show that micron-long MFPs contribute significantly to bulk thermal conductivity at  $T = 300$  K. Doped c-Si has a lower slope compared to intrinsic c-Si because phonons contribute to thermal conductivity with shorter MFPs. The MFP spectrum of the 500 nm a-Si film shows that propagating phonons with MFPs larger than 100 nm contribute  $35 \pm 7\%$  to its thermal conductivity (for a-Si the maximum value is used for normalization).

In intrinsic c-Si  $L_p$  is probed from 0.3–8.0  $\mu\text{m}$  and it is found that phonons with MFPs longer than 1  $\mu\text{m}$  contribute  $40 \pm 5\%$  to the bulk thermal conductivity. It should be noted that  $95 \pm 6\%$  of the bulk thermal conductivity is obtained at the lowest heating frequency (200 kHz,  $L_p \approx 8 \mu\text{m}$ ). This result underscores the importance of using low heating frequencies or steady-state measurements when attempting to measure bulk thermal conductivities. Relative to direct thermal conductivity measurements of c-Si thin films [24] and nanowires [26],  $k_{\text{accum}}$  at the film thickness or wire diameter is lower. In these nanostructures, phonons with MFPs greater than the limiting dimension are not excluded (as they are in BB-FDTR) and contribute to thermal conductivity with a MFP similar to the limiting dimension. Compared to intrinsic c-Si, the MFP spectrum of doped c-Si has a reduced slope, indicating that dopants

broaden the MFP spectrum by adding an additional phonon scattering mechanism. Phonons scattered by dopants are forced to contribute to the thermal conductivity at a shorter MFP than they would in the intrinsic crystal.

The nature of thermal transport in amorphous solids is a long-standing question in solid-state physics [109]. Often, as in the results for SiO<sub>2</sub>, the thermal conductivity can be described in terms of diffusons (i.e., non-propagating modes). In contrast, the MFP spectrum for the 500 nm a-Si film shows that 35±7% of its bulk thermal conductivity comes from propagating (i.e., phonon-like) modes with MFPs longer than 100 nm. Propagating phonon-like modes in a-Si were first inferred by a disagreement between thermal conductivity measurements and modeling predictions that was resolved by the consideration of low-frequency Debye modes [110]. More recent simulations and experiments have also pointed to the existence of long MFP phonon-like modes in a-Si [109,111-113]. Using atomistic calculations, He et al. define modes with MFPs less than 10 nm as diffusons, which contribute approximately half to the bulk thermal conductivity [111]. Phonon-like modes with MFPs greater than 10 nm account for the remaining half. The range of  $L_{p,i}$  (40-1000 nm) in a-Si accesses these phonon-like modes. The spectrum is flat below 100 nm as all of the propagating modes ballistically transmit through the domain while the non-propagating modes remain diffusive. A steep transition occurs from 100-500 nm before the MFP spectrum asymptotes to a constant value as  $L_{p,i}$  exceeds the film thickness (500 nm).

The MFP spectra of 500 nm, 1  $\mu\text{m}$ , and 2  $\mu\text{m}$  thick a-Si films are shown in Fig. 3.6 (see Table 3.1 for constant thermal conductivity fits and fitting parameters). There are two main features, (i) the value measured at low modulation frequencies increases with increasing film thickness, and (ii) as the thickness increases, the location of the abrupt change increases. Regarding (i), some film thickness dependence of thermal conductivity is expected if phonons with MFP longer than the film thickness make significant contributions. Consequently, the value at which the accumulation function plateaus should increase with film thickness since all of the curves are normalized to the same value (1.7 W/m-K). Regarding (ii), in a thin film, the integrand of the accumulation function [from Eq. (1.5)] should display a spike near the film thickness because phonons with MFP greater than the film thickness now contribute with a MFP similar

to the film thickness. This spike in the integrand should translate to a sharp increase in the accumulation function. The location of this sharp increase should increase with increasing film thickness and should happen somewhere near the film thickness. The experimental measurements are consistent with (i) and (ii), and provide evidence that long MFP phonons contribute significantly to thermal transport. Furthermore, the low-frequency values of thermal conductivity observed are consistent with the thickness dependent ranges tabulated by Ref. [111].

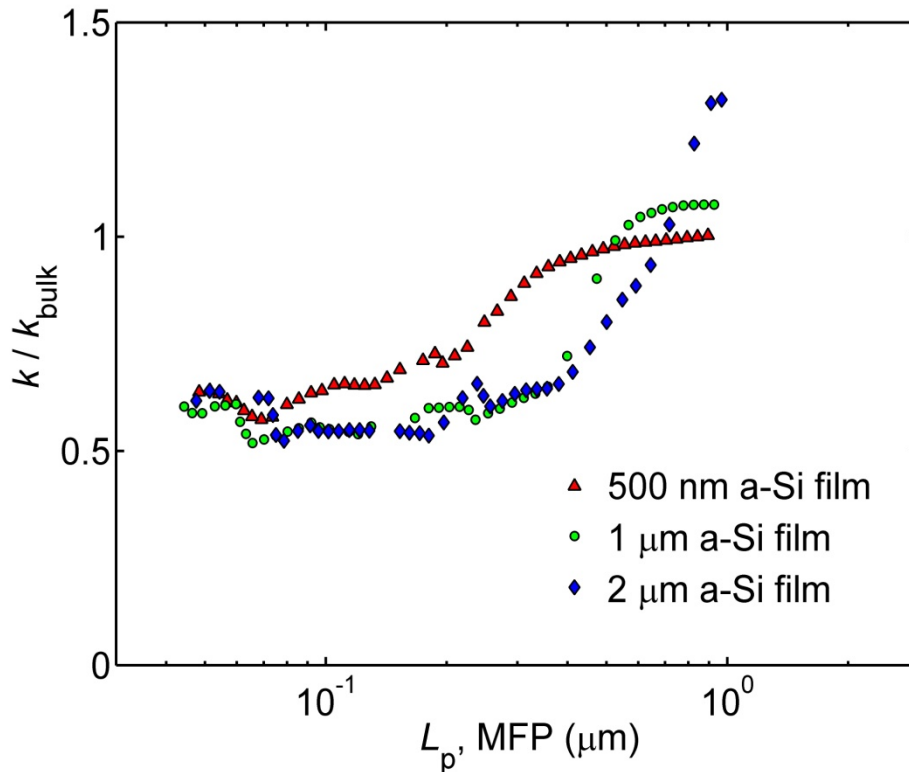


Fig. 3.6. The MFP spectra for 500 nm, 1  $\mu\text{m}$ , and 2  $\mu\text{m}$  thick films of a-Si. All curves are normalized to the maximum value of the 500 nm thick film (1.7 W/m-K). The plateau of the MFP spectra increase with increasing film thickness, suggesting phonons with MFPs larger than the film thickness are contributing significantly to thermal conductivity.

### C. Temperature-dependent MFP spectra in c-Si

For temperature-dependent measurements of c-Si a MicrostatHe cryostat and an ITC503S temperature controller from Oxford Instruments were used. For low temperature measurements liquid  $\text{N}_2$  is used to cool and a resistance heater local to the cold finger is used to stabilize the temperature. Measurements were taken at  $T = 400$  K, 150 K, and 80 K as reported by the temperature controller. The

temperatures reported in this section include the effect from the DC temperature rise (see Chapter 2). Throughout the experiments, the temperature drifted by  $<1$  K.

Phonon MFP spectra of intrinsic c-Si at temperatures of 81, 155, 311, and 417 K are shown in Fig. 3.7 normalized by bulk values [95,104] (see Table 3.1 for constant thermal conductivity fits and fitting parameters). The associated values of  $G$ , shown in the inset, are consistent with prior measurements of a chromium/silicon interface [114]. At lower temperatures, longer MFP phonons contribute more significantly to the measured thermal conductivity. At temperatures of 81 K and 155 K, the heat capacity is at 20% and 45% of saturation [115]. High frequency phonon modes are not populated and phonon-phonon scattering is reduced relative to  $T = 311$  K. At temperatures of 311 and 417 K, the population effects are less critical because the heat capacity is at 75% and 83% of saturation [115]. Instead, the shift in the MFP spectrum from  $T = 311$  K to  $T = 417$  K comes primarily from increased phonon-phonon scattering (i.e., increased anharmonicity).

While these data compare favorably with the first principles predictions by Esfarjani and coworkers [19,45,116] at all temperatures, one unresolved discrepancy is that a frequency-dependent thermal conductivity was not observed in TDTR measurements of c-Si at  $T = 300$  K [71]. Plausible explanations include (i) that a narrower frequency range (0.5-10 MHz compared to our range of 0.2-200 MHz) was considered, (ii) that the transducer material may affect the perceived frequency dependence (TDTR uses Al, while BB-FDTR uses Au), and (iii) that the radii of the laser beams, known to influence TDTR measurements of thermal conductivity at cryogenic temperatures [19], was different (6.5-15  $\mu\text{m}$  for TDTR relative to 3.4  $\mu\text{m}$  for BB-FDTR). The reasons for this discrepancy will be discussed further in the following chapters.

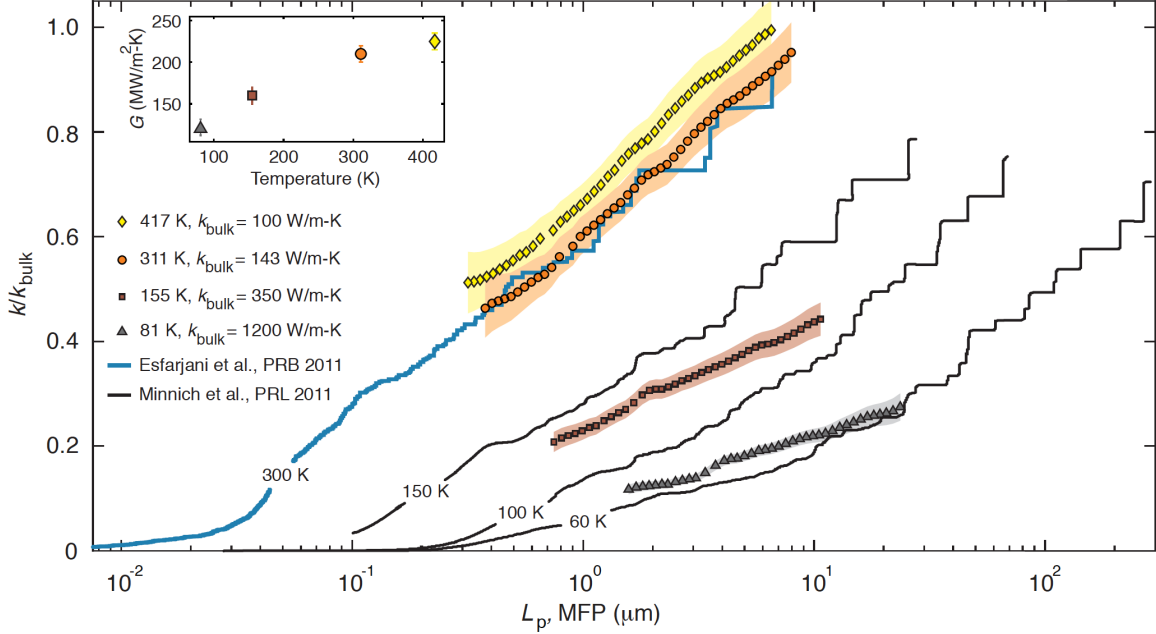
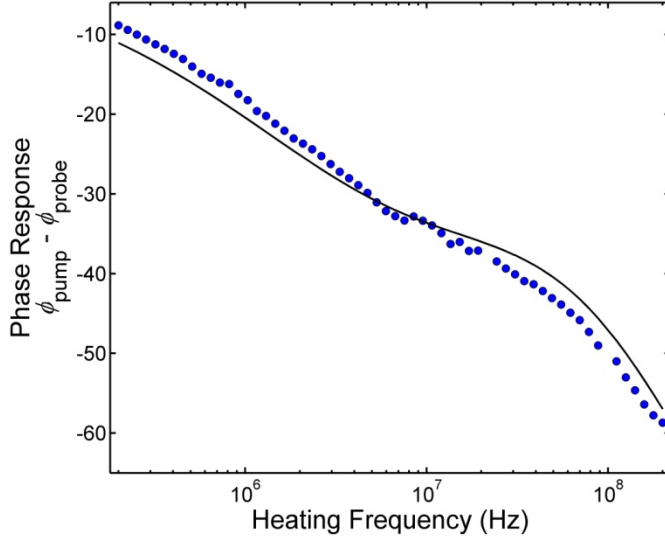


Fig. 3.7. MFP spectra for intrinsic c-Si at  $T = 81, 155, 311,$  and  $417$  K compared to MFP predictions from first principles calculations. Inset shows the temperature dependence of thermal interface conductance between the gold/chromium transducer and the intrinsic c-Si sample. The spectrum of phonon MFPs relevant to thermal conductivity shifts to lower values with increasing temperature due to increased phonon-phonon scattering. At  $T = 300$  K, phonons with  $MFP > 1 \mu\text{m}$  contribute  $40 \pm 5\%$  to bulk thermal conductivity. Comparison with predictions from Minnich et al. (Ref. [19]) and Esfarjani et al. (Ref. [45]) are favorable at all temperatures.

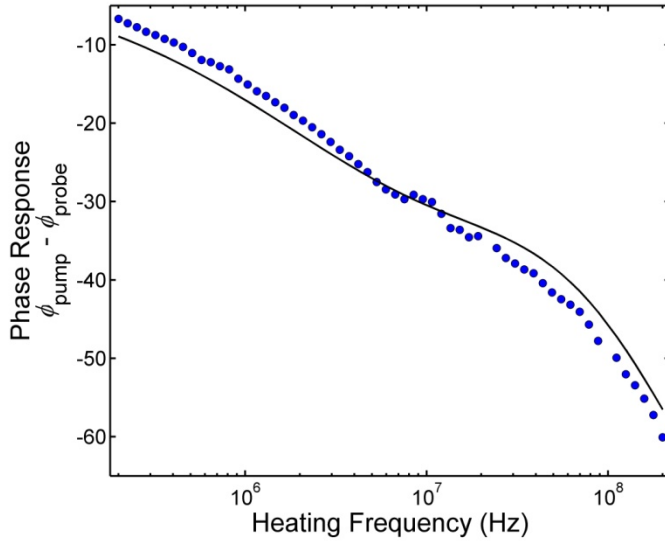
#### IV. Summary

This discovery that micron-long MFPs contribute substantially to  $k$  at room temperature and above suggests that silicon-based devices may have thermal management challenges in structures much larger than traditionally expected [24,37]. BB-FDTR's continuous resolution of the MFP spectrum indicates how the dissipative ability of c-Si will continuously decrease as transistor size decreases to uphold Moore's Law. Likewise, BB-FDTR can aid in the understanding of thermal transport in amorphous solids by identifying propagating phonon modes and generating thermal conductivity accumulation functions. The general experimental approach can be extended to measure the phonon MFP spectrum of other semiconducting and insulating solids [75].

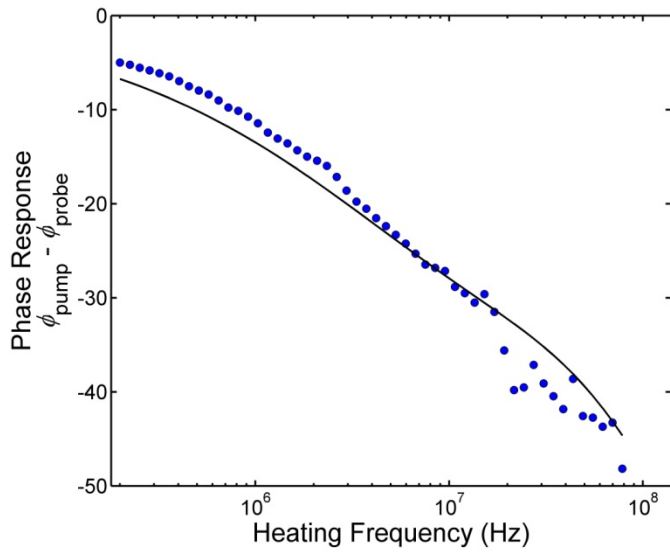
Table 3.1. Phase lag data from BB-FDTR experiments shown with constant  $k$  fits, and the parameters used in the fits for each sample.



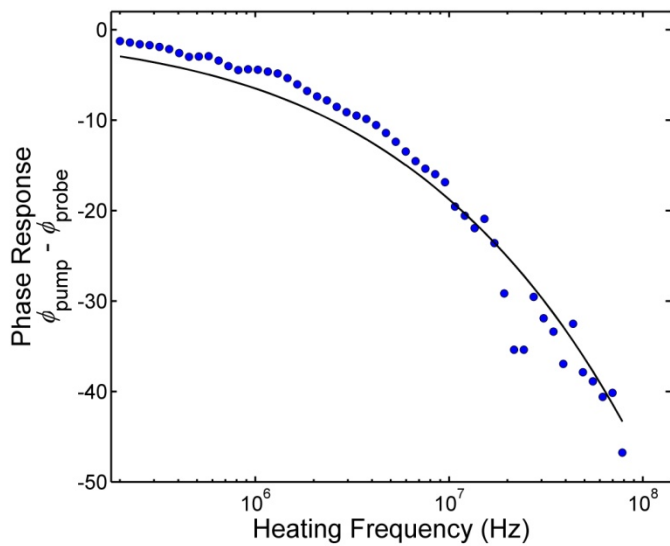
Sample: c-Si, $T = 416.6$ K	
$C_v$ [115] (kJ/m <sup>3</sup> -K)	1840
$k_{tr}$ , (W/m-K)	110
$t_{tr}$ , (nm)	62
$t_{sub}$ , (nm)	$5.25 \times 10^5$
$G$ , (MW/m <sup>2</sup> -K)	225
$k_{constant}$ , (W/m-K)	73.1
$A_o$ (mW)	20
DC $\Delta T$ , (K)	16.6
$k_{bulk}$ [95,104] (W/m-K)	100



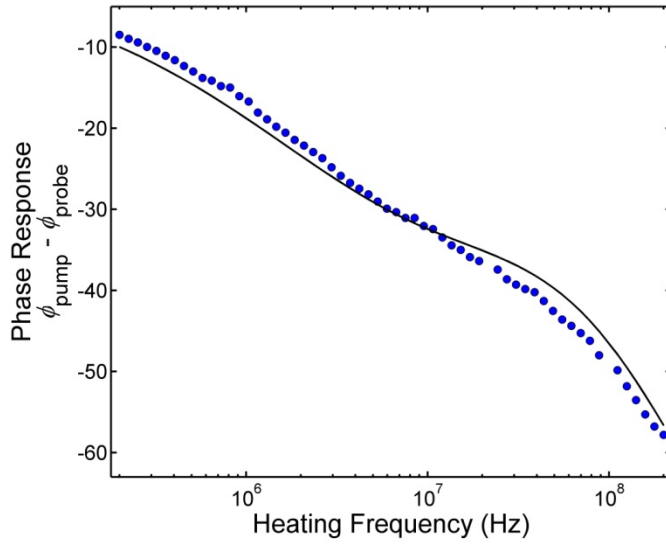
Sample: c-Si, $T = 311.4$ K	
$C_v$ [115] (kJ/m <sup>3</sup> -K)	1692
$k_{tr}$ , (W/m-K)	110
$t_{tr}$ , (nm)	62
$t_{sub}$ , (nm)	$5.25 \times 10^5$
$G$ , (MW/m <sup>2</sup> -K)	210
$k_{constant}$ , (W/m-K)	99.1
$A_o$ (mW)	20
DC $\Delta T$ , (K)	11.4
$k_{bulk}$ [95,104] (W/m-K)	143



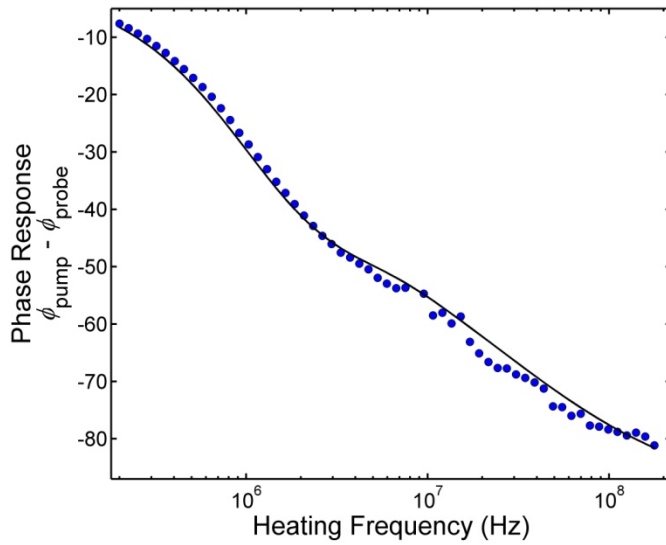
Sample: c-Si, $T = 154.7$ K	
$C_v$ [115] (kJ/m <sup>3</sup> -K)	1061
$k_{tr}$ , (W/m-K)	110
$t_{tr}$ , (nm)	62
$t_{sub}$ , (nm)	$5.25 \times 10^5$
$G$ , (MW/m <sup>2</sup> -K)	160
$k_{constant}$ , (W/m-K)	107.7
$A_o$ (mW)	20
DC $\Delta T$ , (K)	4.7
$k_{bulk}$ [95] (W/m-K)	350



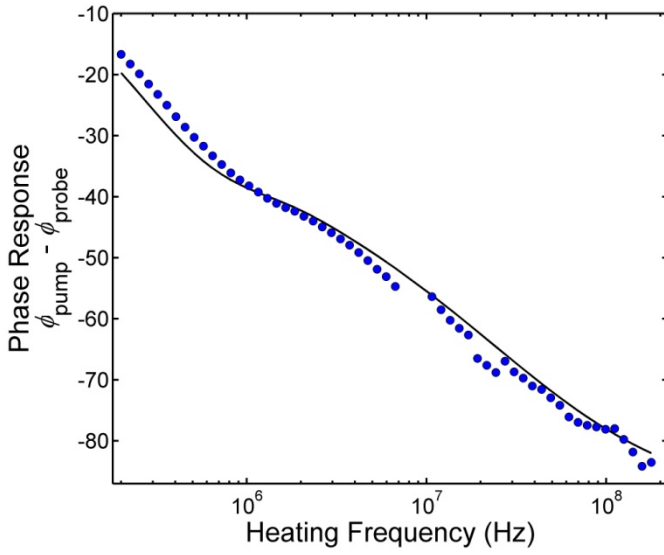
Sample: c-Si, $T = 81.3$ K	
$C_v$ [115] (kJ/m <sup>3</sup> -K)	466
$k_{tr}$ , (W/m-K)	110
$t_{tr}$ , (nm)	62
$t_{sub}$ , (nm)	$5.25 \times 10^5$
$G$ , (MW/m <sup>2</sup> -K)	120
$k_{constant}$ , (W/m-K)	187.1
$A_o$ (mW)	19
DC $\Delta T$ , (K)	1.3
$k_{bulk}$ [95] (W/m-K)	1200



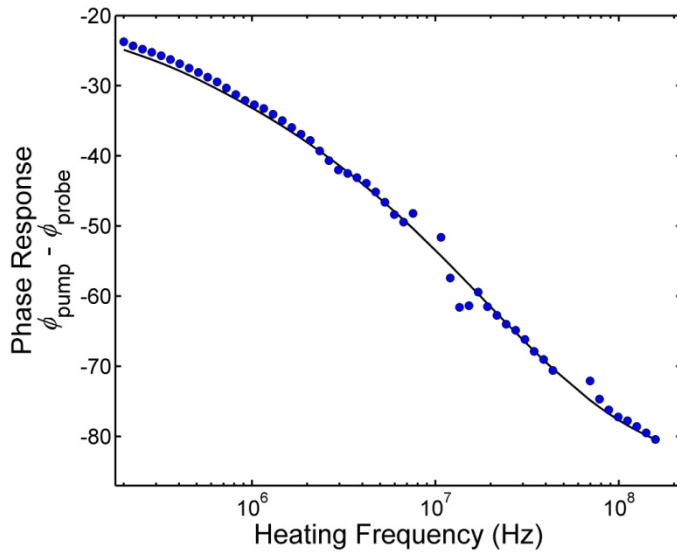
Sample: doped c-Si, $T = 313.8$ K	
$C_v$ [115] (kJ/m <sup>3</sup> -K)	1692
$k_{tr}$ , (W/m-K)	112
$t_{tr}$ , (nm)	61
$t_{sub}$ , (nm)	$3.8 \times 10^5$
$G$ , (MW/m <sup>2</sup> -K)	220
$k_{constant}$ , (W/m-K)	82.6
$A_o$ (mW)	20
DC $\Delta T$ , (K)	13.8
$k_{bulk}$ [102] (W/m-K)	120



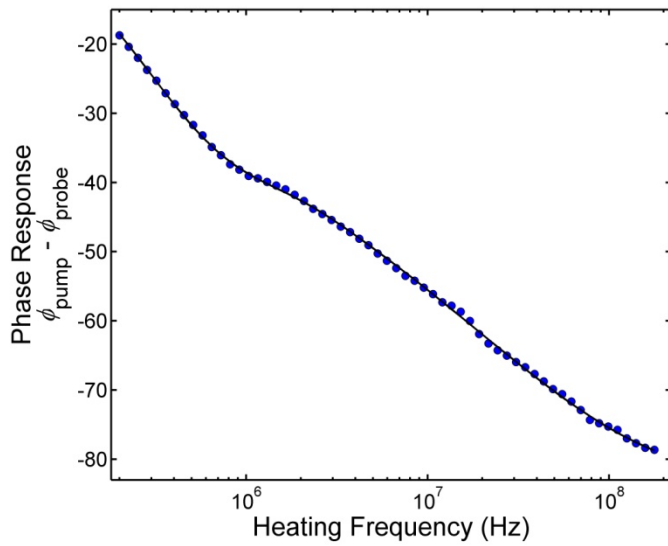
Sample: 500 nm a-Si, $T = 305.5$ K	
$C_v$ [115] (kJ/m <sup>3</sup> -K)	1677
$k_{tr}$ , (W/m-K)	117
$t_{tr}$ , (nm)	60
$t_{sub}$ , (nm)	500
$G$ , (MW/m <sup>2</sup> -K)	40
$k_{constant}$ , (W/m-K)	1.49
$A_o$ (mW)	9.5
DC $\Delta T$ , (K)	5.5
$k_{bulk}$ , (W/m-K)	n/a



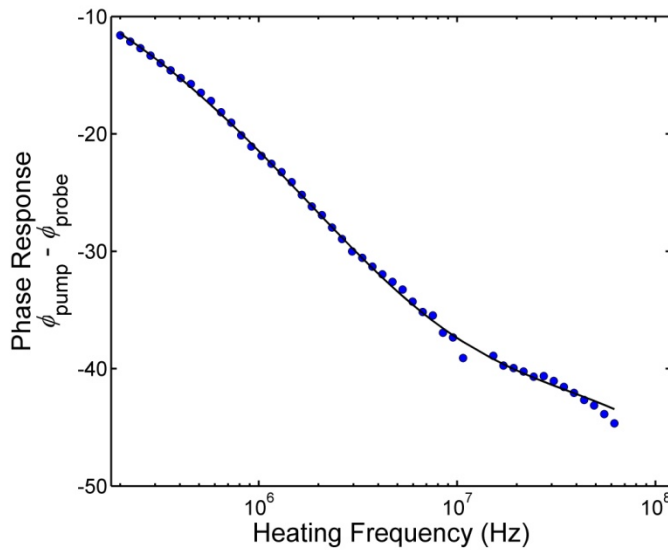
Sample: 1 $\mu\text{m}$ a-Si, $T = 306.3$ K	
$C_v$ [115] (kJ/m <sup>3</sup> -K)	1677
$k_{tr}$ , (W/m-K)	115
$t_{tr}$ , (nm)	58
$t_{sub}$ , (nm)	1000
$G$ , (MW/m <sup>2</sup> -K)	35
$k_{constant}$ , (W/m-K)	1.35
$A_o$ (mW)	11
DC $\Delta T$ , (K)	6.3
$k_{bulk}$ , (W/m-K)	n/a



Sample: 2 $\mu\text{m}$ a-Si, $T = 304.6$ K	
$C_v$ [115] (kJ/m <sup>3</sup> -K)	1677
$k_{tr}$ , (W/m-K)	130
$t_{tr}$ , (nm)	61
$t_{sub}$ , (nm)	2200
$G$ , (MW/m <sup>2</sup> -K)	30
$k_{constant}$ , (W/m-K)	1.0
$A_o$ (mW)	6.1
DC $\Delta T$ , (K)	4.6
$k_{bulk}$ , (W/m-K)	n/a



Sample: SiO <sub>2</sub> , $T = 306.6$ K	
$C_v$ [103] (kJ/m <sup>3</sup> -K)	1677
$k_{tr}$ , (W/m-K)	130
$t_{tr}$ , (nm)	61
$t_{sub}$ , (nm)	1000
$G$ , (MW/m <sup>2</sup> -K)	60
$k_{constant}$ , (W/m-K)	1.48
$A_o$ (mW)	11.5
DC $\Delta T$ , (K)	6.6
$k_{bulk}$ [103] (W/m-K)	1.4



Sample: Pt, $T = 318.8$ K	
$C_v$ [103] (kJ/m <sup>3</sup> -K)	2848
$k_{tr}$ , (W/m-K)	118
$t_{tr}$ , (nm)	62
$t_{sub}$ , (nm)	$1 \times 10^6$
$G$ , (MW/m <sup>2</sup> -K)	850
$k_{constant}$ , (W/m-K)	71.9
$A_o$ (mW)	12.5
DC $\Delta T$ , (K)	18.8
$k_{bulk}$ [103] (W/m-K)	72

## 4. INTERPRETING NONDIFFUSIVE BB-FDTR MEASUREMENTS WITH THE BTE

### I. Overview

The thermal conductivity accumulation function is important for determining the relationship between system dimensions and effective thermal conductivity. Attempts to experimentally measure  $k_{\text{accum}}$  induce nondiffusive thermal transport through varying an experimentally controllable length scale  $L_c$  in a range comparable to phonon MFPs. Nondiffusive thermal transport has been observed in TTG [65] and TDTR and BB-FDTR [19,71,73-75] experiments. An effective thermal conductivity of the material as a function of  $L_c$  is found by interpreting these nondiffusive measurements with a solution to the heat diffusion equation.

The initial interpretation to obtain  $k_{\text{accum}}$  from  $k$  vs.  $L_c$  measurements was that energy carriers with  $\Lambda > L_c$  do not contribute to the experimentally measured thermal conductivity  $k_{\text{exp}}$  and energy carriers with  $\Lambda \leq L_c$  fully contribute, as they would in a purely diffusive regime [19,71,73,75]. Determining  $k_{\text{accum}}$  for Si-based materials using BB-FDTR under this interpretation was described in Chapter 3. Mathematically, this assumption takes the form

$$k_{\text{exp}}(L_c) = \int_0^{L_c} k_{\Lambda} d\Lambda \quad . \quad (4.1)$$

This mapping between  $L_c$  and MFP contributions to the effective thermal conductivity leads to accumulation functions that are consistent with first principles predictions in silicon and gallium arsenide [19,73,75], but lacks rigorous justification. More generally,

$$k_{\text{exp}}(L_c) = \int_0^{\infty} S(\Lambda, L_c) k_{\Lambda} d\Lambda \quad , \quad (4.2)$$

where  $S(\Lambda, L_c)$  is known as the suppression function. In the simple interpretation in Eq. (4.1),  $S(\Lambda, L_c)$  is a step function from 1 to 0 at  $\Lambda = L_c$ . But discrepancies between BB-FDTR [73] and TDTR [71] results using Eq. (4.1) demand a deeper understanding of the suppression function.

Comparison of analytical [81] and numerical solutions [79,80,82] of the BTE to the heat diffusion equation for TTG leads to the functional dependence of the suppression function on  $L_c$  and MFP and reconciles nondiffusive TTG measurements and  $k_{\text{accum}}$ . In this chapter, I derive an analytical suppression function for thermoreflectance techniques by solving the BTE. In thermoreflectance techniques, there are two experimental length scales: (1) the thermal penetration depth  $L_p$  and (2) the  $e^{-2}$  radius of the Gaussian laser spot,  $r_o$ . The presence of  $r_o$  in thermoreflectance experiments necessitates a comparison of length scales rather than the time scales  $1/\Omega$  and phonon lifetime. I account for both experimental length scales in my expression for the suppression function. I use the results to interpret nondiffusive measurements of phonon transport in silicon by BB-FDTR and TDTR, although the solution does not account for the multiple time scales in TDTR that arise from using a pulsed laser. Before this work was published, Ding *et al.* predicted suppression due to spot size in TDTR using a Monte Carlo-based numerical solution to the BTE [72], but neither suppression due to thermal penetration depth nor analytical analyses for these experiments had been demonstrated in the literature. Three important questions are clarified: (1) What is the form of thermal penetration depth-based suppression? (2) What is its interplay with spot size-based suppression? (3) Under what circumstances can BB-FDTR and TDTR measurements be interpreted with the conventional heat diffusion equation? This work appears in *Physical Review B*, vol. 90, pp. 064302, 2014 with contributions from co-authors A. J. H. McGaughey and J. A. Malen [83].

## II. Suppression function in a planar geometry

As shown in Fig. 4.1(a), a planar medium with a temporally oscillating surface temperature with angular frequency  $\Omega$  and amplitude  $T_s = 1$  K, such that  $T(x = 0, t) = T_s e^{i\Omega t}$  is considered first. Because I solve for deviations from the mean temperature, for convenience I define the temperature  $T(x \rightarrow \infty, t) = T_\infty = 0$  K. The one-dimensional nature of this problem will yield an analytical solution that provides insight into the functional dependence of the suppression function on thermal penetration depth.

I begin with the gray, 1-D BTE for phonons in Cartesian coordinates under the relaxation time approximation in an isotropic medium [39,117]

$$\frac{1}{v} \frac{\partial n}{\partial t} + \mu \frac{\partial n}{\partial x} = \frac{n_e - n}{\tau v} , \quad (4.3)$$

where the non-equilibrium distribution function  $n(x, t, \mu)$  is the phonon energy density per unit phonon frequency per unit solid angle and equals  $\hbar\omega D(\omega)g(x, t, \mu)/4\pi$ . Here,  $\hbar$  is the reduced Planck constant,  $\omega$  is phonon frequency,  $D(\omega)$  is the phonon density of states,  $g(x, t, \mu)$  is the occupation function,  $n_e(x, t)$  is the equilibrium distribution function and is specified for phonons when  $g$  is the Bose-Einstein distribution  $g_{BE}$ ,  $\tau$  is the phonon lifetime  $\Lambda/v$ ,  $v$  is the frequency-independent phonon group velocity (i.e., sound velocity), and  $\mu$  is the directional cosine ( $\mu = \cos\theta$ ) that accounts for the velocity of phonons traveling at an angle  $\theta$  from the  $x$ -direction [see Fig. 4.1(a)]. For small temperature variation,  $n_e(x, t) \approx \hbar\omega D(\omega) \left. \frac{dg_{BE}}{dT} \right|_{x,t} T(x, t)/4\pi = C_\omega T(x, t)/4\pi$ , where  $C_\omega$  is the volumetric heat capacity per unit frequency and  $T(x, t)$  is the departure from  $T_\infty = 0$  [50,79,81,84]. Thus, I solve for the deviations from the equilibrium distribution function, which are related to deviations of temperature from  $T_\infty$ .

Since the oscillating surface temperature determines the temporal behavior of the solution, separation of variables is performed such that  $n(x, t, \mu) = \bar{n}(x, \mu)e^{i\Omega t}$ , where  $\bar{n}$  is the component of  $n$  that is only a function of  $x$  and  $\mu$ . Substituting into Eq. (4.3) yields

$$\mu \frac{d\bar{n}}{dx} + \left( \frac{i\Omega}{v} + \frac{1}{\tau v} \right) \bar{n} = \frac{\bar{n}_e}{\tau v} . \quad (4.4)$$

The difficulty in solving Eq. (4.4) arises from the fact that phonons traveling over all directions  $\mu$  must be accounted for. For TTG, Collins *et al.* demonstrated a Volterra integral solution to a BTE of similar form [81], but the dependence on  $\mu$  in this formulation leads to a divergent integral. Henceforth, a two-flux procedure, similar to that of the Milne-Eddington approximation for radiative heat transfer [118], is followed. This method involves taking the zeroth and first moments of Eq. (4.4) [i.e., Eq. (4.4) is integrated over all directions after multiplication with  $\mu^0 = 1$  (zeroth moment) and  $\mu^1 = \mu$  (first moment)]. The distribution moments are defined as

$$\bar{n}_l(x) = 2\pi \int_{-1}^1 \bar{n}(x, \mu) \mu^l d\mu, \quad l = 0, 1, \dots . \quad (4.5)$$

Furthermore, the distribution function is assumed to be isotropic over the upper and lower hemispheres such that  $\bar{n}^+(x) \equiv \bar{n}(x, 0 < \mu \leq 1)$  and  $\bar{n}^-(x) \equiv \bar{n}(x, -1 \leq \mu \leq 0)$  [see Fig. 4.1(a)] [118]. From Eq. (4.5), the zeroth and first moments are  $\bar{n}_0 = 2\pi(\bar{n}^+ + \bar{n}^-) = 3\bar{n}_2$  and  $\bar{n}_1 = \pi(\bar{n}^+ - \bar{n}^-)$ , which can be physically related to temperature and heat flux [118]. Applying the two flux method to Eq. (4.4) yields a coupled set of equations

$$\frac{d\bar{n}_0}{dx} + 3\left(\frac{i\Omega}{v} + \frac{1}{\tau v}\right)\bar{n}_1 = 0 \quad , \quad (4.6a)$$

$$\frac{d\bar{n}_1}{dx} + \frac{i\Omega}{v}\bar{n}_0 = 0 \quad . \quad (4.6b)$$

In formulating Eqs. (4.6a) and (4.6b), conservation of energy for a gray medium is used to determine the equilibrium distribution  $\bar{n}_e$  in terms of  $\bar{n}_0$  (Ref. [21]) as

$$\bar{n}_e = \frac{1}{2} \int_{-1}^1 \bar{n} d\mu = \frac{\bar{n}_0}{4\pi} \quad . \quad (4.7)$$

This coupled set of ordinary, linear, homogeneous differential equations is an eigenvalue problem and has a solution of the form  $\begin{bmatrix} \bar{n}_0 \\ \bar{n}_1 \end{bmatrix} = c_1 \mathbf{v}_1 e^{-\lambda x} + c_2 \mathbf{v}_2 e^{\lambda x}$ , where  $c_1$  and  $c_2$  are constants to be determined by the boundary conditions,  $\pm\lambda$  are the eigenvalues, and  $\mathbf{v}_1$  and  $\mathbf{v}_2$  are the eigenvectors. Since the spatial domain is semi-infinite,  $c_2 = 0$  because  $\bar{n}_0$  and  $\bar{n}_1$  cannot increase unbounded. The boundary condition at  $x = 0$  is depicted schematically in Fig. 4.1(a) and is [17,119]

$$\bar{n}^+(x = 0) = \varepsilon \frac{C_{\omega T_s}}{4\pi} + \rho \bar{n}^-(x = 0) \quad , \quad (4.8)$$

where  $\varepsilon$  and  $\rho$  are the phonon emissivity and reflectivity, both of which will be discussed in further detail later in this chapter. Physically, Eq. (4.8) states that the total energy carried by phonons traveling in the positive  $x$ -direction at the surface is equal to the sum of the energy carried by phonons emitted due to the induced surface temperature  $T_s$  and the energy carried by phonons travelling in the negative  $x$ -direction that are reflected from the surface.

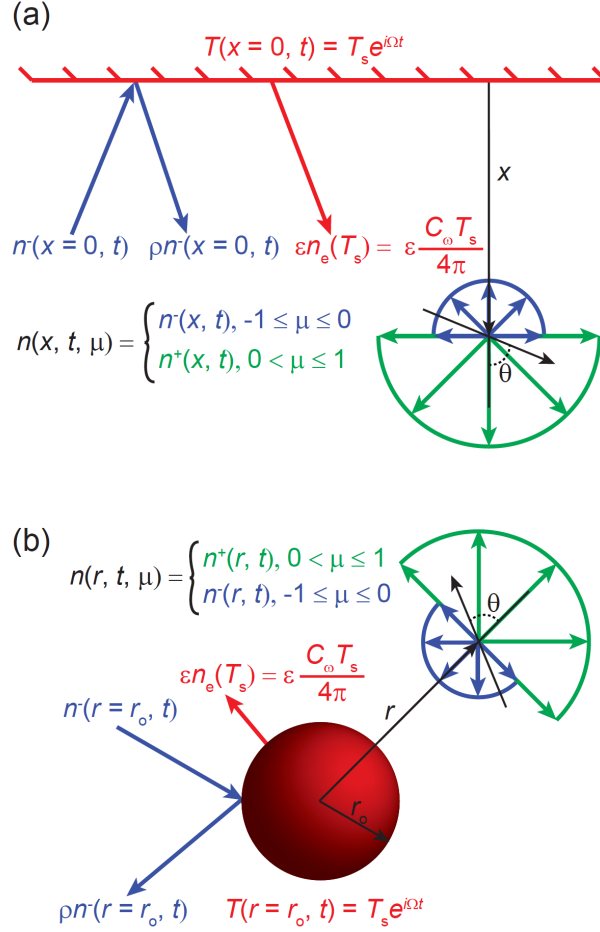


Fig. 4.1. Schematic diagrams for (a) the 1-D planar system and (b) the spherically symmetrical system, both with oscillating surface temperatures. Here,  $\mu$  is the directional cosine,  $\mu = \cos\theta$ . The parameters  $\epsilon$  and  $\rho$  are the phonon emissivity and reflectivity.

By solving the system of equations and integrating over all phonon frequencies, the spatial temperature and heat flux profiles are found to be

$$\bar{T}_{\text{BTE}}(x) = \frac{\int_0^\infty \bar{n}_0(x) d\omega}{\int_0^\infty C_\omega d\omega} = \frac{\epsilon T_s}{(1+\rho) \frac{4i\beta}{3\eta} + (1-\rho)} \exp\left(-\frac{\eta}{L_p} x\right), \quad (4.9a)$$

$$\bar{q}''_{\text{BTE}}(x) = \int_0^\infty v \bar{n}_1(x) d\omega = \frac{\epsilon T_s C v}{2(1+\rho) + (1-\rho) \frac{3\eta}{2i\beta}} \exp\left(-\frac{\eta}{L_p} x\right), \quad (4.9b)$$

where  $\eta = \sqrt{2i - 2\tau\Omega}$ ,  $\beta = \Lambda/L_p$ , and  $k_{\text{bulk}} = \frac{1}{3} C v^2 \tau$ . Since the gray approximation is used,  $\bar{n}_0$  and  $\bar{n}_1$  are independent of  $\omega$  and the integral over  $\omega$  only changes  $C_\omega$  to the total volumetric heat capacity, i.e.,

$\int_0^\infty C_\omega d\omega = C$ . To generate figures in this section and the following section, bulk silicon properties ( $C = 1.65 \times 10^6 \text{ J m}^{-3} \text{ K}^{-1}$ ,  $k_{\text{bulk}} = 145 \text{ W m}^{-1} \text{ K}^{-1}$ , and  $v = 8430 \text{ m s}^{-1}$ ) [42,120] are used and  $L_p$  is determined using  $k_{\text{bulk}}$ .

The magnitudes of the spatial temperature profiles from the diffusion solution [ $\bar{T}_{\text{diff}}(x) = T_s \exp(-\frac{\sqrt{2i}x}{L_p})$ ] and BTE solution for  $\varepsilon = 1 - \rho = 1$  and  $\Lambda/L_p = 1$  are shown in Fig. 4.2(a). The spatial temperature profile from the diffusion solution is a continuous exponential decay where the diffusive thermal resistance can be defined as  $R_{\text{diff},x} = (T_s - T_\infty)/\bar{q}_{\text{diff}}''(x=0)$ . The real part of the exponential in Eqs. (4.9a) and (4.9b) represents the BTE prediction of penetration depth  $L_{p\text{-BTE}}$ , which can be written as

$$L_{p\text{-BTE}} = \frac{L_p}{\sqrt{(1+\tau^2\Omega^2)^{1/2}-\tau\Omega}} \quad (4.10)$$

When  $\tau\Omega \ll 1$ ,  $L_{p\text{-BTE}} = L_p$  and  $\bar{T}_{\text{BTE}}(x)$  collapses to  $\bar{T}_{\text{diff}}(x)$ , but when  $\tau\Omega \gg 1$ ,  $L_{p\text{-BTE}} \rightarrow \infty$ , which indicates purely ballistic transport. Thus, as  $\Lambda/L_p$  increases, the temperature decay rate predicted by the BTE decreases.

The spatial temperature profile from the BTE solution indicates two distinct regions: a surface temperature jump of  $\Delta T_\varepsilon$  and a spatial temperature decay spanning  $\Delta T_i$ . When  $\varepsilon = 1 - \rho$ , the total thermal resistance from the BTE solution  $R_{\text{BTE},x}$  is comprised of two parts,

$$R_\varepsilon = \frac{\Delta T_\varepsilon}{\bar{q}_{\text{BTE}}''(x=0)} = \frac{4 - 2\varepsilon}{\varepsilon C v} \quad (4.11a)$$

$$R_{i,x} = \frac{\Delta T_i}{\bar{q}_{\text{BTE}}''(x=0)} = \frac{\sqrt{\frac{L_p^2}{2i} + \frac{\Lambda^2}{3}}}{k_{\text{bulk}}} \quad (4.11b)$$

such that

$$R_{\text{BTE},x} = R_\varepsilon + R_{i,x} \quad (4.11c)$$

The thermal resistances in Eqs. (4.11a), (4.11b), and (4.11c) are complex. Complex thermal resistances are analogous to impedance in alternating current circuit analysis. In the plots throughout this chapter, the magnitude of such complex thermal resistances is plotted.

The magnitude of the terms  $R_\varepsilon$ ,  $R_{i,x}$ , and  $R_{\text{BTE},x}$  are plotted in Fig. 4.2(b) as a function of  $\Lambda/L_p$  and  $\tau\Omega$  with  $\varepsilon = 1 - \rho = 1$  and are compared to the magnitude of  $R_{\text{diff},x}$ . The term  $R_\varepsilon$  is a resistance that arises from the interaction between the surface and ballistic phonons originating within one MFP of the surface and is associated with the surface temperature jump in BTE [17,20,97,121] and radiative transfer [122] problems. The term  $R_\varepsilon$  is independent of any experimentally controllable length scale but is always present. The term  $R_{i,x}$  is intrinsic to the material and accounts for transport of phonons associated with two length scales:  $L_p$  and  $\Lambda$ . It should be noted that  $R_{i,x}$  says nothing about the surface properties (i.e.,  $R_{i,x}$  is not a function of  $\varepsilon$ ). Thus, when  $\Lambda/L_p \ll 1$ ,  $R_{\text{BTE},x} = R_\varepsilon + R_{i,x} = R_\varepsilon + L_p/(\sqrt{2}ik_{\text{bulk}}) \approx L_p/(\sqrt{2}ik_{\text{bulk}})$  and the BTE thermal resistance converges to the diffusive thermal resistance because  $R_{i,x}$  dominates  $R_\varepsilon$ . However, as the phonon MFP approaches  $L_p$ , the second term in  $R_{i,x}$  and the  $R_\varepsilon$  term become non-negligible and the BTE thermal resistance becomes larger than the diffusive thermal resistance. In the ballistic limit ( $\Lambda/L_p \gg 1$ ),  $R_{\text{BTE},x} = R_\varepsilon + R_{i,x} = R_\varepsilon + \Lambda/(\sqrt{3}k_{\text{bulk}})$  and becomes independent of  $\Omega$ . It should be noted that the total thermal resistance is independent of whether a temporally oscillating surface temperature or heat flux is imposed, the latter of which is more consistent with the experiments.

As in the analysis of the experimental measurements, the effective thermal conductivity  $k_{\text{eff}}$  is determined by equating the complex diffusive thermal resistance ( $R_{\text{diff},x} = 1/\sqrt{i\Omega Ck_{\text{eff}}}$ ) to the complex thermal resistance determined by the BTE,  $R_{\text{BTE},x}$  [17,80]. Since, by definition,  $T_s$  is identical in both systems, this procedure is equivalent to equating surface heat fluxes from the diffusion and BTE solutions. Furthermore, identical functional forms of the BTE and diffusion solutions suggest that interpreting nondiffusive transport with an effective, suppressed  $k$  is reasonable. The suppression function for this planar geometry  $S_x(\Lambda, L_p, \varepsilon, \rho)$  is the fractional contribution to thermal conductivity made by a phonon with a MFP of  $\Lambda$  in a thermorefectance experiment with  $\Omega$ ,  $\varepsilon$ , and  $\rho$  and is

$$S_x(\Lambda, L_p, \varepsilon, \rho) = \frac{k_{\text{eff}}}{k_{\text{bulk}}} = \frac{9\varepsilon^2}{2i\beta^2 \left[ 2(1+\rho) + (1-\rho)\frac{3\eta}{2i\beta} \right]^2} . \quad (4.12)$$

It should be noted that  $S_x(\Lambda, L_p, \varepsilon, \rho)$  is complex. Thus the phase angle of the suppression function influences the observed phase angle in thermoreflectance experiments, ultimately influencing the value of thermal conductivity obtained. In plots of the suppression function throughout the paper, its magnitude is plotted.

The magnitude of the thermal resistance of the system from the BTE and diffusion solutions and the magnitude of  $S_x(\Lambda, L_p, \varepsilon, \rho)$  as a function of  $\Lambda/L_p$  and  $\tau\Omega$  for  $\varepsilon = 1 - \rho = 1, 0.5,$  and  $0.1$  are shown in Figs. 4.3(a) and 4.3(b). The suppression function [Fig. 4.3(b)] accounts for the increase in thermal resistance compared to the diffusion solution [Fig. 4.3(a)], and reduces the effective thermal conductivity of the material. The suppression function is different than that previously assumed [i.e., a step function, see Eq. (4.1)] [71,73,75] in that phonons with  $\Lambda/L_p < 1$  contribute less and phonons with  $\Lambda/L_p > 1$  contribute more near  $\Lambda/L_p = 1$ .

The effect of changing  $\varepsilon$  is highlighted in Figs. 4.3(a) and 4.3(b). In this BTE solution, the resistance associated with the surface temperature jump  $R_\varepsilon = (4 - 2\varepsilon)/\varepsilon C v$  (for  $\rho = 1 - \varepsilon$ ) is independent of any experimentally controllable length scale, i.e.,  $L_p$ . Consequently, this resistance is always present and of the same magnitude but only becomes non-negligible when  $R_{i,x}$  is sufficiently small, which happens when the penetration depth is on the order of or smaller than the MFP. Decreasing  $\varepsilon$  increases  $R_\varepsilon$ , increasing the surface temperature jump, and hastening the onset of suppression. This fact can be qualitatively understood with an analogy to radiative transfer, i.e., the energy transfer rate from an isothermal gray surface will be less than that from an isothermal black surface at a given surface temperature. Reducing the phonon emissivity reduces the number of phonons emitted from the surface and hence reduces the energy transfer away from the surface, increasing the thermal resistance and reducing the effective thermal conductivity of the material in the nondiffusive regime. Furthermore, it is reasonable that emissivity is related to the interface resistance between the transducer and substrate in a

thermoreflectance experiment considering that emissivity affects the size of the surface temperature jump [123]. The effect of changing  $\varepsilon$  and  $\rho$  will be revisited later in this chapter.

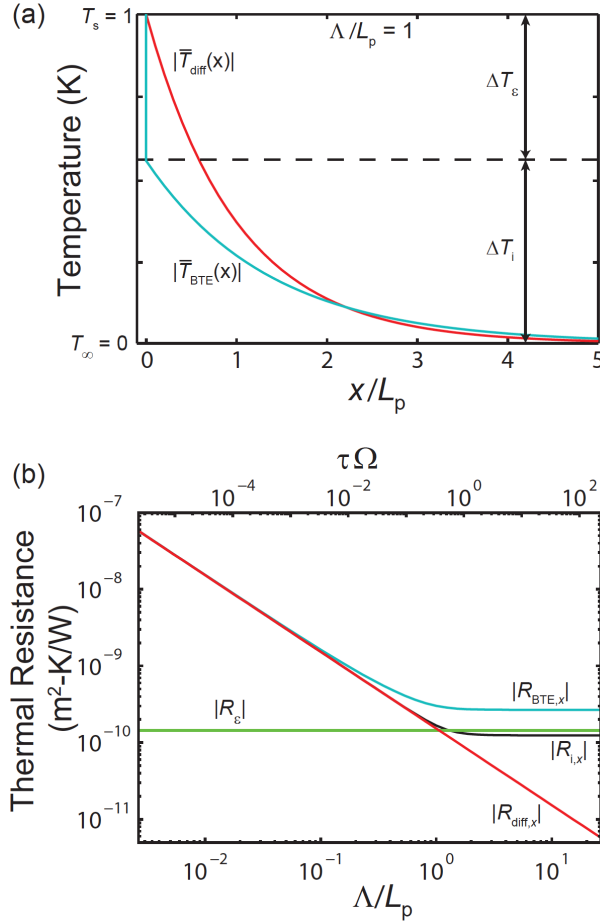


Fig. 4.2. 1-D planar geometry with temporally oscillating surface temperature and  $\varepsilon = 1 - \rho = 1$ . (a) Magnitude of the spatial temperature profiles from the diffusion and BTE solutions for  $\Lambda/L_p = 1$ . The BTE solution has two distinct regions that correspond to two distinct thermal resistances. (b) Magnitude of the thermal resistances  $R_{diff,x}$  and  $R_{BTE,x} = R_\varepsilon + R_{i,x}$  plotted as a function of  $\Lambda/L_p$  and  $\tau\Omega$ .

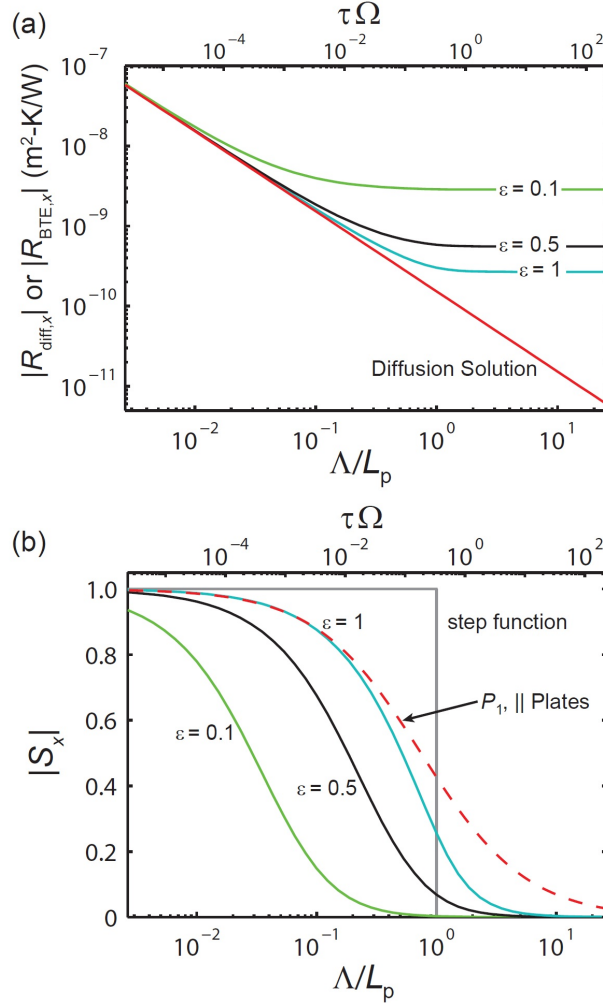


Fig. 4.3. 1-D planar geometry with temporally oscillating surface temperature and  $\epsilon = 1 - \rho = 1, 0.5,$  and  $0.1$ . (a) Magnitude of the thermal resistance from the diffusion and BTE solutions vs.  $\Lambda/L_p$  and  $\tau\Omega$ . The BTE predicts a higher thermal resistance than the diffusion solution, which can be accounted for by reducing the effective thermal conductivity in the diffusion solution. (b) Magnitude of the suppression function plotted as a function of  $\Lambda/L_p$  and  $\tau\Omega$ . These curves are compared to the  $P_1$  solution to the BTE for parallel, black, isothermal plates and to the step function suppression function [71,73,75].

To verify the behavior of this suppression function, it is compared to a solution to the gray BTE for two infinite, parallel, black ( $\epsilon = 1$ ), isothermal plates. This scenario is similar to the periodic problem except that in the periodic problem the oscillating surface temperature defines the length scale  $L_p$ . The solution to the isothermal problem is obtained using the  $P_1$  approximation and is plotted against the ratio of  $\Lambda$  and plate separation distance in Fig. 4.3(b). A similar trend instills confidence in the solution to the periodic problem and suggests that although  $L_p$  is not a physical boundary, it similarly suppresses contributions of phonons to thermal transport.

### III. Suppression function in a spherical geometry

In BB-FDTR and TDTR experiments, there are two relevant length scales: the thermal penetration depth and the spot size of the heating laser. Thus, in order to obtain an accurate suppression function for relating thermoreflectance measurements to  $k_{\text{accum}}$ , both length scales should be incorporated. The most accurate solution would involve solving the spectral BTE in cylindrical coordinates, under conditions of radially symmetric Gaussian surface heating. While other studies have reached numerical solutions to similar problems [36,72], one goal of this work is to reach an analytical solution for a simpler problem.

As depicted in Fig. 3.1(b), consider a sphere with radius  $r_0$  embedded in an infinite medium with temperature  $T(r \rightarrow \infty, t) = T_\infty = 0$  K and a temporally oscillating surface temperature at the sphere-medium interface. Solving the BTE within the medium will provide a solution that is dependent on  $L_p$  due to the periodic nature of the surface temperature as well as the effect of spot size, which can be captured by varying the radius of the embedded sphere. It should be noted that Chen solved a similar problem for a sphere with steady-state heating [17]. While this geometry is not an exact representation of a thermoreflectance experiment, the spherical symmetry (1-D in the radial direction) of the problem allows for the derivation of an analytical solution for the suppression function that is dependent on  $L_p$  and  $r_0$ .

I begin with the 1-D, gray BTE under the relaxation time approximation in spherical coordinates in the radial direction  $r$  (Ref. [39]),

$$\frac{1}{v} \frac{\partial n}{\partial t} + \mu \frac{\partial n}{\partial r} + \frac{1-\mu^2}{r} \frac{\partial n}{\partial \mu} = \frac{n_e - n}{\tau v} . \quad (4.13)$$

The  $\mu$ -dependence in Eq. (4.13) can be eliminated using the method of spherical harmonics ( $P_N$  approximation), which is a generalization of the Milne-Eddington approximation and has been thoroughly studied in spherically-symmetrical geometries in radiative transfer [118,124-126]. The method involves reducing the governing equation into a set of  $N$  simpler partial differential equations by taking advantage of the orthogonality of spherical harmonics. Applying the  $P_N$  approximation to Eq. (4.13) yields

$$\frac{1}{v} \frac{\partial n_l}{\partial t} + \frac{l+1}{2l+1} \frac{\partial n_{l+1}}{\partial r} + \frac{l}{2l+1} \frac{\partial n_{l-1}}{\partial r} + \frac{(l+1)(l+2)}{r(2l+1)} n_{l+1} - \frac{l(l-1)}{r(2l+1)} n_{l-1} + \frac{n_l}{\tau v} = \frac{n_0}{\tau v} \delta_{0l} , \quad (4.14)$$

where  $l = 0, 1, 2, \dots, N$  and  $\delta_{0l}$  is the Kronecker delta. In the limit where  $N \rightarrow \infty$ , the exact solution is obtained. Here the  $P_1$  approximation is used, which is typically accurate for scattering media at large optical thicknesses with decreasing accuracy as the optical thickness is decreased [118]. For this problem, large optical thicknesses correspond to  $L_p \gg \Lambda$ . Using the  $P_1$  approximation and separating variables in a similar fashion as Eq. (4.4), Eq. (4.13) reduces to

$$\frac{d\bar{n}_0}{dr} + 3 \left( \frac{i\Omega}{v} + \frac{1}{\tau v} \right) \bar{n}_1 = 0 , \quad (4.15a)$$

$$\frac{d\bar{n}_1}{dr} + \frac{i\Omega}{v} \bar{n}_0 + \frac{2}{r} \bar{n}_1 = 0 . \quad (4.15b)$$

By employing an analogous boundary condition as used for the planar solution, i.e.,  $\bar{n}^+(r = r_0) = \varepsilon \frac{C_\omega T_s}{4\pi} + \rho \bar{n}^-(r = r_0)$ , closed-form solutions for the spatial temperature and heat flux profiles for  $r \geq r_0$  are obtained as

$$\bar{T}_{\text{BTE}}(r) = \frac{r_0 \varepsilon T_s}{r \left[ (1 + \rho) \frac{4i(\beta\eta + \Psi)}{3\eta^2} + (1 - \rho) \right]} \exp \left[ -\frac{\eta}{L_p} (r - r_0) \right] , \quad (4.16a)$$

$$\bar{q}''_{\text{BTE}}(r) = \frac{\beta\eta \frac{r}{r_0} + \Psi}{\beta\eta + \Psi} \frac{r_0^2 \varepsilon T_s C v}{r^2 \left[ 2(1 + \rho) + (1 - \rho) \frac{3\eta^2}{2i(\beta\eta + \Psi)} \right]} \exp \left[ -\frac{\eta}{L_p} (r - r_0) \right] , \quad (4.16b)$$

where  $\Psi = \Lambda/r_0$ . The suppression function is found by determining  $k_{\text{eff}}$  of the infinite medium that equates the complex thermal resistance from the diffusion solution [ $R_{\text{diff},r} = 1/(\sqrt{i\Omega C k_{\text{eff}}} + k_{\text{eff}}/r_0)$ ] [93] to the complex thermal resistance defined by the BTE, which is equivalent to equating surface heat fluxes [17,80], and is

$$S_r(\Lambda, L_p, r_0, \varepsilon, \rho) = \frac{k_{\text{eff}}}{k_{\text{bulk}}} = \gamma + i \left( \frac{\beta}{\Psi} \right)^2 - \frac{\beta}{\Psi} \sqrt{2i\gamma - \left( \frac{\beta}{\Psi} \right)^2} , \quad (4.17)$$

where

$$\gamma = \frac{3\varepsilon/\Psi}{2(1+\rho)+(1-\rho)\frac{3\eta^2}{2i(\beta\eta+\Psi)}} \quad (4.18)$$

In Fig. 4.4(a), the magnitude of the complex thermal resistance is plotted as a function of  $\Lambda/L_p$  and  $\tau\Omega$  at different values of  $\Lambda/r_0$  with  $\varepsilon = 1 - \rho = 1$  for both the diffusion and BTE solutions. The thermal resistance from the diffusion equation (solid lines) highlights the interplay between  $r_0$  and  $L_p$ . When  $L_p \ll r_0$ , the solution converges to the planar solution [Fig. 4.3(a)], and when  $L_p \gg r_0$ , the diffusive thermal resistance becomes independent of  $\Lambda/L_p$ .

Similar to the planar solution, the total thermal resistance from the BTE is the sum of a surface component  $R_\varepsilon = (4 - 2\varepsilon)/\varepsilon C v$  (for  $\varepsilon = 1 - \rho$ ), which is the same as for the planar solution, and an intrinsic component  $R_{i,r}$

$$R_{i,r} = \frac{\eta^2}{2ik_{\text{bulk}}\left(\frac{\eta}{L_p} + \frac{1}{r_0}\right)} \quad (4.19)$$

As in the planar solution,  $R_{i,r}$  includes no effect from the surface properties ( $R_{i,r}$  is not a function of  $\varepsilon$  when  $\varepsilon = 1 - \rho$ ). For a given value of  $\varepsilon$ ,  $R_{i,r}$  converges to the diffusion solution when  $\Lambda/L_p \ll 1$  and asymptotes to  $\Lambda/(\sqrt{3}k_{\text{bulk}})$  when  $\Lambda/L_p \gg 1$ . But since the diffusive resistance decreases with increasing  $\Lambda/r_0$  when  $\Lambda/L_p \ll 1$ ,  $R_\varepsilon$  becomes non-negligible, and even dominates, when  $r_0$  is commensurate or smaller than the MFP. Because the total thermal resistance is the sum of  $R_\varepsilon$  and  $R_{i,r}$ , the BTE and diffusion solutions do not converge when  $\Lambda/L_p \ll 1$  at larger values of  $\Lambda/r_0$ . When  $\Lambda/r_0 = 0$ , the BTE solution converges to the planar solution from Eq. (4.9), as shown in Fig. 4.3(a).

The magnitude of the suppression function  $S_r(\Lambda, L_p, r_0, \varepsilon, \rho)$  is plotted in Fig. 4.4(b) for  $\varepsilon = 1 - \rho = 1$ . In the limit when  $r_0 \rightarrow \infty$ , the solution converges to the planar solution given in Eq. (4.12) and shown in Fig. 4.3(b). Changes in the suppression function with  $\Lambda/r_0$  over all  $\Lambda/L_p$  illustrate the interactions between the two length scales. In general, the smaller of  $L_p$  or  $r_0$  dominates suppression. For example, when  $\Lambda/L_p \ll 1$ , suppression is solely due to decreasing particle radius and is consistent with the TDTR experimental measurements by Minnich *et al.* of  $k$  vs.  $r_0$  that were independent of heating frequency [19]

and Chen in the case of steady-state heating [17]. According to the BTE solution, if either  $L_p$  or  $r_o$  are much smaller than the phonon MFP, that phonon will not contribute to  $k_{\text{exp}}$ . Under these circumstances, BB-FDTR and TDTR are inadequate for measuring the bulk thermal conductivity of a material.

The magnitude of the thermal resistance from the BTE and diffusion solutions and the magnitude of  $S_r(\Lambda, L_p, r_o, \epsilon, \rho)$  are plotted in Figs. 4.5(a) and 4.5(b) as a function of  $\Lambda/r_o$  for different values of  $\Lambda/L_p$  with  $\epsilon = 1 - \rho = 1$ . As heating frequency increases ( $\Lambda/L_p$  increases), additional suppression occurs from  $L_p$ , even at very low  $\Lambda/r_o$ . In Fig. 4.5(c), the analytical solution for  $S_r$  in the low  $\Omega$  limit ( $\Lambda/L_p = 0$ ) is compared to Chen's exact solution from Ref. [17] for a sphere with steady-state heating and the suppression function from Ref. [72] found numerically by solving the spectral BTE for a Gaussian-shaped laser spot. Due to the use of the  $P_1$  approximation, I find that Eq. (4.17) and the exact solution for a sphere with steady-state heating from Ref. [17] differ by a factor of two on the horizontal axis. I assert that this factor is not significant considering that the range of MFP spans four orders of magnitude in typical crystalline semiconductors [37,45,127]. Using a value of  $3r_o$  in Eq. (4.17), however, yields a suppression function that compares well with the suppression function from Ref. [72]. It is expected that there should be a correction factor to the spot size in Eq. (4.17) resulting from the geometry chosen to generate an analytical solution, i.e., the geometry of the spot is approximated as a finite sphere in an infinite medium while the actual experimental geometry is a Gaussian spot incident on a semi-infinite medium.

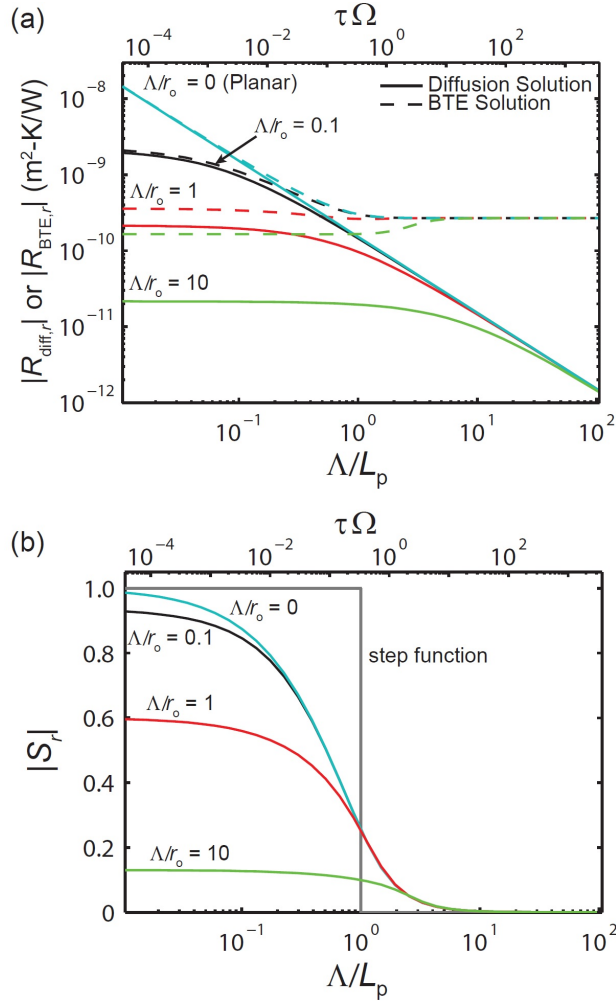


Fig. 4.4. Spherical particle embedded in an infinite medium with oscillating temperature at the surface of the sphere ( $r = r_o$ ) with  $\varepsilon = 1 - \rho = 1$ . (a) Magnitude of the thermal resistance from the diffusion and BTE solutions vs.  $\Lambda/L_p$  and  $\tau\Omega$ . (b) Magnitude of the suppression function plotted as a function of  $\Lambda/L_p$  and  $\tau\Omega$  for different values of  $\Lambda/r_o$ . For  $\Lambda/r_o = 0$ , the results collapse to the 1-D planar case shown in Figs. 4.3(a) and 4.3(b).

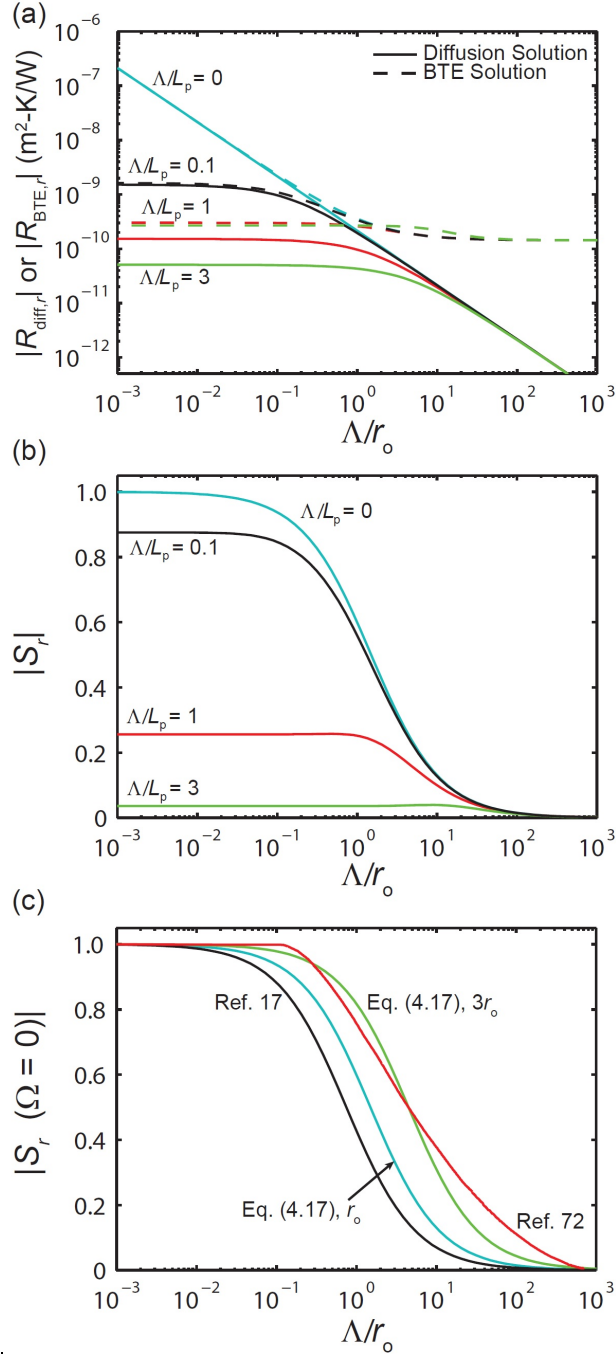


Fig. 4.5. Spherical particle embedded in an infinite medium with oscillating temperature at the surface of the sphere ( $r = r_0$ ) with  $\varepsilon = 1 - \rho = 1$ . (a) Magnitude of the thermal resistance from the diffusive and BTE solutions vs.  $\Lambda/r_0$  for different values of  $\Lambda/L_p$ . (b) Magnitude of the suppression function plotted as a function of  $\Lambda/r_0$  for different values of  $\Lambda/L_p$ . (c) Comparison of Eq. (4.17) when  $\Lambda/L_p = 0$  for a particle with radius  $r_0$  and a particle with radius  $3r_0$ , the exact solution for a sphere with steady-state heating from Ref. [17], and the suppression function found numerically by solving the spectral BTE for a Gaussian-shaped laser spot from Ref. [72]. Using a particle radius of  $3r_0$  in Eq. (4.17) compares well with numerical results from Ref. [72].

#### IV. Relating experiments and $k_{\text{accum}}$ using the suppression function

The suppression function can be used to relate experimental measurements to  $k_{\text{accum}}$  by mapping length scales to phonon MFPs. For example,  $k_{\text{accum}}$  can be obtained using Eq. (4.2) with thermoreflectance thermal conductivity measurements and the suppression function from Eq. (4.17) as inputs to the solution of an inverse problem, which was done by Minnich for TTG using convex optimization [80]. Alternatively, as is done here, the experimental measurement can be predicted given  $k_{\Lambda}$  as an input, which can be obtained from models (e.g., Callaway, Born-von Karman-Slack, first principles, etc.) [41,45,75]. This approach is less mathematically complex and allows for a direct comparison to the measurements.

Experimental measurements on silicon made by TDTR and BB-FDTR with predicted  $k_{\text{exp}}$  are compared in Figs. 4.6(a) and 4.6(b). The solid lines are the predicted accumulation functions from first principles calculations for silicon plotted as a function of MFP at temperatures of 80 and 300 K [48,128]. Using Eq. (4.2) with the suppression function from Eq. (4.17), these data are transformed into a predicted  $k_{\text{exp}}$  as would be measured by BB-FDTR or TDTR, shown as the dashed lines in Figs. 4.6(a) and 4.6(b). To make this transformation, a spot size of  $3r_0$  is used, which is found by comparing Eq. (4.17) to the suppression function for a Gaussian-shaped spot from Ref. [72] [see Fig. 4.5(c)] and a temperature independent value of  $\varepsilon = 1 - \rho$  in Eq. (4.17) that yields the best fit between experimental data and Eq. (4.2), i.e.,  $\varepsilon$  is used as a fitting parameter.

In Fig. 4.6(a),  $k_{\text{accum}}$  vs.  $\Lambda$  data from the first principles calculations are transformed into predicted  $k_{\text{exp}}$  vs.  $3r_0$  using Eq. (4.2) and Eq. (4.17). It is found that a value of  $\varepsilon = 1 - \rho = 0.88$  fits the TDTR measurements from Ref. [72] at temperatures of 80 and 300 K well. Here, a heating frequency of  $10^6$  Hz is used to determine  $\Lambda/L_p$ . It should be noted that the interface between the transducer and substrate for the TDTR data presented is aluminum/silicon. It is reasonable that the value of  $\varepsilon$  obtained by fitting is related to the properties of this interface. To show how increased TDTR heating frequency is expected to further suppress  $k_{\text{exp}}$  predicted  $k_{\text{exp}}$  vs.  $3r_0$  for a heating frequency of  $10^7$  Hz with  $\varepsilon = 1 - \rho = 0.88$  is also plotted.

In Fig. 4.6(b)  $k_{\text{accum}}$  vs.  $\Lambda$  data from the first principles calculations are transformed into predicted  $k_{\text{exp}}$  vs.  $L_p$  using Eq. (4.2) and Eq. (4.17). Here,  $L_p$  is determined using predicted  $k_{\text{exp}}$  instead of  $k_{\text{bulk}}$  to be consistent with the previous presentation of the experimental measurements [73] (see Chapter 3). It is found that a value of  $\varepsilon = 1 - \rho = 0.6$  best describes the BB-FDTR measurements from Ref. [73] at temperatures of 80 and 300 K. In the BB-FDTR results presented, the interface between the transducer and substrate is chromium/silicon rather than aluminum/silicon, and it is reasonable that there is a difference in the fitted value of  $\varepsilon$  for BB-FDTR compared to TDTR.

For silicon at a temperature of 300 K, the predicted  $k_{\text{exp}}$  vs.  $L_p$  for TDTR in Fig. 4.6(b) shows  $L_p$ -dependence over the measurement range although the experimental measurements show no  $L_p$ -dependence. The TDTR spot size used is the average of the range given in Ref. [71] ( $3r_o = 32.25 \mu\text{m}$ ). For BB-FDTR ( $3r_o = 10.2 \mu\text{m}$ ), the prediction compares well to experimental results at smaller  $L_p$ . The experimental measurements should plateau at larger  $L_p$  due to the effect of spot size, but this effect is not observed. More suppression is observed in BB-FDTR relative to TDTR for the available range of TDTR data because a smaller spot size was used and the emissivity is lower. At  $T = 80 \text{ K}$ , Eqs. (4.2) and (4.17) compare well with BB-FDTR experimental results over all  $L_p$ . At this temperature, phonons have longer MFPs and are significantly suppressed by the finite spot size, i.e., even for very large  $L_p$ ,  $k_{\text{exp}}$  will only attain approximately 30% of  $k_{\text{bulk}}$  due to the spot size restriction. In Figs. 4.6(a) and 4.6(b) the multiple time scales in TDTR that arise from using a pulsed laser are neglected and only the overarching modulation frequency is considered.

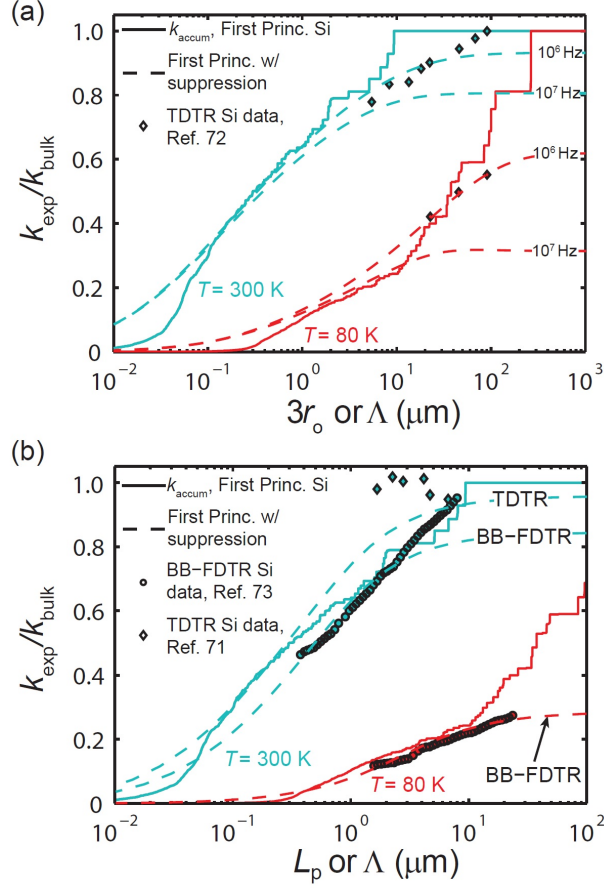


Fig. 4.6. Comparison of thermal conductivity measurements and predicted  $k_{\text{exp}}$  for silicon. (a)  $k_{\text{accum}}$  from first principles calculations (solid lines) is transformed into predicted  $k_{\text{exp}}$  vs.  $3r_o$  (dashed lines) by Eq. (4.2) using the suppression function from Eq. (4.17). A value of  $\epsilon = 0.88$  results in the best fit to TDTR measurements at  $T = 300\text{ K}$  and  $T = 80\text{ K}$  from Ref. [72] with a heating frequency of  $10^6\text{ Hz}$ . Predicted  $k_{\text{exp}}$  vs.  $3r_o$  for a heating frequency of  $10^7\text{ Hz}$  with  $\epsilon = 0.88$  is shown for comparison. In TDTR, the transducer/substrate interface is aluminum/silicon. (b)  $k_{\text{accum}}$  from first principles calculations is transformed into  $k_{\text{exp}}$  vs.  $L_p$  by Eq. (4.2) using the suppression function from Eq. (4.17). A value of  $\epsilon = 0.6$  results in the best fit to BB-FDTR measurements (circles) at  $T = 300\text{ K}$  and  $T = 80\text{ K}$  from Ref. [73]. In BB-FDTR, the transducer/substrate interface is chromium/silicon. Predicted  $k_{\text{exp}}$  vs.  $L_p$  with  $\epsilon = 0.88$  is compared to TDTR measurements from Ref. [71] (diamonds).

To generate predicted  $k_{\text{exp}}$  vs.  $L_p$  in Figs. 4.6(a) and 4.6(b), a suppression function derived from the gray BTE [Eq. (4.17)] is applied to the full phonon spectrum, where the MFP is frequency dependent. A similar approach was used by Collins *et al.* for TTG, in which a gray suppression function was applied to the full phonon spectrum to obtain predictions of thermal diffusivity as a function of grating period [81]. The results were compared to predictions of thermal diffusivity as a function of grating period calculated from the spectral BTE using phonon properties from first principles calculations. The authors

found favorable comparison in that the predicted effective thermal diffusivity varied by less than 7% over grating periods from  $10^{-1}$ - $10^6$  nm compared to the full spectral model of Si and PbTe at a temperature of 300 K.

The parameters  $\varepsilon$  and  $\rho$  in Eq. (4.17) arise from the analogy with radiative transfer and describe the ability of the surface to emit and reflect phonons. In the comparisons with experimental results  $\varepsilon$  is used as a fitting parameter but I propose that  $\varepsilon$  is related to the properties of the transducer/substrate interface in BB-FDTR and TDTR experiments. One interpretation is that the phonon emissivity is equal to the transmission coefficient of phonons from the transducer into the substrate [119].

Phonon transmission coefficients are used in the Landauer formulation to make predictions of interface thermal resistance. Following Ref. [42], the total interface resistance  $R_{\text{total}} = 2R_T + R_L$ , where  $R_T$  and  $R_L$  are the contributions from transverse and longitudinal acoustic phonons, can be derived in a similar manner as thermal conductivity. Beginning with Eqs. (2.10) and (2.11) in Ref. [129] and using a truncated Debye dispersion and Debye density of states,

$$R_T^{-1} = \frac{\alpha k_B^4 T^3}{8\pi^2 \hbar^3 v_T^2} \int_0^{\theta_T/T} \frac{y^4 e^y}{(e^y - 1)^2} dy \quad , \quad (4.20a)$$

$$R_L^{-1} = \frac{\alpha k_B^4 T^3}{8\pi^2 \hbar^3 v_L^2} \int_0^{\theta_L/T} \frac{y^4 e^y}{(e^y - 1)^2} dy \quad , \quad (4.20b)$$

where  $k_B$  is the Boltzmann constant,  $v_T$  and  $v_L$  are the transverse and longitudinal speeds of sound,  $\theta_T$  and  $\theta_L$  are the temperatures associated with the transverse and longitudinal Brillouin zone edge frequencies,  $y = \hbar\omega/k_B T$ , and  $\alpha = \varepsilon$  is the transmission coefficient. Using Eq. (4.20) with values of  $v_T$ ,  $v_L$ ,  $\theta_T$ , and  $\theta_L$  from Ref. [42] and the best fit values for  $\alpha = \varepsilon$ , it is found that  $R_{\text{total}} = 3.85 \text{ m}^2 \text{ K GW}^{-1}$  for a chromium/silicon interface and  $R_{\text{total}} = 2.63 \text{ m}^2 \text{ K GW}^{-1}$  for an aluminum/silicon interface at  $T = 300 \text{ K}$ . These values compare well with measured values reported in Ref. [73] and Ref. [19] at  $T = 300 \text{ K}$  ( $R_{\text{total}} = 4.76 \text{ m}^2 \text{ K GW}^{-1}$  for chromium/silicon interface and  $R_{\text{total}} = 2.78 \text{ m}^2 \text{ K GW}^{-1}$  for aluminum/silicon interface). Furthermore, because  $\varepsilon$  influences the onset of suppression, I hypothesize that the interface properties contribute to the discrepancy between room temperature BB-FDTR and

TDTR heating frequency dependence for silicon [see Fig. 4.6(b)], though a spectral phonon model that includes the transducer may be required to reconcile this unresolved question.

It is important to note that previous nondiffusive measurements have been solely attributed to reduced thermal conductivity, i.e., the interface resistance between the substrate and the transducer is assumed constant in diffuse interpretations of the experiments [19,71,73,75]. In this formulation, a comparison is made between a thermal resistance from the BTE that includes a surface temperature drop to a diffusion solution that does not account for an interface thermal resistance (no surface temperature drop). As a result, the effect of  $R_e$  [Eq. (4.13a)] is included in the definition of  $k_{\text{eff}}$ . To generate a suppression function that does not include the surface temperature drop, one can equate the appropriate complex diffusive thermal resistance to  $R_{i,x}$  or  $R_{i,r}$ , resulting in  $S_i = 1/(1 + i\tau\Omega)$ . This result is equivalent for both the planar and spherical geometries and is independent of the particle radius. In Ref. [73], a suppression function was determined from a numerical solution to the 1-D, gray BTE for phonons travelling in the positive and negative  $x$ -direction ( $\mu = 1$  or  $-1$ ). The result is related to  $S_i$ ; the difference being a factor of  $\pi/2$  on the  $x$ -axis, which stems from considering  $-1 \leq \mu \leq 1$  when determining  $S_i$  [130].

To include heating frequency-dependent interface resistance between the transducer and the substrate, a BTE formulation that explicitly includes an interface could be considered and compared to a diffusion solution including an interface. How the transducer affects nondiffusive transport, which is important in interpreting the experiments, has not been explicitly addressed, though it may contribute to the discrepancy between heating frequency-dependent measurements of silicon by BB-FDTR and TDTR.

## V. Summary

An analytical suppression function for a system geometrically similar to a thermoreflectance experiment was obtained by solving the BTE for a gray medium. The result accounts for the two dominant length scales in thermoreflectance experiments: thermal penetration depth and heating laser spot radius. The suppression function is used to predict  $k_{\text{exp}}$  vs.  $L_p$  and  $k_{\text{exp}}$  vs.  $3r_o$  to make a direct comparison to experimental measurements by both BB-FDTR and TDTR. The results corroborate the use of BB-

FDTR and TDTR as tools for identifying  $k_{\text{accum}}$  by generating nondiffusive transport and provide insight and understanding of the measurements. Furthermore, the results suggest that if either  $L_p$  or  $r_o$  are much smaller than the phonon MFPs that dominate  $k$ , BB-FDTR and TDTR are inadequate for measuring the bulk thermal conductivity of a material. The phonon surface properties  $\varepsilon$  and  $\rho$  affect suppression and may explain discrepancies between TDTR and BB-FDTR measurements of similar samples with different transducers. It is clear that powerful new insight is offered by nondiffusive thermal transport measurements paired with the experiment-specific suppression function to map data into real energy carrier properties.

## 5. ELECTRON-PHONON NON-EQUILIBRIUM IN THE TRANSDUCER

### I. Overview

One important detail about TDTR and FDTR is the existence of a thin metal layer, which is coated on the sample surface. This metal layer acts as a transducer that imparts information about the sample surface temperature to the probe laser due to the thermoreflectance properties of the metal. The transducer layer introduces two major complications into the analysis and interpretation of the experiments: (1) an interface exists between the transducer and substrate, which is typically characterized by a thermal interface conductance  $G$  that becomes an additional fitting parameter and (2) the interaction between electrons and phonons in the metal transducer cannot necessarily be neglected at short time scales. These two complications have been suggested as reasons for the discrepancy between TDTR and FDTR measurements of thermal conductivity as a function of heating frequency [78,131]. In this chapter, I address and discuss the latter.

Typically for TDTR the transducer material is aluminum, while for recent implementation of FDTR the transducer is gold with a thin chromium adhesion layer [74,76]. In the metal transducer layer, electrons are primarily responsible for the thermal conductivity and phonons are responsible for the heat capacity. Both electrons and phonons carry energy in metals and the rate at which electrons and phonons share energy with one another is characterized by the electron-phonon coupling parameter  $g$ . At a temperature of 300 K measurements find  $g_{Al} = 24.5 \times 10^{16} \text{ W m}^{-3} \text{ K}^{-1}$  and  $g_{Au} = 2.2 \times 10^{16} \text{ W m}^{-3} \text{ K}^{-1}$  [132,133]. The electron-phonon coupling parameter in aluminum is an order of magnitude larger than gold, physically indicating that electrons and phonons thermally equilibrate faster in aluminum than in gold.

The timescale for electron-phonon equilibration has been observed to be on the order of the lattice heat capacity divided by  $g$  [108]. The timescales in TDTR (laser pulse width, pump-probe delay time, time between laser pulses, and  $1/2\pi f$ ) and FDTR ( $1/2\pi f$ ) are comparable to the electron-phonon equilibrium time. Consequently, non-equilibrium between electrons and phonons occurs in these

experiments and must be considered when interpreting the experimental data. A tool well suited to capture these physics is the two-temperature diffusion model, which has been applied to thermoreflectance experiments in the literature [132,134-139]. Furthermore, it has been shown that there is indirect heating of a thin metal layer with strong electron-phonon coupling when in contact with an optically excited layer with weak electron phonon coupling [132]. This results in non-surface heating in thermoreflectance experiments with similar geometry, such as in FDTR with a gold/chromium transducer [73-75]. The literature, however, lacks a two-temperature formulation applicable to thermoreflectance experiments that accounts for arbitrary, non-surface heating.

Here, I formulate a two-temperature model based on the work in Ref. [139] with the added functionality to deposit heat at any location in the multi-layer sample geometry. I also perform a sensitivity analysis of this model to determine important parameters in the solution and establish a guideline for when the use of a two-temperature model is necessary to interpret thermoreflectance data. A case study is performed using existing data from Ref. [73]. The transducer layer is characterized using SiO<sub>2</sub> and platinum substrates. After characterizing the transducer, silicon FDTR data are refit with the two-temperature model. Accounting for electron-phonon non-equilibrium processes in the transducer reduces the thermal conductivity heating frequency dependence observed in FDTR. Additional FDTR measurements on silicon with a gold/chromium/aluminum transducer are performed and show limited heating frequency dependence, indicating that the transducer/substrate interface plays a role in the observed heating frequency dependent-thermal conductivity. This work appears in *Journal of Applied Physics*, vol. 118, pp. 235101, 2015 with contributions from co-authors L. C. Wei and J. A. Malen and is reprinted with permission from AIP Publishing LLC © 2015 [140].

## II. Two-temperature formulation

The two-temperature model in an N-layered geometry, as depicted in Fig. 5.1, is solved in a similar fashion as Ref. [139]. The two-temperature model describes heat transfer in the n<sup>th</sup> layer through two distinct channels, each having its own thermal conductivity ( $k_{n,1}$  and  $k_{n,2}$ ), volumetric heat capacity

( $C_{n,1}$  and  $C_{n,2}$ ) and temperature ( $\theta_{n,1}$  and  $\theta_{n,2}$ ). Heat is exchanged between each channel at a rate proportional to the coupling parameter in that layer  $g_n$ . The thickness of each layer is  $t_n$  with the  $N^{\text{th}}$  layer being semi-infinite. I account for temporally periodic, spatially (in the  $r$ -direction) Gaussian heat input at the surface and into each channel of each layer at a distance  $\delta_n$  from the beginning of the  $n^{\text{th}}$  layer [e.g., to model the spatial (in the  $z$ -direction) absorption of the pump laser due to the optical penetration depth of the light in the metal transducer]. Accounting for arbitrary periodic heat input into any layer at any location within that layer is a new contribution to the literature relative to the two-temperature model presented in Ref. [139].

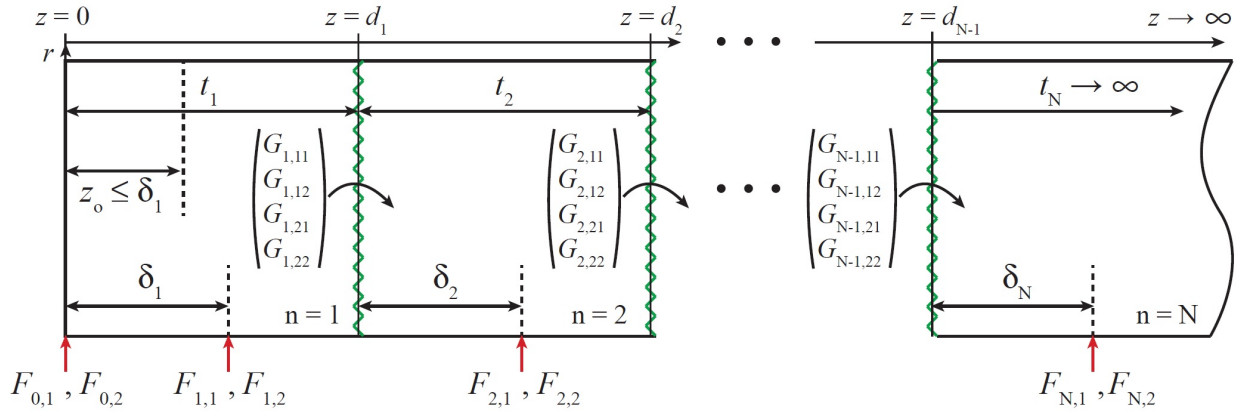


Fig. 5.1. Schematic of the two-temperature model for an  $N$ -layered sample with arbitrarily valued and located input heat fluxes in each layer.

In an FDTR experiment, a periodic, radially Gaussian heat flux with angular frequency  $\Omega = 2\pi f$  is incident on the sample. Thus, to be consistent with the geometry of the experiment and to take advantage of the cylindrical symmetry of the problem, the coupled heat diffusion equation in cylindrical coordinates is solved for the temperatures  $\theta_{n,1}(t, z, r)$  and  $\theta_{n,2}(t, z, r)$  of the  $n^{\text{th}}$  layer [Eqs. (5.1a) and (5.1b)] that includes heat deposition profiles into each channel of the  $n^{\text{th}}$  layer  $F_{n,1}$  and  $F_{n,2}$  [Eqs. (5.1c) and (5.1d)],

$$C_{n,1} \frac{\partial \theta_{n,1}}{\partial t} = k_{n,1} \left[ \frac{\partial^2 \theta_{n,1}}{\partial z^2} + \frac{\eta_{n,1}}{r} \frac{\partial}{\partial r} \left( r \frac{\partial \theta_{n,1}}{\partial r} \right) \right] + g_n (\theta_{n,2} - \theta_{n,1}), \quad (5.1a)$$

$$C_{n,2} \frac{\partial \theta_{n,2}}{\partial t} = k_{n,2} \left[ \frac{\partial^2 \theta_{n,2}}{\partial z^2} + \frac{\eta_{n,2}}{r} \frac{\partial}{\partial r} \left( r \frac{\partial \theta_{n,2}}{\partial r} \right) \right] + g_n (\theta_{n,1} - \theta_{n,2}), \quad (5.1b)$$

$$F_{n,1} = -k_{n,1} \frac{\partial \theta_{n,1}}{\partial z} \Big|_{z=\delta_n} = \frac{4H_{n,1}}{r_{\text{spot,pump}}^2} e^{i\Omega t} e^{-2r^2/r_{\text{spot,pump}}^2}, \quad (5.1c)$$

$$F_{n,2} = -k_{n,2} \frac{\partial \theta_{n,2}}{\partial z} \Big|_{z=\delta_n} = \frac{4H_{n,2}}{r_{\text{spot,pump}}^2} e^{i\Omega t} e^{-2r^2/r_{\text{spot,pump}}^2}, \quad (5.1d)$$

where  $\eta_{n,1}$  and  $\eta_{n,2}$  are the ratios of thermal conductivity in the  $r$  and  $z$  directions for each channel in the  $n^{\text{th}}$  layer (a value of 1 indicates an isotropic material),  $r_{\text{spot,pump}}$  is the  $1/e^2$  pump beam radius, and  $H_{n,1}$  and  $H_{n,2}$  are the amplitudes of the heat absorbed into channels 1 and 2. Here it is assumed that thermal conductivity is independent of temperature and location within each layer.

Since the time dependence of the temperature follows the heating and varies as  $e^{i\Omega t}$ , separation of variables is performed. Furthermore, I take advantage of the cylindrical symmetry of the problem and perform a Hankel transform [93]. The result reduces the governing equations and heat deposition in the  $n^{\text{th}}$  layer to

$$\frac{d^2 T_{n,1}}{dz^2} = \frac{C_{n,1} i\Omega + g_n + k_{n,1} \eta_{n,1} \kappa^2}{k_{n,1}} T_{n,1} - \frac{g_n}{k_{n,1}} T_{n,2}, \quad (5.2a)$$

$$\frac{d^2 T_{n,2}}{dz^2} = \frac{C_{n,2} i\Omega + g_n + k_{n,2} \eta_{n,2} \kappa^2}{k_{n,2}} T_{n,2} - \frac{g_n}{k_{n,2}} T_{n,1}, \quad (5.2b)$$

$$\hat{F}_{n,1} = -k_{n,1} \frac{\partial T_{n,1}}{\partial z} \Big|_{z=\delta_n} = H_{n,1} e^{-\kappa^2 r_{\text{spot,pump}}^2/8} \quad (5.2c)$$

$$\hat{F}_{n,2} = -k_{n,2} \frac{\partial T_{n,2}}{\partial z} \Big|_{z=\delta_n} = H_{n,2} e^{-\kappa^2 r_{\text{spot,pump}}^2/8} \quad (5.2d)$$

where  $T_{n,1}(z, \kappa)$  and  $T_{n,2}(z, \kappa)$  are the time-independent, transformed temperatures in the  $n^{\text{th}}$  layer (in units  $\text{K m}^2$ ),  $\hat{F}_{n,1}$  and  $\hat{F}_{n,2}$  are the time-independent, transformed heat deposition profiles in the  $n^{\text{th}}$  layer,

and  $\kappa$  is the Hankel variable. It should be noted that the surface heating profiles  $\hat{F}_{0,1}$  and  $\hat{F}_{0,2}$  are identical in form to Eqs. (5.2c) and (5.2d) only evaluated at  $z = 0$ . For convenience, I define  $\alpha_{n,1} = (C_{n,1}i\Omega + g_n + k_{n,1}\eta_{n,1}\kappa^2)/k_{n,1}$  and  $\alpha_{n,2} = (C_{n,2}i\Omega + g_n + k_{n,2}\eta_{n,2}\kappa^2)/k_{n,2}$ . Converting Eqs. (5.2a) and (5.2b) into matrix form yields

$$\frac{d^2}{dz^2} \begin{bmatrix} T_{n,1} \\ T_{n,2} \end{bmatrix} = \begin{bmatrix} \alpha_{n,1} & -g_n/k_{n,1} \\ -g_n/k_{n,2} & \alpha_{n,2} \end{bmatrix} \begin{bmatrix} T_{n,1} \\ T_{n,2} \end{bmatrix}, \quad (5.3)$$

The general solution to Eq. (5.3) in matrix form is

$$\begin{bmatrix} T_{n,1} \\ T_{n,2} \end{bmatrix} = \mathbf{X}_n \begin{bmatrix} B_{n,1}^- e^{-\lambda_{n,1}z} + B_{n,1}^+ e^{\lambda_{n,1}z} \\ B_{n,2}^- e^{-\lambda_{n,2}z} + B_{n,2}^+ e^{\lambda_{n,2}z} \end{bmatrix}, \quad (5.4)$$

where  $B_{n,1}^-$ ,  $B_{n,1}^+$ ,  $B_{n,2}^-$ , and  $B_{n,2}^+$  are constants of integration of the  $n^{\text{th}}$  layer to be determined by the boundary conditions,  $\lambda_{n,1}^2$  and  $\lambda_{n,2}^2$  are the eigenvalues of the  $n^{\text{th}}$  layer found from the characteristic matrix in Eq. (5.3), and  $\mathbf{X}_n$  is the associated eigenvector matrix of the  $n^{\text{th}}$  layer

$$\mathbf{X}_n = \begin{bmatrix} v_{n,1} & v_{n,2} \\ u_{n,1} & u_{n,2} \end{bmatrix}. \quad (5.5)$$

Here,  $v_{n,1}$  and  $u_{n,1}$  are the components of the eigenvector associated with the eigenvalue  $\lambda_{n,1}^2$  and  $v_{n,2}$  and  $u_{n,2}$  are the components of the eigenvector associated with the eigenvalue  $\lambda_{n,2}^2$ . I define

$$\mathbf{Y}_n = \begin{bmatrix} k_{n,1} & 0 \\ 0 & k_{n,2} \end{bmatrix} \begin{bmatrix} v_{n,1} & v_{n,2} \\ u_{n,1} & u_{n,2} \end{bmatrix} \begin{bmatrix} \lambda_{n,1} & 0 \\ 0 & \lambda_{n,2} \end{bmatrix} = \begin{bmatrix} \gamma_{n,11}v_{n,1} & \gamma_{n,12}v_{n,2} \\ \gamma_{n,21}u_{n,1} & \gamma_{n,22}u_{n,2} \end{bmatrix}, \quad (5.6)$$

where  $\gamma_{n,ab} = k_{n,a}\lambda_{n,b}$ . Finally, the time-independent, transformed temperature  $[T_{n,1}(z, \kappa)$  and  $T_{n,2}(z, \kappa)]$  and heat flux  $[q''_{n,1}(z, \kappa)$  and  $q''_{n,2}(z, \kappa)]$  profiles for each channel at position  $z$  in the  $n^{\text{th}}$  layer in matrix form are

$$\boldsymbol{\Psi}_n^z = \mathbf{X}_n \mathbf{A}_n^z \mathbf{B}_n, \quad (5.7a)$$

$$\boldsymbol{\Psi}_n^z = \begin{bmatrix} T_{n,1}(z, \kappa) \\ T_{n,2}(z, \kappa) \\ q_{n,1}''(z, \kappa) \\ q_{n,2}''(z, \kappa) \end{bmatrix}, \quad (5.7b)$$

$$\boldsymbol{\chi}_n = \begin{bmatrix} \mathbf{X}_n & \mathbf{X}_n \\ \mathbf{Y}_n & -\mathbf{Y}_n \end{bmatrix}, \quad (5.7c)$$

$$\mathbf{A}_n^z = \begin{bmatrix} e^{-\lambda_{n,1}z} & 0 & 0 & 0 \\ 0 & e^{-\lambda_{n,2}z} & 0 & 0 \\ 0 & 0 & e^{\lambda_{n,1}z} & 0 \\ 0 & 0 & 0 & e^{\lambda_{n,2}z} \end{bmatrix}, \quad (5.7d)$$

$$\mathbf{B}_n = \begin{bmatrix} B_{n,1}^- \\ B_{n,2}^- \\ B_{n,1}^+ \\ B_{n,2}^+ \end{bmatrix}, \quad (5.7e)$$

where position  $z$  and layer  $n$  are indicated by the superscript and subscript.

The unknowns in Eq. (5.7) are the values in the vector  $\mathbf{B}_n$ , which are the constants of integration resulting from the solution to Eq. (5.2). To obtain these values for each layer, the boundary conditions are used. First consider the heat input into each layer. In layer  $n$ , the spatial temperature and heat flux profiles to the left and right of  $\delta_n$  are defined as  $\boldsymbol{\Psi}_n^{z,L}$  and  $\boldsymbol{\Psi}_n^{z,R}$ , as shown in Fig. 5.2(a). The quantities  $\boldsymbol{\Psi}_n^{z,L}$  and  $\boldsymbol{\Psi}_n^{z,R}$  are related by equating temperatures at  $z = d_{n-1} + \delta_n$  and balancing heat fluxes such that

$$\boldsymbol{\Psi}_n^{z=d_{n-1}+\delta_n,L} + \mathbf{Q}_n = \boldsymbol{\Psi}_n^{z=d_{n-1}+\delta_n,R} \rightarrow \boldsymbol{\chi}_n \mathbf{A}_n^{z=d_{n-1}+\delta_n} \mathbf{B}_n^L + \mathbf{Q}_n = \boldsymbol{\chi}_n \mathbf{A}_n^{z=d_{n-1}+\delta_n} \mathbf{B}_n^R, \quad (5.8a)$$

$$\mathbf{Q}_n = \begin{bmatrix} 0 \\ 0 \\ \hat{F}_{n,1} \\ \hat{F}_{n,2} \end{bmatrix}. \quad (5.8b)$$

In the case where  $\hat{F}_{n,1}$  and  $\hat{F}_{n,2}$  both equal zero (i.e., when heating is purely at the surface),  $\mathbf{B}_n^L$  equals  $\mathbf{B}_n^R$  and thus  $\boldsymbol{\Psi}_n^{z,L} = \boldsymbol{\Psi}_n^{z,R} = \boldsymbol{\Psi}_n^z$ . Note that the matrix  $\boldsymbol{\chi}_n$  is the same on either side of  $\delta_n$ .

Now consider the interface between layer  $n$  and layer  $n+1$  at  $z = d_n$ , as shown in Fig. 5.2(b). At this interface, there is an interface thermal conductance between each channel in layer  $n$  and each channel in layer  $n+1$  ( $G_{n,11}, G_{n,12}, G_{n,21}, G_{n,22}$ ), such that the temperature and heat flux profiles on either side of the interface are related by

$$\boldsymbol{\Psi}_n^{z=d_n,R} = \mathbf{G}_{n \rightarrow n+1} \boldsymbol{\Psi}_{n+1}^{z=d_n,L} \quad \rightarrow \quad \boldsymbol{\chi}_n \mathbf{A}_n^{z=d_n} \mathbf{B}_n^R = \mathbf{G}_{n \rightarrow n+1} \boldsymbol{\chi}_{n+1} \mathbf{A}_{n+1}^{z=d_n} \mathbf{B}_{n+1}^L. \quad (5.9)$$

Here,  $\mathbf{G}_{n \rightarrow n+1}$  is determined by balancing heat fluxes across the interface and is given by [139]

$$\mathbf{G}_{n \rightarrow n+1} = \begin{bmatrix} G_{n,22}a_1 & -G_{n,21}a_2 & G_{n,22} & -G_{n,21} \\ -G_{n,12}a_1 & G_{n,11}a_2 & -G_{n,12} & G_{n,11} \\ a_5 & -a_5 & G_{n,22}a_3 & -G_{n,21}a_3 \\ -a_5 & a_5 & -G_{n,12}a_4 & G_{n,11}a_4 \end{bmatrix}, \quad (5.10a)$$

$$a_1 = \frac{G_{n,11} + G_{n,21}}{G_{n,11}G_{n,22} - G_{n,12}G_{n,21}},$$

$$a_2 = \frac{G_{n,12} + G_{n,22}}{G_{n,11}G_{n,22} - G_{n,12}G_{n,21}},$$

$$a_3 = \frac{G_{n,11} + G_{n,12}}{G_{n,11}G_{n,22} - G_{n,12}G_{n,21}}, \quad (5.10b)$$

$$a_4 = \frac{G_{n,22} + G_{n,21}}{G_{n,11}G_{n,22} - G_{n,12}G_{n,21}},$$

$$a_5 = G_{n,22}G_{n,21}a_3 + G_{n,11}G_{n,12}a_4.$$

Since the  $N^{\text{th}}$  layer is semi-infinite, the temperature must decay to the initial temperature as  $z \rightarrow \infty$ . For simplicity, I define  $T_{N,1}(z \rightarrow \infty, \kappa) = 0$  and  $T_{N,2}(z \rightarrow \infty, \kappa) = 0$ , which implies this solution is for the change in temperature around the initial temperature. Thus,

$$\chi_N \mathbf{A}_N^{z \rightarrow \infty} \mathbf{B}_N^R = \begin{bmatrix} 0 \\ 0 \\ q''_{N,1}(z \rightarrow \infty, \kappa) \\ q''_{N,2}(z \rightarrow \infty, \kappa) \end{bmatrix} = \boldsymbol{\Psi}_N^{z \rightarrow \infty, R}. \quad (5.11)$$

Lastly, at  $z = 0$  I specify the surface heat flux quantities  $\hat{F}_{0,1}$  and  $\hat{F}_{0,2}$  (i.e., the magnitude of the temporal surface heating profile) such that

$$\begin{bmatrix} T_{1,1}(z = 0, \kappa) \\ T_{1,2}(z = 0, \kappa) \\ \hat{F}_{0,1} \\ \hat{F}_{0,2} \end{bmatrix} = \boldsymbol{\Psi}_1^{z=0, L} = \chi_1 \mathbf{B}_1^L. \quad (5.12)$$

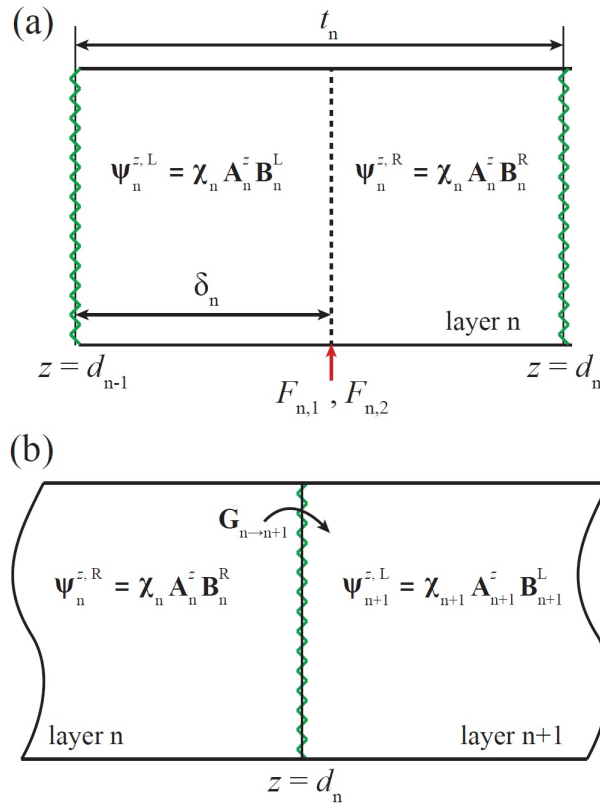


Fig. 5.2. Formulating the boundary conditions in (a) layer n on either side of the input heat flux at  $z = d_{n-1} + \delta_n$  and (b) layers n and n+1, on either side of the  $n^{\text{th}}$  interface corresponding to  $z = d_n$ .

The vectors  $\mathbf{B}_n^L$  and  $\mathbf{B}_n^R$  are determined using Eqs. (5.8), (5.9), (5.11), and (5.12). Once these values are determined, the time-independent, transformed temperature and heat flux profiles in the  $n^{\text{th}}$

layer are found by substitution into  $\boldsymbol{\Psi}_n^{z,L} = \boldsymbol{\chi}_n \mathbf{A}_n^z \mathbf{B}_n^L$  and  $\boldsymbol{\Psi}_n^{z,R} = \boldsymbol{\chi}_n \mathbf{A}_n^z \mathbf{B}_n^R$ . Rearranging Eqs. (5.11) and (5.12) yields the unknown  $\mathbf{B}$  vectors for the left portion of the first layer and the right portion of the last layer

$$\mathbf{B}_1^L = [\boldsymbol{\chi}_1]^{-1} \boldsymbol{\Psi}_1^{z=0,L}, \quad (5.13a)$$

$$\mathbf{B}_N^R = [\mathbf{A}_N^{z \rightarrow \infty}]^{-1} [\boldsymbol{\chi}_N]^{-1} \boldsymbol{\Psi}_N^{z \rightarrow \infty, R}. \quad (5.13b)$$

The remaining  $\mathbf{B}$  vectors are determined by rearranging Eqs. (5.8) and (5.9)

$$\mathbf{B}_n^L = [\mathbf{A}_n^{z=d_{n-1}}]^{-1} [\boldsymbol{\chi}_n]^{-1} [\mathbf{G}_{n-1 \rightarrow n}]^{-1} \boldsymbol{\chi}_{n-1} \mathbf{A}_{n-1}^{z=d_{n-1}} \mathbf{B}_{n-1}^R, \quad (5.14a)$$

$$\mathbf{B}_n^R = [\mathbf{A}_n^{z=d_{n-1}+\delta_n}]^{-1} [\boldsymbol{\chi}_n]^{-1} (\boldsymbol{\chi}_n \mathbf{A}_n^{z=d_{n-1}+\delta_n} \mathbf{B}_n^L + \mathbf{Q}_n). \quad (5.14b)$$

It should be noted that  $\mathbf{A}_n^{z_1} [\mathbf{A}_n^{z_2}]^{-1} = \mathbf{A}_n^{z_1-z_2}$ . For simplification,  $\boldsymbol{\mu}_n = \boldsymbol{\chi}_n \mathbf{A}_n^{z=t_n} [\boldsymbol{\chi}_n]^{-1}$  and  $\boldsymbol{\beta}_n = \boldsymbol{\chi}_n \mathbf{A}_n^{z=t_n-\delta_n} [\boldsymbol{\chi}_n]^{-1}$ . Writing  $\boldsymbol{\Psi}_N^{z \rightarrow \infty, R}$  in terms of  $\boldsymbol{\Psi}_1^{z=0,L}$  yields

$$\begin{aligned} \boldsymbol{\Psi}_N^{z \rightarrow \infty, R} &= \left( \prod_{j=2}^N \boldsymbol{\mu}_{2-j+N} [\mathbf{G}_{1-j+N \rightarrow 2-j+N}]^{-1} \right) \boldsymbol{\mu}_1 \boldsymbol{\Psi}_1^{z=0,L} \\ &+ \sum_{m=1}^N \left[ \left( \prod_{j=2}^{1-m+N} \boldsymbol{\mu}_{2-j+N} [\mathbf{G}_{1-j+N \rightarrow 2-j+N}]^{-1} \right) \boldsymbol{\beta}_m \mathbf{Q}_m \right] \end{aligned} \quad (5.15)$$

The resulting form of Eq. (5.15) is

$$\boldsymbol{\Psi}_N^{z \rightarrow \infty, R} = \overbrace{\begin{bmatrix} p_{11} & p_{12} & p_{13} & p_{14} \\ p_{21} & p_{22} & p_{23} & p_{24} \\ p_{31} & p_{32} & p_{33} & p_{34} \\ p_{41} & p_{42} & p_{43} & p_{44} \end{bmatrix}}^{\mathbf{P}} \boldsymbol{\Psi}_1^{z=0,L} + \overbrace{\begin{bmatrix} s_1 \\ s_2 \\ s_3 \\ s_4 \end{bmatrix}}^{\mathbf{S}}, \quad (5.16)$$

where the matrix  $\mathbf{P}$  is the matrix proportional to  $\boldsymbol{\Psi}_1^{z=0,L}$  from the first term in Eq. (5.15) and the vector  $\mathbf{S}$  is a result of the bracketed second term in Eq. (5.15) and arises from the heat flux source terms  $F_{n,1}$  and  $F_{n,2}$  in each layer. The time-independent, transformed surface temperatures at  $z = 0$  can be determined as

$$\begin{bmatrix} T_{1,1}(z=0, \kappa) \\ T_{1,2}(z=0, \kappa) \end{bmatrix} = - \begin{bmatrix} p_{11} & p_{12} \\ p_{21} & p_{22} \end{bmatrix}^{-1} \begin{bmatrix} p_{13} & p_{14} \\ p_{23} & p_{24} \end{bmatrix} \begin{bmatrix} \hat{F}_{0,1} \\ \hat{F}_{0,2} \end{bmatrix} - \begin{bmatrix} p_{11} & p_{12} \\ p_{21} & p_{22} \end{bmatrix}^{-1} \begin{bmatrix} S_1 \\ S_2 \end{bmatrix}. \quad (5.17)$$

Once the transformed surface temperatures are known, the  $\mathbf{B}$  vector for any layer can be determined from Eqs. (5.13) and (5.14). From there it is straightforward to determine the time-independent, transformed temperature and heat flux profiles in the  $n^{\text{th}}$  layer using  $\boldsymbol{\Psi}_n^{z,L} = \boldsymbol{\chi}_n \mathbf{A}_n^z \mathbf{B}_n^L$  and  $\boldsymbol{\Psi}_n^{z,R} = \boldsymbol{\chi}_n \mathbf{A}_n^z \mathbf{B}_n^R$ . For example, to determine the temperature and heat flux at a value of  $z = z_o$ , where  $0 \leq z_o \leq \delta_1$ , as shown in Fig. 5.1, calculate

$$\begin{bmatrix} T_{1,1}(z = z_o, \kappa) \\ T_{1,2}(z = z_o, \kappa) \\ q''_{1,1}(z = z_o, \kappa) \\ q''_{1,2}(z = z_o, \kappa) \end{bmatrix} = \boldsymbol{\chi}_1 \mathbf{A}_1^{z=z_o} [\boldsymbol{\chi}_1]^{-1} \begin{bmatrix} T_{1,1}(z = 0, \kappa) \\ T_{1,2}(z = 0, \kappa) \\ \hat{F}_{0,1} \\ \hat{F}_{0,2} \end{bmatrix}, \quad (5.18)$$

where the transformed surface temperatures were found from Eq. (5.17) and the surface heat fluxes quantities  $\hat{F}_{0,1}$  and  $\hat{F}_{0,2}$  are user-defined quantities [see Eqs. (5.2c) and (5.2d)].

After determining  $T_{1,1}(z = z_o, \kappa)$  and  $T_{1,2}(z = z_o, \kappa)$  from Eq. (5.18), I perform an inverse Hankel transform and multiply by the time-dependent solution  $e^{i\Omega t}$  to obtain  $\theta_{1,1}(t, z = z_o, r)$  and  $\theta_{1,2}(t, z = z_o, r)$  as

$$\theta_{1,1}(t, z = z_o, r) = e^{i\Omega t} \int_0^\infty T_{1,1}(z = z_o, \kappa) J_0(\kappa r) \kappa d\kappa, \quad (5.19a)$$

$$\theta_{1,2}(t, z = z_o, r) = e^{i\Omega t} \int_0^\infty T_{1,2}(z = z_o, \kappa) J_0(\kappa r) \kappa d\kappa, \quad (5.19b)$$

where  $J_0(\kappa r)$  is the zeroth order Bessel function of the first kind. In an FDTR experiment, an unmodulated probe beam measures the weighted average of the temperature distribution over its Gaussian-shaped beam (with a  $1/e^2$  radius  $r_{\text{spot,probe}}$ ). Mathematically, the weighted temperatures  $\bar{\theta}_{1,1}$  and  $\bar{\theta}_{1,2}$  are determined from [70]

$$\bar{\theta}_{1,1}(t, z = z_0) = \int_0^\infty \theta_{1,1}(t, z = z_0, r) \frac{4}{r_{\text{spot,probe}}^2} e^{-2r^2/r_{\text{spot,probe}}^2} 2\pi r dr, \quad (5.20a)$$

$$\bar{\theta}_{1,2}(t, z = z_0) = \int_0^\infty \theta_{1,2}(t, z = z_0, r) \frac{4}{r_{\text{spot,probe}}^2} e^{-2r^2/r_{\text{spot,probe}}^2} 2\pi r dr. \quad (5.20b)$$

Substituting Eqs. (5.19a) and (5.19b) into Eqs. (5.20a) and (5.20b) and rearranging yields a single integral over  $\kappa$ , which must be evaluated numerically

$$\bar{\theta}_{1,1}(t, z = z_0) = 2\pi e^{i\Omega t} \int_0^\infty T_{1,1}(z = z_0, \kappa) e^{-\kappa^2 r_{\text{spot,probe}}^2/8} \kappa d\kappa, \quad (5.21a)$$

$$\bar{\theta}_{1,2}(t, z = z_0) = 2\pi e^{i\Omega t} \int_0^\infty T_{1,2}(z = z_0, \kappa) e^{-\kappa^2 r_{\text{spot,probe}}^2/8} \kappa d\kappa. \quad (5.21b)$$

Equations (5.21a) and (5.21b) yield the temporal temperature change about the initial temperature of the solid at  $z = z_0$  weighted over the  $r$ -direction with a Gaussian-shaped weight function for each channel. Since the experiment returns only one temperature  $\theta_{\text{exp}}$ , it is important to know which temperature or combination of temperatures the probe contains. Thus, the experimental temperature response  $\theta_{\text{exp}}$  (namely the phase in FDTR experiments) is compared to a combination of the calculated temperature response for each channel  $a\bar{\theta}_{1,1} + b\bar{\theta}_{1,2}$  where  $a$  and  $b$  represent the portion of channel 1 and channel 2 temperatures in the measured temperature.

This solution can be extended to TDTR by using pulsed heating profiles for  $F_{0,1}$ ,  $F_{0,2}$ ,  $F_{n,1}$ , and  $F_{n,2}$  (i.e., multiply Eqs. (5.1c) and (5.1d) with a Dirac comb). A Fourier transform of the governing equations and boundary conditions is performed in lieu of separation of variables and the solution becomes a series solution. Handling the periodic sampling of the pulsed probe laser is discussed in Refs. [70] and [141]. Furthermore, volumetric heating can be simulated with this solution by creating multiple thin layers and choosing  $F_{0,1}$ ,  $F_{0,2}$ ,  $F_{n,1}$ , and  $F_{n,2}$  appropriately (discretization of the volumetric heating profile).

### III. Sensitivity analysis

A sensitivity analysis is performed to identify how sensitive the solution to the two-temperature model is to different input parameters  $\varepsilon$ . Based on prior convention the sensitivity  $S_\varepsilon$  is defined as the logarithmic derivative of the temperature phase response  $\phi$  with respect to a 1% change in one of the parameters  $\varepsilon$ ,  $S_\varepsilon = d\ln(\phi)/d\ln(\varepsilon)$  [94]. In my prior work, I used a gold/chromium transducer layer, where the chromium serves as an adhesion layer to increase the interface thermal conductance, therein increasing the sensitivity to the substrate thermal conductivity [73-75]. To simplify the sensitivity analysis yet still gain physical insight, I consider only a one layer metal transducer [layer 1 = transducer (tr)] deposited on a semi-infinite dielectric substrate [layer 2 = substrate (sub)].

Electron [channel 1 = electron (el)] and phonon [channel 2 = phonon (ph)] transport is modeled in the metal transducer layer and only phonon transport in the dielectric substrate (i.e.,  $k_{\text{sub,el}} = C_{\text{sub,el}} = 0$ ). Surface heating into only the electron channel of the transducer is assumed and that the phonon temperature of the transducer at the surface of the transducer is measured ( $H_{0,\text{el}} = 1 \text{ W}$ ,  $H_{0,\text{ph}} = H_{\text{tr,el}} = H_{\text{tr,ph}} = H_{\text{sub,el}} = H_{\text{sub,ph}} = 0$ ,  $a = 0$ ,  $b = 1$ , and  $z_o = 0$ ), which are assumptions typically made in thermoreflectance techniques [142]. It should be noted that the magnitudes of  $H_{0,1}$ ,  $H_{0,2}$ ,  $H_{n,1}$ , and  $H_{n,2}$  do not affect the phase of the temperature response but will affect the temperature amplitude. The fraction of the total heat deposited at each location is sufficient to predict the phase of the temperature response. Since the exact magnitudes of  $H_{0,1}$ ,  $H_{0,2}$ ,  $H_{n,1}$ , and  $H_{n,2}$  change from experiment to experiment and can be difficult to determine, only the phase of the temperature is reported.

All parameters  $\varepsilon$  and the nominal values of each parameter used to determine the temperature phase response are shown in Table 5.1. The interface thermal conductance  $G$  specified in the table is the conductance between the phonon channel in the transducer and the phonon channel in the substrate (i.e., the conductance between the electron channel in the transducer and the phonon channel in the substrate is neglected, although recent work has shown that electron-phonon interactions across a metal/nonmetal

interface are possible) [143]. The values indicated in Table 5.1 represent typical values from a real sample in an actual FDTR experiment with  $r_{\text{spot,probe}} = r_{\text{spot,pump}} = r_{\text{spot}}$  [73].

Table 5.1. Nominal values for the parameters used in the sensitivity analysis.

$\varepsilon$	Nominal Value
$C_{\text{tr,ph}}$ ( $\text{J m}^{-3} \text{K}^{-1}$ )	$2.4 \times 10^6$
$C_{\text{tr,el}}$ ( $\text{J m}^{-3} \text{K}^{-1}$ )	$2.1 \times 10^4$
$k_{\text{tr,ph}}$ ( $\text{W m}^{-1} \text{K}^{-1}$ )	3
$k_{\text{tr,el}}$ ( $\text{W m}^{-1} \text{K}^{-1}$ )	107
$g_{\text{tr}}$ ( $\text{W m}^{-3} \text{K}^{-1}$ )	$2.2 \times 10^{16}$
$t_{\text{tr}}$ (nm)	50
$C_{\text{sub,ph}}$ ( $\text{J m}^{-3} \text{K}^{-1}$ )	$1.65 \times 10^6$
$k_{\text{sub,ph}}$ ( $\text{W m}^{-1} \text{K}^{-1}$ )	130
$G$ ( $\text{MW m}^{-2} \text{K}^{-1}$ )	200
$r_{\text{spot}}$ ( $\mu\text{m}$ )	3.4

The nominal phase vs. heating frequency and result of the sensitivity analysis using the nominal values of  $\varepsilon$  from Table 5.1 are shown in Figs. 5.3(a) and 5.3(d). The phase vs. heating frequency and the sensitivity analysis using nominal values of  $\varepsilon$  with decreased  $G$  and decreased  $k_{\text{sub,ph}}$  are shown in Figs. 5.3(b) and 5.3(e) and Figs. 5.3(c) and 5.3(f). The solution to the two-temperature model is most sensitive to the spot size at low frequency, similar to the one-temperature model [74]. Large sensitivity to the substrate thermal conductivity is apparent in all cases and is important since it is necessary to be sensitive to fitting parameters over the entire measurement range of an FDTR measurement. The solution becomes particularly sensitive to the transducer thickness and phonon heat capacity at high frequency and is fairly insensitive to transducer electron and phonon thermal conductivities and electron heat capacity over all frequencies for all cases shown. In general, the solution is sensitive to the electron-phonon coupling parameter and interface thermal conductance at larger heating frequency.

I compare the sensitivity of  $\varepsilon$  from a two-temperature solution to a one-temperature solution. I define  $dS_\varepsilon = |S_\varepsilon(g_{\text{tr}} = 2.2 \times 10^{16})| - |S_\varepsilon(g_{\text{tr}} = \infty)|$ , where  $S_\varepsilon(g_{\text{tr}} = 2.2 \times 10^{16})$  is the sensitivity of  $\varepsilon$

when  $g_{\text{tr}} = 2.2 \times 10^{16} \text{ W m}^{-3} \text{ K}^{-1}$  [i.e., the sensitivity to the two-temperature model shown in Figs. 5.3(d)-(f)] and  $S_{\varepsilon}(g_{\text{tr}} = \infty)$  is the sensitivity of  $\varepsilon$  when  $g_{\text{tr}} = \infty$  (i.e., the sensitivity to the one-temperature model). When  $dS_{\varepsilon} = 0$ , there is no difference in the sensitivity of  $\varepsilon$  between a two-temperature and one-temperature solution. When  $dS_{\varepsilon} > 0$ , the two-temperature solution is more sensitive to  $\varepsilon$  and when  $dS_{\varepsilon} < 0$ , the one-temperature solution is more sensitive to  $\varepsilon$ . The parameter  $dS_{\varepsilon}$  for  $\varepsilon = t_{\text{tr}}, C_{\text{sub,ph}}, k_{\text{sub,ph}}, G$ , and  $r_{\text{spot}}$  is shown in Figs. 5.3(g)-(i). These  $\varepsilon$  are chosen since they are the most sensitive parameters from Figs. 5.3(d)-(f) and to make a fair comparison between the one- and two-temperature models (i.e., comparing bulk and individual channel transducer properties is irrelevant). The sharp changes in  $dS_{\varepsilon}$  result from  $S_{\varepsilon}$  crossing zero.

At low heating frequencies,  $dS_{\varepsilon} \approx 0$  for all  $\varepsilon$  for all cases. This result is expected and indicates that the two-temperature and one-temperature models predict the same temperature response since electron-phonon coupling timescales are much shorter than the timescale of heating. In general, sensitivities to the substrate thermal conductivity, interface thermal conductance, and transducer thickness are reduced in the two-temperature model due to the additional thermal resistance (i.e., resistance due to electron-phonon coupling). The solution of the two-temperature model is also less sensitive to the transducer thickness, but has similar sensitivity to spot size.

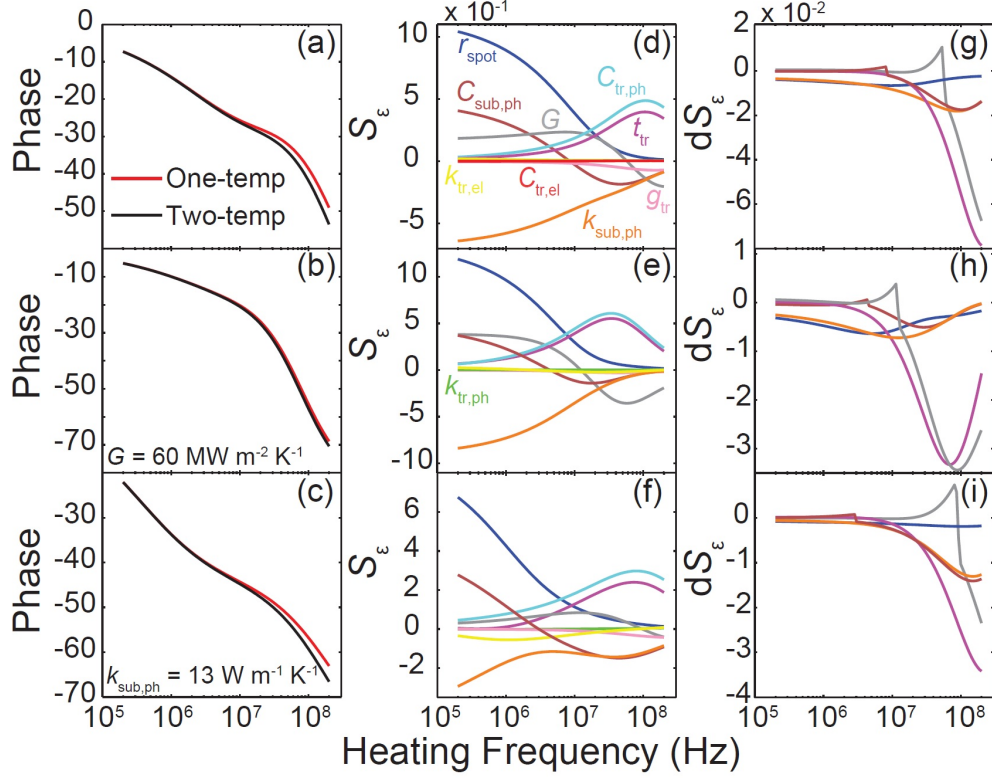


Fig. 5.3. Sensitivity analysis. The phase response from the one- and two-temperature solutions (a-c), the sensitivity analysis for the two-temperature solution (d-f), and the difference in the sensitivity of  $\epsilon$  between the two-temperature (when  $g_{\text{tr}} = 2.2 \times 10^{16} \text{ W m}^{-3} \text{ K}^{-1}$ ) and one-temperature (when  $g_{\text{tr}} = \infty$ ) solutions (g-i) using values of  $\epsilon$  from Table 5.1 (a,d,g), values of  $\epsilon$  from Table 5.1 with  $G = 60 \text{ MW m}^{-2} \text{ K}^{-1}$  (b,e,h), and values of  $\epsilon$  from Table 5.1 with  $k_{\text{sub,ph}} = 13 \text{ W m}^{-1} \text{ K}^{-1}$  (c,f,i).

Next, the effect of modeling a two-temperature system (i.e., a system where the electrons and phonons are out of equilibrium) with a one-temperature model is examined. First, the phase response as a function of heating frequency is generated with the two-temperature model. The phase data are divided into different windows and the phase data within each window are fit with a one-temperature model (i.e.,  $g_{\text{tr}} = \infty$ ) for the substrate thermal conductivity. This mimics the approach used in Refs. [73] and [75].

An important aspect of the result is how to determine the value of  $G$  used in the one-temperature model to fit the two-temperature data. Results for two cases are presented: (1) the value of  $G$  used in the one-temperature model is the same  $G$  used in the generation of the two-temperature phase data [Figs. 5.4(a) and 5.4(b)] and (2) the value of  $G$  used in the one-temperature model is found by fitting the high frequency two-temperature phase data [Figs. 5.4(c) and 5.4(d)]. The latter case is exactly the procedure

used in prior studies where a frequency independent  $G$  between the semiconductor substrate and adjacent metal layer was determined by fitting the high frequency phase data (15 data points in the  $\sim 100$  MHz range) due to increased sensitivity to  $G$  in this frequency range [73-75]. This procedure is analogous to the approach in TDTR, where the in-phase data related to high frequency components of the thermal decay ( $\sim 1$  GHz) are used to determine  $G$ , while the out-of-phase data related to the thermal response at  $f$  ( $\sim 10$  MHz) are used to determine  $k$ . The comparison of FDTR and TDTR is clarified by Collins et al., who examine TDTR in the frequency domain [77].

The fitted value of  $k_{\text{sub,ph}}$  normalized by the bulk thermal conductivity vs. heating frequency is shown in Fig. 5.4(a) for values of  $\varepsilon$  from Table 5.1 (base case), values of  $\varepsilon$  from Table 5.1 with  $G = 60$  MW m<sup>-2</sup> K<sup>-1</sup>, and values of  $\varepsilon$  from Table 5.1 with  $k_{\text{sub,ph}} = 13$  W m<sup>-1</sup> K<sup>-1</sup>. A similar procedure is performed with an increased transducer electron-phonon coupling parameter ( $g_{\text{tr}} = 22 \times 10^{16}$  W m<sup>-3</sup> K<sup>-1</sup>) as shown in Fig. 5.4(b). Here, the  $G$  used in the one-temperature model is the same value used to generate the two-temperature phase data for each parameter set (i.e., 200 MW m<sup>-2</sup> K<sup>-1</sup>, 60 MW m<sup>-2</sup> K<sup>-1</sup>, and 200 MW m<sup>-2</sup> K<sup>-1</sup>).

Interpreting two-temperature data with a one-temperature model results in a substrate thermal conductivity that shows added heating frequency dependence at higher heating frequencies. Furthermore, this heating frequency dependence becomes stronger with decreasing interface thermal conductance and increasing substrate thermal conductivity. Increasing the coupling between electrons and phonons delays the onset of heating frequency-dependent substrate thermal conductivity. I find from the two-temperature solution that the onset of electron-phonon non-equilibrium effects can be characterized with the non-dimensional time  $\tau_{\text{el-ph}} = \sqrt{2\pi f C_{\text{tr,ph}}/g_{\text{tr}}}$ . Upon closer inspection,  $\tau_{\text{el-ph}}$  is a comparison of two timescales: (1) the timescale of electron-phonon coupling in a diffusive system  $t_{\text{el-ph}} = C_{\text{tr,ph}}/g_{\text{tr}}$  and (2) the experimental timescale  $1/2\pi f$ .

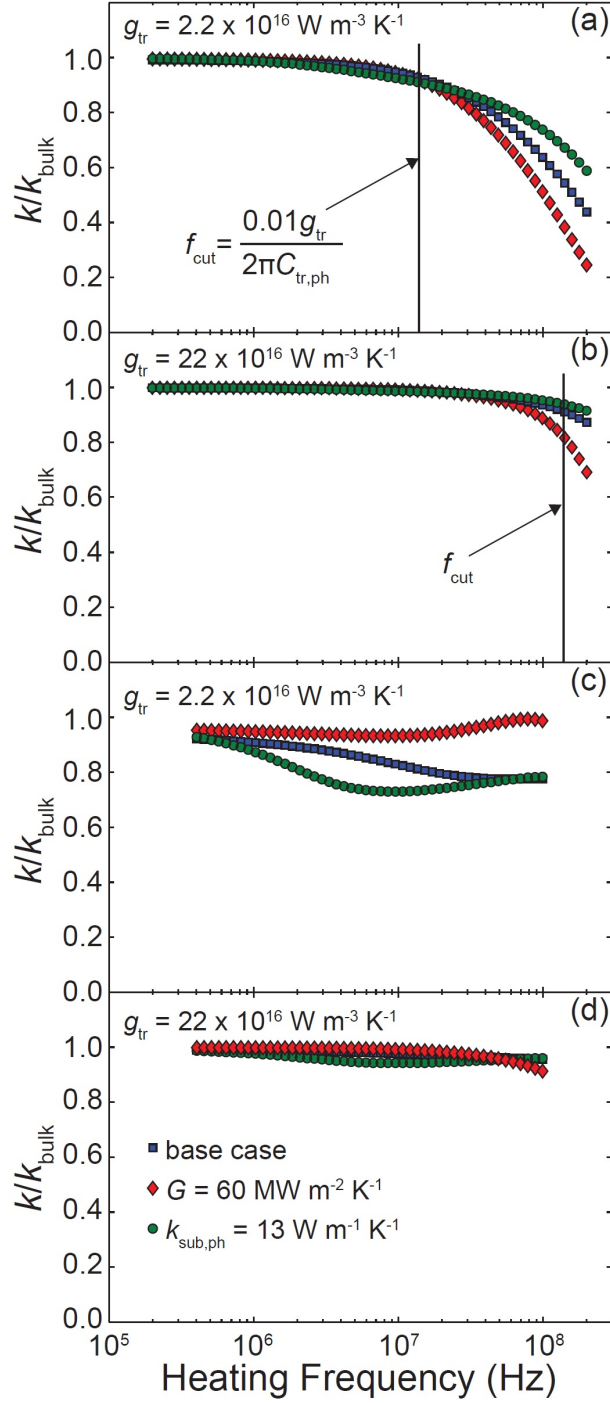


Fig. 5.4. Temperature phase response is generated using the two-temperature model with (a,c)  $g_{\text{tr}} = 2.2 \times 10^{16} \text{ W m}^{-3} \text{ K}^{-1}$  and (b,d)  $g_{\text{tr}} = 22 \times 10^{16} \text{ W m}^{-3} \text{ K}^{-1}$ . These phase data are then window fit with a solution to the one-temperature model ( $g_{\text{tr}} = \infty$ ) using the nominal value of  $G$  (a,b) and a value of  $G$  determined by fitting the high frequency phase data (c,d).

A shorter electron-phonon coupling timescale on the order of  $C_{\text{tr,el}}/g_{\text{tr}}$  has been previously defined, but I find the important electron-phonon coupling timescale to be on the order of  $C_{\text{tr,ph}}/g_{\text{tr}}$ ,

which is consistent with Refs. [108] and [144]. This longer timescale of electron-phonon coupling can also be derived using an analogy to the timescale for heat conduction. Assume  $t_{\text{el-ph}} = L_{\text{el-ph}}^2/D$  where  $D$  is the thermal diffusivity and  $L_{\text{el-ph}} = \sqrt{k_{\text{el}}/g}$  from Ref. [108]. The thermal diffusivity is a measure of a material's ability to conduct heat relative to its ability to store heat. In a metal, heat is mostly conducted by electrons and mostly stored by phonons, consequently  $D = k_{\text{tr,el}}/C_{\text{tr,ph}}$ . Substituting and simplifying yields the timescale for electron-phonon coupling processes as  $t_{\text{el-ph}} = C_{\text{tr,ph}}/g_{\text{tr}}$ .

When  $\tau_{\text{el-ph}} \ll 1$ , non-equilibrium effects between electrons and phonons in the transducer can be neglected. Consequently, I define the cutoff heating frequency as  $f_{\text{cut}} = 0.01g_{\text{tr}}/2\pi C_{\text{tr,ph}}$  (when  $\tau_{\text{el-ph}} = 0.1$ ). In an FDTR experiment with heating frequencies larger than  $f_{\text{cut}}$ , one should consider interpreting data with a two-temperature model. The cutoff heating frequency is indicated in Figs. 5.4(a) and 5.4(b) and consistently corresponds to an approximate 10% reduction in  $k_{\text{sub,ph}}$  when window fitting two-temperature phase data with a one-temperature model.

Next, two-temperature phase data are fit with the one-temperature model using a value of  $G$  determined from fitting the high frequency phase data. This procedure is exactly that used in prior studies [73-75]. The resulting  $k$  vs.  $f$  curves with  $g_{\text{tr}} = 2.2 \times 10^{16} \text{ W m}^{-3} \text{ K}^{-1}$  and  $g_{\text{tr}} = 22 \times 10^{16} \text{ W m}^{-3} \text{ K}^{-1}$ , shown in Figs. 5.4(c) and 5.4(d), exhibit reduced heating frequency dependence for all cases compared to the data shown in Figs. 5.4(a) and 5.4(b). When the electron-phonon coupling is weak ( $g_{\text{tr}} = 2.2 \times 10^{16} \text{ W m}^{-3} \text{ K}^{-1}$ ) the fitted values of  $G$  are  $160 \text{ W m}^{-2} \text{ K}^{-1}$ ,  $55 \text{ W m}^{-2} \text{ K}^{-1}$ , and  $135 \text{ W m}^{-2} \text{ K}^{-1}$  for the phase data generated using values of  $\epsilon$  from Table 5.1 (base case), values of  $\epsilon$  from Table 5.1 with  $G = 60 \text{ MW m}^{-2} \text{ K}^{-1}$ , and values of  $\epsilon$  from Table 5.1 with  $k_{\text{sub,ph}} = 13 \text{ W m}^{-1} \text{ K}^{-1}$ . These values of  $G$  are lower than the nominal values ( $200 \text{ W m}^{-2} \text{ K}^{-1}$ ,  $60 \text{ W m}^{-2} \text{ K}^{-1}$ , and  $200 \text{ W m}^{-2} \text{ K}^{-1}$ ). Alternatively, when the electron-phonon coupling is strong ( $g_{\text{tr}} = 22 \times 10^{16} \text{ W m}^{-3} \text{ K}^{-1}$ ) the fitted values of  $G$  are  $195 \text{ W m}^{-2} \text{ K}^{-1}$ ,  $60 \text{ W m}^{-2} \text{ K}^{-1}$ , and  $185 \text{ W m}^{-2} \text{ K}^{-1}$ , much closer to the nominal values.

One description of metal/dielectric interface transport is that the total interface thermal resistance (inverse of interface thermal conductance) is described as two resistances in series: (1) a resistance

associated with energy transfer between electrons and phonons in the metal at the interface and (2) a resistance associated with energy transfer between phonons in the metal and phonons in the dielectric across the interface [108,145]. Using a one-temperature model to determine the interface thermal resistance between a metal and dielectric lumps these two resistances together. The two-temperature model, however, inherently accounts for the electron-phonon coupling resistance. Thus, when the electron-phonon coupling resistance increases (reduced value of  $g_{tr}$ ), the total interface thermal resistance determined from the one-temperature model (by fitting high frequency phase data) will be larger (smaller interface thermal conductance) than that determined from the two-temperature model.

When  $G$  is not found from the high frequency phase data, the one-temperature model effectively accounts for the electron-phonon coupling resistance by reducing the thermal conductivity of the substrate [Figs. 5.4(a) and 5.4(b)]. As the coupling parameter increases, the electron-phonon resistance decreases, resulting in less heating frequency dependence of thermal conductivity over the frequency range shown. Fitting the high frequency data with the one-temperature model yields a larger interface thermal resistance and consequently less heating frequency dependence of thermal conductivity. Nonetheless, window fitting two-temperature data with a one-temperature model using  $G$  from the high frequency data (as was done in Refs. [73] and [75]) does yield some added heating frequency dependent thermal conductivity in systems with weak electron-phonon coupling [up to 30% for the cases shown in Fig. 5.4(c)].

#### IV. Fitting BB-FDTR data

In Refs. [73] and [75], phase data from BB-FDTR experiments were window fit with a solution to the one-temperature diffusion equation. A heating frequency-dependent thermal conductivity in silicon and other small unit cell semiconductors was found. The result was transformed into the thermal conductivity accumulation function  $k_{accum}$  that describes cumulative contributions to thermal conductivity from energy carriers with different MFPs. In those experiments, a gold/chromium transducer was deposited on the substrate, where the chromium served as an adhesion layer to increase the interface thermal conductance.

In the previous section, it was shown that electron-phonon non-equilibrium effects in a gold transducer are important at frequencies realized in BB-FDTR experiments and that fitting two-temperature data with a one-temperature model can lead to added heating frequency dependence to the thermal conductivity. Thus in this section, my goal is to develop a physically appropriate method to model the gold/chromium transducer used in BB-FDTR and refit silicon data from Ref. [73]. BB-FDTR measurements of SiO<sub>2</sub> and platinum (i.e., materials where a heating frequency-dependent thermal conductivity is not expected since energy carrier MFPs are much shorter than experimental length scales) from Ref. [73] are used to aid in consistent characterization of the gold/chromium transducer [146]. Heat transport in the SiO<sub>2</sub> and platinum samples is modeled with different sets of parameters: (i) a consistent set of parameters that best describes both the SiO<sub>2</sub> and platinum BB-FDTR phase data simultaneously (“consistent parameters”) and (ii) a set of parameters for SiO<sub>2</sub> and platinum samples that best describes BB-FDTR phase data for each sample individually (“best-fit parameters”). The “consistent parameters” are shown in Table 5.2.

The two-temperature model has many input parameters, many of which are well-known quantities and were determined either from the literature or measured in-house prior to fitting. Since phase data from Ref. [73] are used, identical parameters are used where appropriate (e.g.,  $r_{\text{spot}}$  and  $t_n$ ). For the data shown in this work,  $r_{\text{spot,pump}} = r_{\text{spot,probe}} = r_{\text{spot}}$  was measured using a knife-edge profiling technique, the transducer layer thicknesses were measured using x-ray reflectivity, and the thermal conductivity of the transducer was measured using a four-point resistivity measurement and the Wiedemann-Franz law  $k_{\text{WF}}$ . The electron thermal conductivity  $k_{\text{n,el}} = k_{\text{WF}} - k_{\text{n,ph}}$  where  $k_{\text{n,ph}}$  is from the literature. The same value of  $k_{\text{WF}}$  is used for each individual metal layer in the transducer since it was determined for the entire transducer layer. The heat capacities and electron phonon coupling constants are taken from the literature. The most difficult parameters to determine, and the only parameters that differ between the “consistent parameters” and the “best-fit parameters”, are the interface thermal conductances ( $G_{\text{n,el-el}}$ ,  $G_{\text{n,el-ph}}$ ,  $G_{\text{n,ph-el}}$ ,  $G_{\text{n,ph-ph}}$ ) for each interface, the ratio of electron and phonon temperatures

the probe laser is sensing ( $a$  and  $b$ ), where the heat is deposited ( $H_{n,1}$ ,  $H_{n,2}$ , and  $\delta_n$ ), and where the temperature is being sensed ( $z_0$ ).

For interface thermal conductances, only  $G_{n,el-el}$  and  $G_{n,ph-ph}$  are considered since coupling between different energy carriers across interfaces is weak [139]. For the gold/chromium interface values of  $4 \text{ GW m}^{-2} \text{ K}^{-1}$  and  $200 \text{ MW m}^{-2} \text{ K}^{-1}$  are used for the electron-electron and phonon-phonon interface thermal conductance as determined in Ref. [78]. For the metal-dielectric interface, only the phonon-phonon interaction across the interface is considered although it is possible that electrons in the metal will couple with phonons in the dielectric [143]. The high frequency phase data are fit to determine  $G_{n,ph-ph}$  between the metal and dielectric layer (chromium/SiO<sub>2</sub>, chromium/silicon, aluminum/silicon) and  $G_{n,el-el}$  between the chromium and platinum substrate, as was done in Refs. [74], [73], and [75].

The values of  $a$  and  $b$  are dependent on the material, the wavelength of the probe laser, and magnitude of the electron temperature excursion. For a 785 nm probe laser, as in TDTR,  $a/b \approx 0.02$  for gold (i.e., the change in reflectivity is mostly due to changes in the phonon temperature) [132]. It is expected that changes in reflectivity at 532 nm (probe wavelength in FDTR) are still mostly a result of changes in the phonon temperature. Gold, however, has an interband transition threshold of 2.4 eV, which may complicate the analysis of FDTR since the probe energy is less than this value and the pump energy is greater than this value [92]. Nonetheless, to be conservative values of  $a = 0$  and  $b = 1$  are used for all results presented in this chapter. It should be noted that  $a > 0$  results in more frequency dependence of  $k$  because electrons are hotter, which translates into greater  $k$  suppression. The determination of wavelength-dependent values of  $a$  and  $b$  for continuous wave heating would be a useful complement to two-temperature analysis, though beyond the scope of my work.

Table 5.2. Room temperature values of “consistent parameters” used in the modeling/fitting of data for each sample measured. Italicized parameters are the transducer parameters that differ between “consistent parameters” and “best-fit parameters” for SiO<sub>2</sub> and platinum.

	n = [Au, Cr, SiO <sub>2</sub> , Si] <sup>§</sup>	n = [Au, Cr, Pt] <sup>§</sup>	n = [Au, Cr, Si] <sup>§</sup>	n = [Au, Cr, Al, Si]
$C_{n,ph}$ (MJ m <sup>-3</sup> K <sup>-1</sup> )	[2.4, <sup>a</sup> 3.2, <sup>a</sup> 1.65, <sup>a</sup> 1.65 <sup>a</sup> ]	[2.4, <sup>a</sup> 3.2, <sup>a</sup> 2.8 <sup>a</sup> ]	[2.4, <sup>a</sup> 3.2, <sup>a</sup> 1.65 <sup>a</sup> ]	[2.4, <sup>a</sup> 3.2, <sup>a</sup> 2.4, <sup>a</sup> 1.65 <sup>a</sup> ]
$C_{n,el}$ (kJ m <sup>-3</sup> K <sup>-1</sup> )	[21, <sup>b</sup> 58, <sup>b</sup> n/a, n/a]	[21, <sup>b</sup> 58, <sup>b</sup> 224 <sup>b</sup> ]	[21, <sup>b</sup> 58, <sup>b</sup> n/a]	[21, <sup>b</sup> 58, <sup>b</sup> 40, <sup>b</sup> n/a]
$k_{n,ph}$ (W m <sup>-1</sup> K <sup>-1</sup> )	[3, <sup>c</sup> 20, <sup>d</sup> 1.45, <sup>a</sup> 145 <sup>a</sup> ]	[3, <sup>c</sup> 20, <sup>d</sup> 7 <sup>e</sup> ]	[3, <sup>c</sup> 20, <sup>d</sup> fit]	[3, <sup>c</sup> 20, <sup>d</sup> 5, <sup>e</sup> fit]
$k_{n,el}$ (W m <sup>-1</sup> K <sup>-1</sup> )	[127, <sup>f</sup> 110, <sup>f</sup> n/a, n/a]	[115, <sup>f</sup> 110, <sup>f</sup> 65 <sup>g</sup> ]	[107, <sup>f</sup> 110, <sup>f</sup> n/a]	[87, <sup>h</sup> 70, <sup>h</sup> 85, <sup>h</sup> n/a]
$g_n$ (×10 <sup>16</sup> W m <sup>-3</sup> K <sup>-1</sup> )	[2.2, <sup>i</sup> 42, <sup>j</sup> n/a, n/a]	[2.2, <sup>i</sup> 42, <sup>j</sup> 109 <sup>k</sup> ]	[2.2, <sup>i</sup> 42, <sup>j</sup> n/a]	[2.2, <sup>i</sup> 42, <sup>j</sup> 25, <sup>l</sup> n/a]
$t_n$ (nm)	[53, <sup>m</sup> 8, <sup>m</sup> 1000, <sup>m</sup> 5×10 <sup>5</sup> ]	[55, <sup>m</sup> 7, <sup>m</sup> 5×10 <sup>5</sup> ]	[54, <sup>m</sup> 8, <sup>m</sup> 5×10 <sup>5</sup> ]	[55, 8, 40, 5×10 <sup>5</sup> ]
$\eta_{n,ph}$	[1, 1, 1, 1]	[1, 1, 1]	[1, 1, 1]	[1, 1, 1, 1]
$\eta_{n,el}$	[1, 1, 1, 1]	[1, 1, 1]	[1, 1, 1]	[1, 1, 1, 1]
$G_{n,el-el}$ (MW m <sup>-2</sup> K <sup>-1</sup> )	[4000, <sup>n</sup> n/a, n/a]	[4000, <sup>n</sup> 610 <sup>o</sup> ]	[4000, <sup>n</sup> n/a]	[4000, <sup>n</sup> 4000 <sup>n</sup> , n/a]
$G_{n,el-ph}$ (MW m <sup>-2</sup> K <sup>-1</sup> )	[0, <sup>p</sup> 0, <sup>p</sup> n/a]	[0, <sup>p</sup> 0 <sup>p</sup> ]	[0, <sup>p</sup> 0 <sup>p</sup> ]	[0, <sup>p</sup> 0, <sup>p</sup> 0 <sup>p</sup> ]
$G_{n,ph-el}$ (MW m <sup>-2</sup> K <sup>-1</sup> )	[0, <sup>p</sup> n/a, n/a]	[0, <sup>p</sup> 0 <sup>p</sup> ]	[0, <sup>p</sup> n/a]	[0, <sup>p</sup> 0, <sup>p</sup> n/a]
$G_{n,ph-ph}$ (MW m <sup>-2</sup> K <sup>-1</sup> )	[200, <sup>n</sup> 135, <sup>o</sup> ∞]	[200, <sup>n</sup> 200 <sup>n</sup> ]	[200, <sup>n</sup> 275 <sup>o</sup> ]	[200, <sup>n</sup> 200 <sup>n</sup> , 280 <sup>o</sup> ]
$H_{n,ph}$ (W)	[0, 0, 0, 0]	[0, 0, 0]	[0, 0, 0]	[0, 0, 0, 0]
$H_{n,el}$ (W)	[0.3, 0.7, 0, 0]	[0.3, 0.7, 0]	[0.3, 0.7, 0]	[0.3, 0.7, 0, 0]
$\delta_n$ (nm)	[53, 4, n/a, n/a]	[55, 3.5, n/a]	[54, 4, n/a]	[55, 4, n/a, n/a]
$H_{0,ph}$ (W)	0	0	0	0
$H_{0,el}$ (W)	0	0	0	0
$z_o$ (nm)	40	40	40	40
$a$	0	0	0	0
$b$	1	1	1	1
$r_{spot}$ (μm)	3.4 <sup>m</sup>	2.6 <sup>m</sup>	3.4 <sup>m</sup>	2.3

<sup>§</sup>phase data taken directly from Ref. [73]

<sup>a</sup>Ref. [120]

<sup>b</sup>Ref. [147]

<sup>c</sup>Ref. [148]

<sup>d</sup>Ref. [149]

<sup>e</sup>Ref. [150]

<sup>f</sup>Determined by subtracting  $k_{n,ph}$  from  $k_{WF}$  from Ref. [73]

<sup>g</sup>Determined by subtracting  $k_{n,ph}$  from  $k_{bulk}$  from Ref. [120]

<sup>h</sup>Determined by subtracting  $k_{n,ph}$  from  $k_{WF} = 90$  W m<sup>-1</sup> K<sup>-1</sup>

<sup>i</sup>Ref. [132]

<sup>j</sup>Ref. [151]

<sup>k</sup>Ref. [152]

<sup>l</sup>Ref. [133]

<sup>m</sup>Ref. [73]

<sup>n</sup>Ref. [78]

<sup>o</sup>Determined by fitting high frequency phase data

<sup>P</sup>Ref. [139]

Typically in TDTR and FDTR it is assumed that heat is deposited at the sample surface. The incident pump light couples with the electrons in the metal transducer [142]. In a metal with an infinite electron-phonon coupling parameter, the electrons couple and equilibrate with the phonons instantaneously (i.e., a one-temperature system). In a metal with a finite/low electron-phonon coupling parameter, ballistic motion of electrons excited by the incident pump photons within an optical penetration depth (22 nm for 488 nm pump light in gold) effectively deposit their heat further into the metal (approximately 100 nm in gold at room temperature) [153]. I can account for the initial nondiffusive electron transport with this model by depositing heat at different locations in the transducer.

Ballistic motion of excited gold electrons across the thin gold transducer layer results in most of the heat being effectively deposited into the gold electrons at the gold/chromium interface or in the chromium electrons [78,132]. I find that depositing 30% of the heat into the gold electrons at the gold/chromium interface and 70% of the heat into the chromium electrons yields the best fit for the SiO<sub>2</sub> and platinum samples with a gold/chromium bilayer transducer. The values  $H_{Au,el} = 0.3$  and  $H_{Cr,el} = 0.7$  best describe both the SiO<sub>2</sub> and platinum samples (i.e., these values are identical in both the “best-fit parameters” and “consistent parameters”).

Typically in TDTR and FDTR it is assumed that the probe laser senses the change in reflectivity due to the change in phonon temperature at the sample surface ( $z_o = 0$ ) [142]. I find, however, that the two-temperature model best describes the SiO<sub>2</sub> phase data when  $z_o = 53$  nm (i.e., at the gold/chromium interface) and the platinum data when  $z_o = 20$  nm (i.e., one optical penetration depth of 532 nm probe light in gold). The value of  $z_o$  is the only user-defined parameter that varies between the “best-fit parameters” and “consistent parameters”. Using the best-fit values of  $z_o$  yields  $G_{Cr-SiO_2,ph-ph} = 100$  MW m<sup>-2</sup> K<sup>-1</sup> and  $G_{Cr-Pt,el-el} = 500$  MW m<sup>-2</sup> K<sup>-1</sup> when fitting the high frequency phase data. The value of  $z_o$  that best describes the SiO<sub>2</sub> and platinum phase data simultaneously is  $z_o = 40$  nm (corresponding to two optical penetration depths of the probe light in gold). The values of  $G_{Cr-SiO_2,ph-ph}$  and  $G_{Cr-Pt,el-el}$

determined by fitting the high frequency phase data with the consistent value of  $z_0$  are shown in Table 5.2. It should be noted that the fitted electron-electron interface thermal conductance between the chromium and platinum is lower than expected. Using an interface thermal conductance on the order of  $1 \text{ GW m}^{-2} \text{ K}^{-1}$  is too large to accurately describe the measured data. The low electron-electron interface thermal conductance may result from oxidation of the chromium or an intermixed interfacial layer [154] and is unique to the platinum sample. Notably, other parameters cannot compensate for this low  $G$  value in the fit, and hence it is only a feature of the platinum sample and does not influence other conclusions.

The phase data measured with BB-FDTR for  $\text{SiO}_2$  and platinum at room temperature are shown in Fig. 5.5(a) along with the phase predictions from the two-temperature model using the “consistent parameters” (shown in Table 5.2) and the “best-fit parameters”. The goodness of the fits is quantified using the mean squared error (MSE). For the “best-fit parameters”  $\text{MSE} = 1.37$  for  $\text{SiO}_2$  and  $\text{MSE} = 0.16$  for platinum. At intermediate and high frequencies in  $\text{SiO}_2$ , the two-temperature predictions and BB-FDTR data differ by about 1 degree of phase. Changing the transducer thickness by less than 10% remedies this difference quite well, however, the transducer thickness is set to be consistent with what was measured in Ref. [73]. Overall, the two-temperature model with “consistent parameters” describes the BB-FDTR measurements with a low mean squared error ( $\text{MSE} = 2.80$  for  $\text{SiO}_2$  and  $\text{MSE} = 0.29$  for platinum). Also shown is the two-temperature phase predictions for  $\text{SiO}_2$  and platinum using the transducer parameters from Ref. [78] where all the heat is deposited in the chromium electrons ( $H_{\text{Cr,el}} = 1$ ), the phonon temperature is measured at  $z_0 = 26 \text{ nm}$ , a reduced thermal conductivity of the chromium electron channel is used ( $k_{\text{Cr,el}} = 20 \text{ W m}^{-1} \text{ K}^{-1}$ ), and the electron-phonon coupling parameter of the chromium  $g_{\text{Cr}} = \infty$ . Fitting the high frequency data with the parameters from Ref. [78] yields  $G_{\text{Cr-SiO}_2, \text{ph-ph}} = 130 \text{ MW m}^{-2} \text{ K}^{-1}$  and  $G_{\text{Cr-Pt,el-el}} = 400 \text{ MW m}^{-2} \text{ K}^{-1}$ . These parameters are not as effective at describing the measurements as the set of “consistent parameters” ( $\text{MSE} = 5.64$  for  $\text{SiO}_2$  and  $\text{MSE} = 0.45$  for platinum).

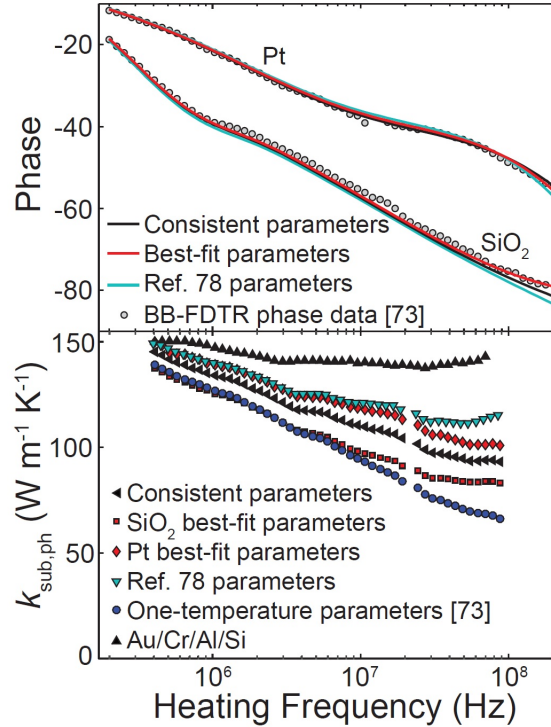


Fig. 5.5. (a) BB-FDTR phase data for  $\text{SiO}_2$  and platinum from Ref. [73] modeled with the two-temperature model using parameters from Ref. [78], parameters that are consistent between each sample (“consistent parameters” shown in Table 5.2), and parameters for each sample that result in the best fit (“best-fit parameters”). (b) BB-FDTR phase data for silicon at  $T = 300$  K from Ref. [73] are window fit using the transducer parameters from (a). BB-FDTR phase data for a gold/chromium/aluminum/silicon sample are measured and fit with the two-temperature model. The thermal conductivity is independent of heating frequency compared to the gold/chromium/silicon sample.

Next, BB-FDTR silicon data at room temperature from Ref. [73] are window fit with the two-temperature model for the silicon thermal conductivity. The results of fitting are compared with the “consistent parameters” (shown in Table 5.2), the “best-fit parameters” for  $\text{SiO}_2$ , the “best-fit parameters” for platinum, the parameters used in Ref. [78], and the one-temperature parameters used in Ref. [73] in Fig. 5.5(b). The interface thermal conductance for each data set (excluding the parameters used in Ref. [78]) was determined by fitting the high frequency phase data. It is clear that using the two-temperature model to fit BB-FDTR phase data diminishes the observed heating frequency dependence compared to window fitting with a one-temperature model. The thermal conductivity, however, is still a strong function of heating frequency. In particular, fitting with the two-temperature model using “consistent parameters” yields a thermal conductivity that reduces by over 30% from  $f = 200$  kHz to 200 MHz,

suggestive of nondiffusive phonon transport in the silicon substrate. Even fitting with the parameters from Ref. [78] results in heating frequency-dependent behavior of the thermal conductivity.

The  $k$  vs.  $f$  data for a gold/chromium/silicon sample, which results from fitting phase data with the two-temperature model, suggest that electron-phonon coupling in the gold layer is not solely responsible for the observed heating frequency-dependent thermal conductivity seen in FDTR experiments, as was proposed in Ref. [78]. Another factor that could result in the discrepancy between FDTR and TDTR  $k$  vs.  $f$  data for silicon is the interface between the metal transducer and the silicon substrate (i.e., in FDTR the interface is chromium/silicon and in TDTR the interface is aluminum/silicon). The different metal/dielectric interfaces may selectively excite different phonon modes in the dielectric substrate resulting in different nondiffusive effects and thus observation of different  $k$  vs.  $f$  behavior [83,131].

To explore this effect, I created and measured a gold/chromium/aluminum/silicon sample and performed BB-FDTR experiments. A similar thickness of gold and chromium was deposited to maintain the same heating as determined from the SiO<sub>2</sub> and platinum samples. These data are window fit with the two-temperature model using the parameters shown in Table 5.2 and the “consistent parameters” for the gold/chromium layers, as shown in Fig. 5.5(b). These data are within  $\pm 15\%$  over the entire frequency range assuming 5% changes in the total transducer layer thickness, spot size, and  $G_{\text{Al-Si,ph-ph}}$ . Values of  $G_{\text{Cr-Al,el-el}} = 4 \text{ GW m}^{-2} \text{ K}^{-1}$  and  $G_{\text{Cr-Al,ph-ph}} = 200 \text{ MW m}^{-2} \text{ K}^{-1}$  are assumed (i.e., the same values determined for the gold/chromium interface in Ref. [78]). The result indicates the thermal conductivity has a limited dependence on heating frequency, suggesting that the metal dielectric interface plays a large role in the observed heating frequency-dependence of the dielectric substrate [83,131]. The role of the interface in heating frequency-dependent measurements of thermal conductivity is an exciting topic to study further.

## V. Summary

I formulated a multi-layer, two-temperature model geometrically similar to thermoreflectance experiments. The model incorporates additional functionality over existing models by allowing heat input at any location in any layer, which can be used to effectively model nondiffusive electron transport in metals with a low electron-phonon coupling parameter. A thorough sensitivity analysis of the solution was performed to identify sensitive parameters and showed that interpreting two-temperature phase data with a one-temperature model results in added heating frequency dependence to the thermal conductivity. Additionally, a cutoff frequency for FDTR experiments was identified, above which electron-phonon coupling effects become important.

The work in Ref. [78] recognized that electron-phonon coupling in the gold transducer layer of BB-FDTR experiments must be considered in the analysis of the data. The two-temperature model developed in this chapter addresses these important modifications to the analysis of BB-FDTR experiments, but also adds some ambiguity due to the number of parameters that must be defined. Many of these parameters can be difficult to determine, specifically all four interface thermal conductances at each interface, where the heat is deposited, where the temperature is measured, and what portion of the electron and phonon temperatures are being measured. I attempted to establish a set of physically consistent parameters for the gold/chromium transducer layer used in BB-FDTR experiments by fitting SiO<sub>2</sub> and platinum phase data, where the thermal conductivity should be heating frequency-independent. Using these parameters to window fit silicon data diminishes the heating frequency dependence of the silicon thermal conductivity, but does not eliminate it. Additional experiments on a gold/chromium/aluminum/silicon sample showed a thermal conductivity with limited heating frequency dependence, suggesting that the interface between the transducer and substrate affects the observed heating frequency dependence.

## 6. APPLYING THE BOLTZMANN TRANSPORT EQUATION TO RRAM

### I. Overview

Resistive-switching memory (RRAM) offers benefits to nonvolatile memory systems due to scalability, fast switching, and easy fabrication [155]. In RRAM, electrical stimulation switches the resistance of a metal-insulator-metal memory cell. A low-resistance state is achieved during the set process, when a conductive filament (CF) is formed by dielectric breakdown. During the reset process, disruption of the CF restores the device to a high-resistance state.

The effect of temperature on switching processes in RRAM is hitherto studied assuming diffusive thermal transport [156-169], but I herein show that nondiffusive mechanisms have critical implications to device operation and active physical interpretations. Nondiffusive thermal transport is particularly important since switching is thought to be temperature driven. Studies suggest that dissolution of the CF during the reset process occurs when the CF reaches a critical temperature due to Joule heating [156,159,170]. Hence, the rate of heat removal from the CF dictates the reset voltage [159].

Modeling thermal transport within the CF and surrounding oxide with the cylindrical heat diffusion equation with bulk thermal properties is appropriate when the geometrical length scales in the system are much larger than thermal energy carrier MFPs [17,21,39]. The validity of this requirement is checked by comparing the radius  $r_o$  of the CF to the gray phonon MFP  $\Lambda_g$  (i.e., phonon frequency-independent) in the insulator. Measurements suggest that the radius of the CF ranges from 1 nm to 20 nm [171]. The gray phonon MFP is defined by kinetic theory as  $\Lambda_g = 3k_{\text{bulk}}/v_s C$ , where  $k_{\text{bulk}}$  is the bulk thermal conductivity,  $v_s$  is the average sound speed, and  $C$  is the total volumetric heat capacity. For rutile  $\text{TiO}_2$ , a prototypical RRAM material,  $\Lambda_g = 1.3$  nm at a temperature  $T = 300$  K [120,172]. With this gray approximation, the heat diffusion equation is invalid only for the smallest CF radii in RRAM. It is well known, however, that phonons in crystals do not have a single, gray MFP but instead a broad range of MFPs, where those larger than  $\Lambda_g$  dominate thermal conductivity [19,45,48,73,75].

In this chapter, I use existing thermal conductivity data to approximate the phonon MFP spectrum in TiO<sub>2</sub> and show that phonons with MFPs comparable to the CF radii contribute significantly to thermal conductivity, rendering the diffusion equation inadequate. Accordingly, I develop an analytical solution to the BTE to predict thermal transport when CF radii are comparable to energy carrier MFPs [17,21,83,173]. The BTE predicts CF temperatures that are higher than predictions by the heat diffusion equation (e.g., 5× higher for a 1 nm CF radius in a device at a temperature of 300 K). Modeling thermal transport with the diffusion equation and a suppressed value of insulator thermal conductivity is, however, a reasonable substitute in device models that cannot invoke the BTE. This work is under review at *IEEE Electron Device Letters* with contributions from co-author J. A. Malen [174].

## II. Phonon mean free path spectrum in TiO<sub>2</sub>

To determine the phonon MFP spectrum of crystalline TiO<sub>2</sub> in the rutile structure I follow the procedure outlined in Ref. [75]. Bulk thermal conductivity data as a function of temperature from Ref. [175] are shown in Fig. 6.1(a) and are fit with the Born-von Karman-Slack model [38], which assumes Born-von Karman dispersion (neglecting optical modes) with an average sound velocity  $v_s = 6650$  m/s [172] and MFP of the form  $\Lambda = v_g(A\omega^4 + P\omega^2Te^{-C_U/T} + v_g/b)^{-1}$ , for the scattering coefficients  $A$  (impurity),  $P$  (Umklapp),  $C_U$  (Umklapp), and  $b$  (boundary). Here,  $\omega$  is phonon frequency and  $v_g(\omega)$  is the phonon group velocity. The number density of primitive unit cells is used in specifying the wavevector cutoff in the Born-von Karman dispersion. The best fit to the data yields  $A = 5 \times 10^{-43} \text{ s}^3$ ,  $P = 1.16 \times 10^{-18} \text{ sK}^{-1}$ ,  $C_U = 77 \text{ K}$ , and  $b = 1 \text{ cm}$  and is shown in Fig. 6.1(a). The values  $b$  is insensitive in the fit since there are no experimental points in a strong boundary scattering regime and is thus chosen to represent a bulk sample.

Next,  $\Lambda(\omega)$  is used to determine the thermal conductivity accumulation function [38]

$$k_{\text{accum}}(\Lambda^*) = \int_0^{\Lambda^*} k_{\Lambda} d\Lambda = \int_0^{\Lambda^*} \frac{1}{3} C_{\Lambda}(\Lambda) v_g(\Lambda) \Lambda d\Lambda \quad , \quad (6.1)$$

which quantifies the cumulative contributions to thermal conductivity from phonons with MFPs between 0 and  $\Lambda^*$  and is shown in Fig. 6.1(b) for temperatures of 300 and 500 K. Here,  $k_\Lambda$  and  $C_\Lambda$  are the thermal conductivity and volumetric heat capacity per unit  $\Lambda$ . For rutile,  $k_{\text{accum}}$  indicates that thermal conductivity at these temperatures is dominated by phonons with MFPs between 1 and 1000 nm. Since these MFPs are comparable to CF radii in RRAM, using the heat diffusion equation is not justified.

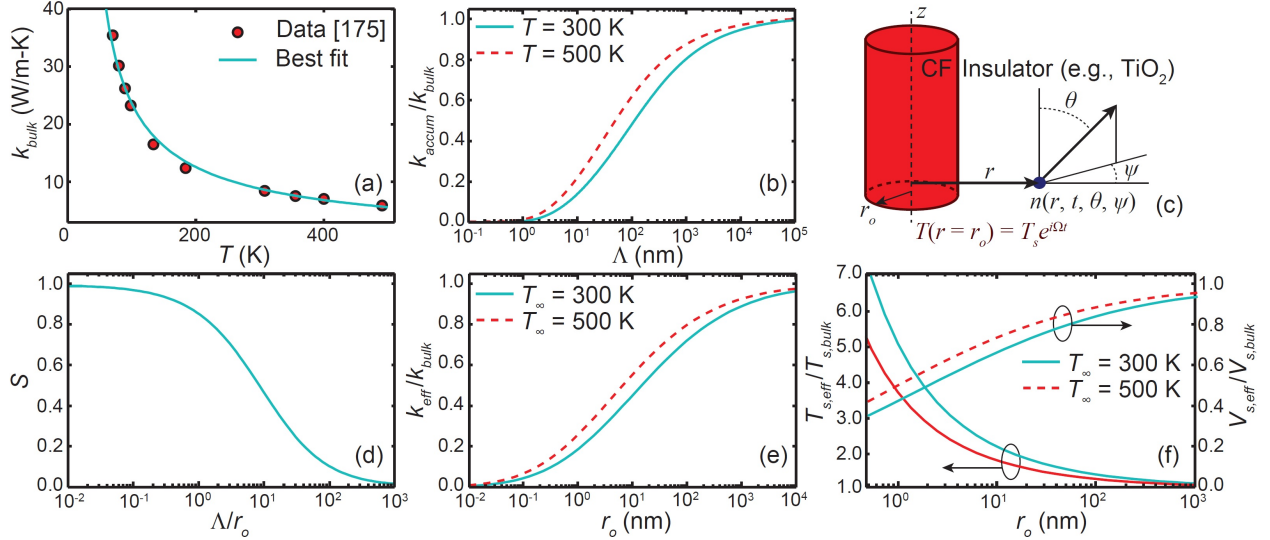


Fig. 6.1. (a)  $k_{\text{bulk}}$  vs.  $T$  data are fit with the Born-von Karman-Slack model to find  $\Lambda(\omega)$ . (b)  $k_{\text{accum}}/k_{\text{bulk}}$  at  $T = 300$  and  $500$  K from Eq. (6.1) using the result from (a). (c) RRAM geometry is approximated as an infinite cylinder in a semi-infinite insulator. The BTE is solved for the non-equilibrium phonon distribution function in the insulator with temporally periodic surface heating. (d)  $S$  determined from Eq. (6.5). (e)  $k_{\text{eff}}$  vs. CF radius for  $\text{TiO}_2$  at  $T_\infty = 300$  and  $500$  K due to nondiffusive effects found using  $k_{\text{accum}}$  [from (b)] and  $S$  [from (d)]. (f) Change in surface temperature and reset voltage of a CF in  $\text{TiO}_2$  when accounting for nondiffusive effects.

### III. Analytical solution to the Boltzmann transport equation

Nondiffusive thermal transport has been modeled analytically in spherical systems with the BTE (see Chapter 4) [17,83]. Here, I develop an approximate analytical solution to the cylindrical BTE for RRAM by approximating the geometry of one CF as an infinitely long cylinder with radius  $r_o$  embedded in an insulator (e.g.,  $\text{TiO}_2$ ), as illustrated in Fig. 6.1(c). Periodic surface heating of the CF is imposed  $T(r = r_o) = T_s e^{i\Omega t}$  where  $\Omega$  and  $T_s$  are the angular frequency and amplitude of the temporal oscillations. This boundary condition relates to periodic operation such as switching of an RRAM device from the set to

reset states. This case is interesting because periodic heating induces additional length scales (i.e., thermal penetration depth) into the system. In this study, I set  $\Omega = 6.3 \times 10^8$  rad/s, corresponding to a switching time of 10 ns.

I solve for the non-equilibrium phonon distribution function  $n$  in the insulator using the 1-D, gray BTE in cylindrical coordinates under the relaxation time approximation in an isotropic medium [39,118]

$$\frac{1}{v_s} \frac{\partial n}{\partial t} + \sin\theta \cos\psi \frac{\partial n}{\partial r} - \frac{\sin\theta \sin\psi}{r} \frac{\partial n}{\partial \psi} = \frac{n_e - n}{\Lambda} \quad , \quad (6.2)$$

where  $\theta$  is the polar angle and accounts for the velocity of phonons traveling at an angle  $\theta$  from the  $z$ -direction,  $\psi$  is the azimuthal angle,  $n(r, t, \theta, \psi)$  is the phonon energy density per unit phonon frequency per unit solid angle and equals  $\hbar\omega D(\omega)g(r, t, \theta, \psi)/4\pi$  where  $\hbar$  is the reduced Planck constant,  $D(\omega)$  is the phonon density of states, and  $g(r, t, \theta, \psi)$  is the occupation function. The equilibrium distribution function  $n_e(r, t)$  is specified for phonons when  $g$  is the Bose-Einstein distribution  $g_{\text{BE}}$ . For small temperature variations,  $n_e(r, t) \approx C_\omega T(r, t)/4\pi$  where  $C_\omega$  is the differential,  $\omega$ -dependent specific heat and  $T(r, t)$  is the deviation from  $T(r \rightarrow \infty, t)$  taken here to be zero for convenience ( $T_\infty = 0$ ) [79].

The difficulty in solving Eq. (6.2) for  $n$  comes from its polar and azimuthal angular dependence. The governing equation is simplified to determine analytical solutions by using the method of spherical harmonics (the  $P_N$  approximation), which reduces Eq. (6.2) into a set of  $N$  simpler partial differential equations by taking advantage of the orthogonality of spherical harmonics [118]. Due to the temporally periodic nature of the problem, separation of variables is performed such that  $n(r, t, \theta, \psi) = \bar{n}(r, \theta, \psi)e^{i\Omega t}$ . The  $P_1$  approximation yields

$$\frac{d\bar{n}_2}{dr} + \frac{\bar{n}_2}{r} + \frac{i\Omega}{v_s} \bar{n}_0 = 0 \quad , \quad (6.3a)$$

$$\frac{1}{3} \frac{d\bar{n}_0}{dr} + \bar{n}_2 \left( \frac{i\Omega}{v_s} + \frac{1}{\Lambda} \right) = 0 \quad . \quad (6.3b)$$

Here,  $\bar{n}_0$  and  $\bar{n}_2$  are the zeroth and second moments of  $\bar{n}$  and are proportional to the temperature and heat flux profiles,  $\bar{T}_{\text{BTE}}(r)$  and  $\bar{q}''_{\text{BTE}}(r)$ . They are determined with boundary conditions (i) as  $r \rightarrow \infty$

the temperature decays to  $T_\infty$  and (ii) at  $r = r_0$  the total energy carried by phonons traveling in the positive  $r$ -direction is equal to the sum of the energy carried by phonons emitted (with probability of emission  $\varepsilon$ ) and the energy carried by phonons traveling in the negative  $r$ -direction that are reflected from the surface (with probability of reflection  $\rho$ ) [17,83]. The resulting spatial temperature and heat flux profiles predicted by the BTE are

$$\bar{T}_{\text{BTE}}(r) = \frac{\int_0^\infty \bar{n}_0 d\omega}{\int_0^\infty C_\omega d\omega} = v_s \beta \varepsilon T_s K_0(\beta r) / \Gamma \quad , \quad (6.4a)$$

$$\bar{q}''_{\text{BTE}}(r) = \int_0^\infty v_s \bar{n}_2 d\omega = i\Omega C v_s \varepsilon T_s K_1(\beta r) / \Gamma \quad , \quad (6.4b)$$

where  $\Gamma = v_s \beta K_0(\beta r_0)(1 - \rho) + 2i\Omega K_1(\beta r_0)(1 + \rho)$ ,  $K_0$  and  $K_1$  are the modified Bessel functions of the second kind of order 0 and 1, and  $\beta = \sqrt{3\Omega(i v_s - \Omega\Lambda) / (v_s^2 \Lambda)}$ . Since  $\bar{n}_0$  and  $\bar{n}_2$  are independent of  $\omega$ , the integral over  $\omega$  only changes  $C_\omega$  to the total volumetric heat capacity  $C$ . For a more thorough derivation, see Ref. [83] (or Chapter 4), which is an analogous derivation in spherical coordinates.

#### IV. Effective thermal conductivity in RRAM

I define the thermal resistance of the system as  $R = (T_s - T_\infty) / \bar{q}''(r = r_0)$ , where  $R_{\text{diff}}$  and  $R_{\text{BTE}}$  are the thermal resistances from the diffusion equation and BTE. The thermal conductivity suppression function  $S(\Lambda, r_0, \Omega) = k_{1\text{-app}} / k_{\text{bulk}}$  is determined by finding the apparent thermal conductivity of a single phonon mode  $k_{1\text{-app}}$  that equates  $R_{\text{diff}}$  to  $R_{\text{BTE}}$ . The suppression function is material-independent and found from

$$\sqrt{\frac{k_{1\text{-app}}}{i\Omega C}} K_1\left(\sqrt{\frac{i\Omega C}{k_{1\text{-app}}}} r_0\right) / K_0\left(\sqrt{\frac{i\Omega C}{k_{1\text{-app}}}} r_0\right) = v_s \varepsilon K_1(\beta r_0) / \Gamma \quad , \quad (6.5)$$

where  $k_{1\text{-app}}$  is solved for numerically since it appears in the argument of  $K_0$  and  $K_1$ . The resulting  $S$  is shown in Fig. 6.1(d) for  $\Omega = 6.3 \times 10^8$  rad/s and  $\varepsilon = 1 - \rho = 1$ .

The material-independent suppression function is used to modify  $k_{\text{accum}}$  of  $\text{TiO}_2$  to determine the effective thermal conductivity  $k_{\text{eff}}(r_0, \Omega) = \int_0^\infty S(\Lambda, r_0, \Omega) k_\Lambda d\Lambda$  in terms of the experiment-specific

lengths and timescales. Here,  $S$  weights a phonon's contribution to thermal conductivity local to the nanoscale CF as compared to in a bulk system. Although the gray BTE is solved,  $S$  is used to suppress contributions from all phonons in the spectrum based on their MFP [131]. The effective thermal conductivity of TiO<sub>2</sub> vs. CF radius is shown in Fig. 6.1(e) for  $\Omega = 6.3 \times 10^8$  rad/s and  $\varepsilon = 1 - \rho = 1$  at  $T_\infty = 300$  and 500 K. Switching times faster than  $\sim 0.1$  ns ( $\Omega \sim 6.3 \times 10^{10}$  rad/s) cause added suppression due to the reduction of the thermal penetration depth in the TiO<sub>2</sub>.

## V. Predicting conductive filament temperature

To predict the surface temperature of the CF using a simple thermal diffusion analysis  $k_{\text{eff}}$  is used instead of  $k_{\text{bulk}}$ . Solving the heat diffusion equation in cylindrical coordinates with periodic surface heating yields the surface temperature of the CF with  $k_{\text{bulk}}$  ( $T_{\text{s,bulk}}$ ) and  $k_{\text{eff}}$  ( $T_{\text{s,eff}}$ ) as the thermal conductivity of TiO<sub>2</sub>. The temperature  $T_{\text{s,eff}}$  accounts for weighted suppression of the full phonon spectrum by the definition of  $k_{\text{eff}}$  and is not the same as the surface temperature from Eq. (6.4a), which is defined for one phonon mode. The ratio  $T_{\text{s,eff}}/T_{\text{s,bulk}}$  is shown in Fig. 6.1(f) for  $T_\infty = 300$  and 500 K and indicates that the surface temperature augmentation of the CF will be larger as  $r_o$  becomes smaller. For example, for a CF with  $r_o = 1$  nm in TiO<sub>2</sub> at  $T_\infty = 300$  K, the actual temperature rise will be  $5\times$  larger than that predicted by the diffusion equation with  $k_{\text{bulk}}$ .

The ratio  $V_{\text{eff}}/V_{\text{bulk}}$  is determined following Ref. [159] and is the change in reset voltage when accounting for the CF surface temperature augmentation and is shown in Fig. 6.1(f) for  $T_\infty = 300$  and 500 K. Since the CF temperature rise increases due to nondiffusive phonon transport, less voltage is required to achieve the critical CF temperature and reset the device. These effects would be less pronounced in polycrystalline and amorphous TiO<sub>2</sub> and at higher operating temperatures since long phonon MFPs do not contribute as significantly in these conditions. Nonetheless if  $k_{\text{accum}}$  is known, the same  $S$  is used to identify  $k_{\text{eff}}$ ,  $T_{\text{s,eff}}$ , and  $V_{\text{s,eff}}$ .

## VI. Summary

In this chapter, I determined  $k_{\text{accum}}$  for rutile  $\text{TiO}_2$  at temperatures of 300 and 500 K from experimental  $k$  vs.  $T$  data. The accumulation function indicates that phonons with MFPs comparable to CF radii in RRAM devices contribute significantly to thermal transport, rendering the use of the heat diffusion equation to model thermal transport inadequate. Consequently, I develop an analytical solution to the BTE to model thermal transport in RRAM devices. A suppression function is developed to determine the effective thermal conductivity of the surrounding  $\text{TiO}_2$ . Using  $k_{\text{eff}}$  instead of  $k_{\text{bulk}}$  in a diffusion analysis shows that the actual temperature rise of a CF filament is larger than expected due to nondiffusive thermal transport.

## 7. OUTLOOK AND CONCLUSION

The study of  $k_{\text{accum}}$  has come a long way in the past decade. The experimental tools and interpretations to measure  $k_{\text{accum}}$  are being actively pursued. At the same time, first principles based computational methods have progressed to make accurate predictions of bulk thermal conductivity, and their predictions of  $k_{\text{accum}}$  for different materials represent the state of the art comparison for experimental results. Continued development and understanding of the experimental techniques will lead to exciting new topics of study and extensions of the work that is summarized and referenced throughout this dissertation. The following subsections outline some promising future research opportunities.

### I. Direct interpretation of experiments using the BTE

TTG, TDTR, and BB-FDTR induce nondiffusive thermal transport in a substrate and simultaneously sense information about the temperature profile in the system. Nondiffusive transport in the system affects the expected temporal and spatial temperature profile (i.e., from solving the diffusion equation). Up until now, the differences between the measured and expected temperature profiles are reconciled by using a reduced  $k$  in the diffusion equation and an experiment-specific suppression function to obtain  $k_{\text{accum}}$ . Hua and Minnich find that this is a reasonable approach in the “weakly quasiballistic regime” because the BTE prediction of temperature is of identical mathematical form to the diffusion equation, i.e., exponential decay with time in TTG [82]. An alternative approach is to directly fit the data with a model that inherently accounts for nondiffusive thermal transport such as a solution to the BTE in a system geometrically similar to the experimental setup. Even with very simple geometries the BTE is challenging to solve and recent attempts to improve upon the diffusive interpretation account for ballistic effects phenomenologically [78,176,177]. Complexities such as the transducer layer used in thermoreflectance techniques and the multiple timescales inherent to TDTR make rigorous solutions to the BTE a long-term challenge.

## II. Clarifying the role of the transducer/interface

In thermoreflectance experiments, a metal transducer is used to eliminate volumetric heating in the substrate and increase the signal to noise ratio. A metal that has a high coefficient of thermoreflectance at the probe laser wavelength is chosen as the transducer. For TDTR, this metal is aluminum and for BB-FDTR, this metal is gold (where a chromium adhesion layer is used between the gold and substrate). The aforementioned discrepancy of  $k_{\text{exp}}$  vs.  $L_p$  by TDTR and BB-FDTR (i.e., TDTR shows no  $L_p$ -dependence on  $k_{\text{exp}}$ , while BB-FDTR does) could potentially be the result of using different transducer materials. Two possible reasons are (1) weak electron-phonon coupling in the gold could influence the reported value of  $k_{\text{exp}}$  in BB-FDTR and (2) spectrally-dependent phonon transmission at the transducer-silicon interface determine which phonons will be excited in the silicon.

Reason (1) was addressed in Chapter 5 of this dissertation. By fitting BB-FDTR data with a two-temperature model that accounted for arbitrary heat deposition, it was found that accounting for electron-phonon non-equilibrium in the gold transducer does diminish the heating frequency dependence of thermal conductivity in silicon but does not eliminate it. Regarding reason (2), the interface between the transducer and substrate may affect the measured thermal conductivity in TDTR and BB-FDTR experiments, e.g., the interface could selectively excite specific phonon modes in the substrate. It was found in Ref. [83] (see Chapter 4) that the suppression function is dependent on the properties of the interface and consequently predicts different  $k_{\text{exp}}$  vs.  $L_p$  for TDTR (where the transducer/substrate interface is aluminum/silicon) and BB-FDTR (where the transducer/substrate interface is chromium/silicon).

The MFPs of phonons excited at the interface in thermoreflectance experiments can be identified with an interface thermal conductance accumulation function  $G_{\text{accum}}$  that describes MFP-dependent contributions of phonons to interface thermal conductance. An analytical expression for the interface thermal conductance accumulation function can be derived in a similar manner as  $k_{\text{accum}}$  was in Eq. (1.7). Beginning from Eqs. (2.10) and (2.11) from Ref. [129] and assuming that scattering at the interface is diffuse and elastic, one polarization, and both materials are isotropic,

$$G = \frac{1}{4} \int_0^\infty v_L \alpha_{L \rightarrow R} \hbar \omega D_L(\omega) \frac{\partial g_{BE}}{\partial T} d\omega, \quad (7.1)$$

where the subscripts L and R correspond to the materials to the left and right of the interface and  $\alpha_{L \rightarrow R}$  is the phonon transmission coefficient for phonons traveling from the material on the left to the material on the right. Eq. (7.1) can be simplified by assuming Debye dispersion and density of states, and the high temperature limit ( $g_{BE} = k_B T / \hbar \omega$ ),

$$G = \frac{1}{8\pi^2} \int_0^{\omega_{BZE}} \alpha_{L \rightarrow R} \frac{\omega^2}{v_L^2} k_B d\omega. \quad (7.2)$$

Following a similar procedure for  $k_{accum}$ , I assume power law scattering of the form  $\Lambda(\omega) = B_L \omega^{-n}$ .

Substituting and transforming variables from  $\omega$  to  $\Lambda$  yields

$$G_{accum}(\Lambda^*) = \frac{1}{8\pi^2} \int_{\Lambda_{min}}^{\Lambda^*} \frac{\alpha_{L \rightarrow R} k_B}{n v_L^2} B_L^n \Lambda^{-\frac{3}{n}-1} d\Lambda. \quad (7.3)$$

Integrating and normalizing by  $G$  (evaluated when  $\Lambda^* \rightarrow \infty$ ) yields the following expression,

$$\frac{G_{accum}(\Lambda^*)}{G} = 1 - \left( \frac{\Lambda_{min}}{\Lambda^*} \right)^{\frac{3}{n}}. \quad (7.4)$$

where, the lesser of  $\Lambda_{min}$  of the transducer or substrate, as determined by  $\Lambda(\omega_{BZE})$  in each material, is used.

The normalized thermal conductivity and interface thermal conductance accumulation functions for silicon at  $T = 300$  K with  $n = 2$  are shown in Fig. 7.1. Here, the interface thermal conductance accumulation function is plotted as a function of the MFPs in silicon for transducers with different Debye temperatures  $\theta_D$ . The result shows that the range of MFPs that contribute to interface thermal conductance is far narrower than those that contribute to thermal conductivity. Furthermore, as the transducer Debye temperature decreases below the substrate Debye temperature, high frequency, short MFP phonons are not excited in the substrate at the interface. Anharmonic processes near the interface may excite these phonons, but it is possible that the transducer/substrate Debye temperature mismatch has implications on the obtained  $k_{accum}$ .

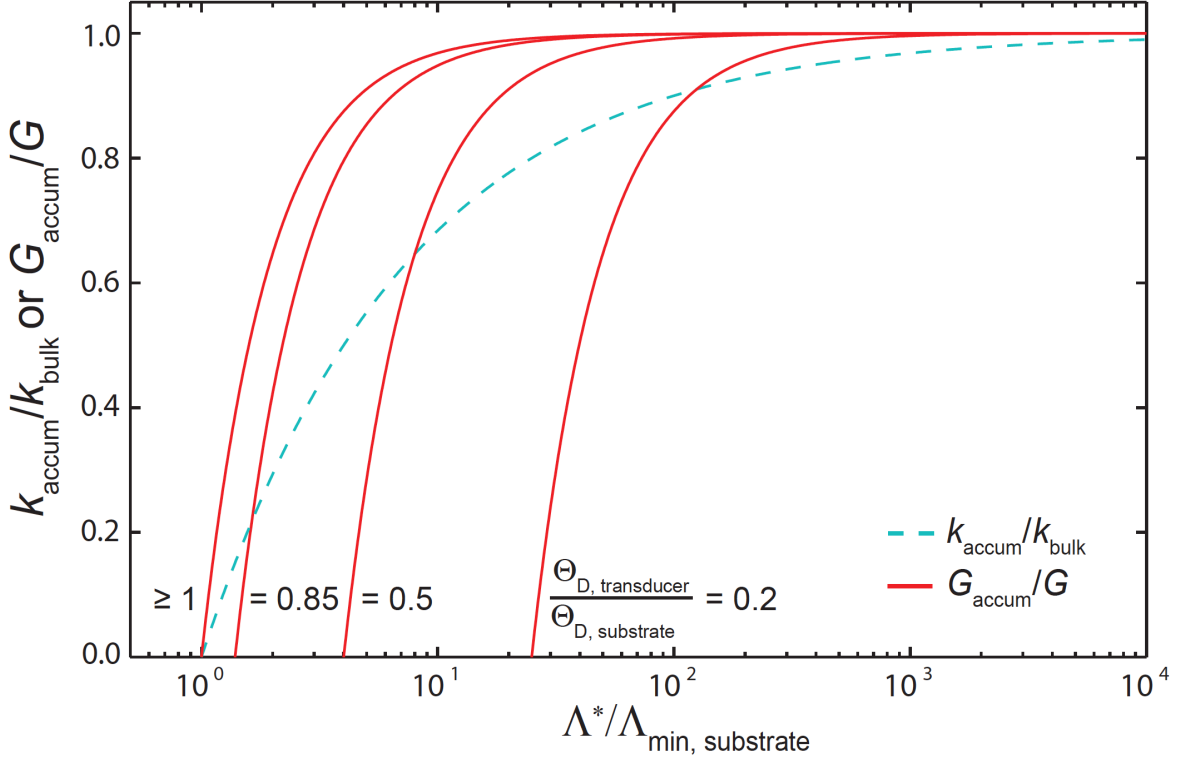


Fig. 7.1. The normalized thermal conductivity accumulation function for silicon at  $T = 300$  K [Eq. (1.11)] plotted with the interface thermal conductance accumulation function [Eq. (7.4)] vs. the ratio of  $\Lambda^*$  and  $\Lambda_{\min}$  of the substrate ( $\Lambda_{\min}$  in silicon is 27 nm at  $T = 300$  K) for different transducer Debye temperatures.

### III. Alloys and nanograined materials

Alloys and nanograined materials exhibit unique thermal and optical properties. Examples include the high thermoelectric figure-of-merit in nanograined silicon [30], bismuth antimony telluride [2] and SiGe alloys [178], and AlGaIn crystals [13], which are commonly used in LEDs. To date, researchers have measured the bulk and nanostructured thermal conductivity of these materials and analyzed the scattering mechanisms over a wide range of temperatures. Measuring  $k_{\text{accum}}$  in alloys and nanograined materials will shed new light on the phonon scattering mechanisms. Understanding the contributions of grain boundary and alloy scattering also has applications in superlattices, membranes, and many other nanostructured materials.

## IV. Electron-dominated materials

Non-equilibrium between electrons and phonons results in the exchange of thermal energy between the two energy carriers. How nondiffusive thermal transport affects the measured thermal conductivity of a non-equilibrium system remains an open research question. Thermal transport in metals is commonly modeled with a diffusive two-temperature model [134], where the electron and phonon temperatures are separately defined and represent thermal excitations of the two energy carriers within the system. Early studies of thermal transport in metals used TDTR to measure electron-phonon scattering and coupling rates [136] and the size effects of non-equilibrium thermal transport in metal films [135,179]. More recently, researchers have examined the thermal conductivity of gold films [180,181] and the non-equilibrium thermal conductance between thin metal bilayers [108,132] and metal-dielectric interfaces [139]. Recent advances in the metrology of thermal conductivity open new channels for studying systems where non-equilibrium transport processes coexist with nondiffusive transport processes. New transport models and measurements that separate the onset of these two effects may provide deeper understanding of the physics within metals as well as numerous other coupled energy systems [138,182-184].

## V. Beyond 3-D materials

Extending nondiffusive thermal conductivity measurements to non-bulk, single crystal materials (e.g., 2-D materials, superlattices, membranes, roughened membranes, etc.) can lead to information about optimal structure for increased thermoelectric figure-of-merit, dominant scattering mechanisms, and phonon physics. Experimental modifications must be considered in order to measure  $k_{\text{accum}}$  for these materials. Graphene is a notable example where a traditional thermoreflectance experiment will not work to measure  $k_{\text{accum}}$  since it must be coated with a metal transducer. Coating graphene with a transducer is undesirable since it will modify the phonon modes in the material [185]. TTG is a natural candidate for measuring graphene, but sufficiently large single crystals are required. Alternatively, graphene has an

adequate coefficient of thermorefectance in the UV-regime, which generates a sufficient signal without the necessity of a transducer layer [186,187].

Additionally, to probe  $k_{\text{accum}}$  in 2-D materials with thermorefectance techniques it is necessary to modify the suppression function. This can be done analytically by solving the 1-D BTE in polar coordinates in the radial direction. I begin with the 1-D, gray BTE in cylindrical coordinates under the relaxation time approximation in an isotropic medium as given in Eq. (6.2). For a 2-D material, the polar angle  $\theta$  is constrained to be  $\pi/2$  [i.e., there is no transport in the  $z$ -direction (see Fig. 6.1(c))] and Eq. (6.2) reduces to

$$\frac{1}{v_s} \frac{\partial n}{\partial t} + \cos\psi \frac{\partial n}{\partial r} - \frac{\sin\psi}{r} \frac{\partial n}{\partial \psi} = \frac{n_e - n}{\Lambda} \quad , \quad (7.5)$$

where  $n(r, t, \psi)$  is the phonon energy density per unit phonon frequency per unit solid angle and is a function of  $r$ -coordinate, time, and azimuthal angle  $\psi$ . The  $P_1$  approximation yields

$$\frac{1}{v_s} \frac{\partial n_0}{\partial t} + \frac{\partial n_2}{\partial r} + \frac{n_2}{r} = 0 \quad , \quad (7.6a)$$

$$\frac{1}{v_s} \frac{\partial n_2}{\partial t} + \frac{1}{2} \frac{\partial n_0}{\partial r} + \frac{n_2}{\Lambda} = 0 \quad . \quad (7.6b)$$

Separating variables and using the same boundary conditions as were used in Chapter 6 for the cylindrical heat source yields the time-independent spatial temperature and heat flux profiles,  $\bar{T}_{\text{BTE}}(r)$  and  $\bar{q}''_{\text{BTE}}(r)$  as

$$\bar{T}_{\text{BTE}}(r) = \frac{\int_0^\infty \bar{n}_0 d\omega}{\int_0^\infty c_\omega d\omega} = v_s \beta \varepsilon T_s K_0(\beta r) / \Gamma \quad , \quad (7.7a)$$

$$\bar{q}''_{\text{BTE}}(r) = \int_0^\infty v_s \bar{n}_2 d\omega = i \Omega C v_s \varepsilon T_s K_1(\beta r) / \Gamma \quad , \quad (7.7b)$$

where  $\Gamma = v_s \beta K_0(\beta r_0)(1 - \rho) + 2i \Omega K_1(\beta r_0)(1 + \rho)$ ,  $K_0$  and  $K_1$  are the modified Bessel functions of the second kind of order 0 and 1, and  $\beta = \sqrt{2\Omega(i v_s - \Omega\Lambda)/(v_s^2 \Lambda)}$ . These are the same expression as the cylindrical case [Eq. (6.4)] except that the parameter  $\beta$  differs by a constant value due to the reduced

dimensionality compared to the cylindrical case. Using Eq. (7.7), the suppression function can be determined and used to map experimental length scales  $L_p$  and  $r_o$  to phonon MFPs in 2-D materials in a similar manner as for bulk materials.

## VI. Conclusion

The work I have completed and described in this dissertation has contributed to the advancement of the field of nanoscale thermal transport. Experimental observation of nondiffusive thermal transport is possible with BB-FDTR. I have presented theoretical frameworks that were used to interpret those observations, but these interpretations are an ongoing research topic. There are still many avenues that remain open for exploration related to the MFP-dependent contributions to  $k$  and the relationship between experimental length and timescales and phonon properties. Ultimately, further development of metrology and interpretation, combined with first principles theory and calculations, will lead to valuable information for scientists and engineers in relation to increasing the thermoelectric figure-of-merit, engineering thermal management in devices, and understanding the physics of thermal energy carriers.

## REFERENCES

1. A. I. Hochbaum, R. Chen, R. D. Delgado, W. Liang, E. C. Garnett, M. Najarian, A. Majumdar, and P. Yang, Enhanced Thermoelectric Performance of Rough Silicon Nanowires, *Nature*, vol. 451, pp. 163-168, 2008.
2. B. Poudel, Q. Hao, Y. Ma, Y. Lan, A. J. Minnich, B. Yu, X. Yan, D. Wang, A. Muto, D. Vashaee, X. Chen, J. Liu, M. S. Dresselhaus, G. Chen, and Z. Ren, High-Thermoelectric Performance of Nanostructured Bismuth Antimony Telluride Bulk Alloys, *Science*, vol. 320, pp. 634-638, 2008.
3. R. J. Mehta, Y. L. Zhang, C. Karthik, B. Singh, R. W. Siegel, T. Borca-Tasciuc, and G. Ramanath, A New Class of Doped Nanobulk High-Figure-of-Merit Thermoelectrics by Scalable Bottom-up Assembly, *Nature Materials*, vol. 11, pp. 233-240, 2012.
4. L. Shi, Thermal and Thermoelectric Transport in Nanostructures and Low-Dimensional Systems, *Nanoscale and Microscale Thermophysical Engineering*, vol. 16, pp. 79-116, 2012.
5. B. Yu, M. Zebarjadi, H. Wang, K. Lukas, H. Wang, D. Wang, C. Opeil, M. S. Dresselhaus, G. Chen, and Z. Ren, Enhancement of Thermoelectric Properties by Modulation-Doping in Silicon Germanium Alloy Nanocomposites, *Nano Letters*, vol. 12, pp. 2077-2082, 2012.
6. W. Ong, S. M. Rupich, D. V. Talapin, A. J. H. McGaughey, and J. A. Malen, Surface Chemistry Mediates Thermal Transport in Three-Dimensional Nanocrystal Arrays, *Nature Materials*, vol. 12, pp. 410-415, 2013.
7. A. Shah, P. Torres, R. Tscharnner, N. Wyrsh, and H. Keppner, Photovoltaic Technology: The Case for Thin-Film Solar Cells, *Science*, vol. 285, pp. 692-698, 1999.
8. M. Gratzel, Perspectives for Dye-Sensitized Nanocrystalline Solar Cells, *Progress in Photovoltaics: Research and Applications*, vol. 8, pp. 171-185, 2000.
9. K. Ramanathan, M. A. Contreras, C. L. Perkins, S. Asher, F. S. Hasoon, J. Keane, D. Young, M. Romero, W. Metzger, R. Noufi, J. Ward, and A. Duda, Properties of 19.2% Efficiency

- ZnO/CdS/CuInGaSe<sub>2</sub> Thin-Film Solar Cells, *Progress in Photovoltaics: Research and Applications*, vol. 11, pp. 225-230, 2003.
10. M. J. Currie, J. K. Mapel, T. D. Heidel, S. Goffri, and M. A. Baldo, High-Efficiency Organic Solar Concentrators for Photovoltaics, *Science*, vol. 321, pp. 226-228, 2008.
  11. E. F. Schubert, N. E. J. Hunt, M. Micovic, R. J. Malik, D. L. Sivco, A. Y. Cho, and G. J. Zyzdik, Highly Efficient Light-Emitting Diodes with Microcavities, *Science*, vol. 12, pp. 943-945, 1994.
  12. S. Nakamura, The Roles of Structural Imperfections in InGaN-Based Blue Light-Emitting Diodes and Laser Diodes, *Science*, vol. 14, pp. 956-961, 1998.
  13. W. Liu and A. A. Balandin, Temperature Dependence of Thermal Conductivity of Al<sub>x</sub>Ga<sub>1-x</sub>N Thin Films Measured by the Differential 3 Omega Technique, *Applied Physics Letters*, vol. 85, pp. 5230-5232, 2004.
  14. J. J. Wierer, A. David, and M. M. Megens, III-Nitride Photonic-Crystal Light-Emitting Diodes with High Extraction Efficiency, *Nature Photonics*, vol. 3, pp. 163-169, 2009.
  15. Z. Su, L. Huang, F. Liu, J. P. Freedman, L. M. Porter, R. F. Davis, and J. A. Malen, Layer-by-Layer Thermal Conductivities of the Group III Nitride Films in Blue/Green Light Emitting Diodes, *Applied Physics Letters*, vol. 100, pp. 201106, 2012.
  16. Z. Su, J. P. Freedman, J. H. Leach, E. A. Preble, R. F. Davis, and J. A. Malen, The Impact of Film Thickness and Substrate Surface Roughness on the Thermal Resistance of Aluminum Nitride Nucleation Layers, *Journal of Applied Physics*, vol. 113, pp. 213503, 2013.
  17. G. Chen, Nonlocal and Nonequilibrium Heat Conduction in the Vicinity of Nanoparticles, *Journal of Heat Transfer*, vol. 118, pp. 539-545, 1996.
  18. P. G. Sverdrup, S. Sinha, M. Ashegi, S. Uma, and K. E. Goodson, Measurement of Ballistic Phonon Conduction near Hotspots in Silicon, *Applied Physics Letters*, vol. 78, pp. 3331-3333, 2001.

19. A. J. Minnich, J. A. Johnson, A. J. Schmidt, K. Esfarjani, M. S. Dresselhaus, K. A. Nelson, and G. Chen, Thermal Conductivity Spectroscopy Technique to Measure Phonon Mean Free Paths, *Physical Review Letters*, vol. 107, pp. 095901, 2011.
20. A. A. Joshi and A. Majumdar, Transient Ballistic and Diffusive Phonon Heat Transport in Thin Films, *Journal of Applied Physics*, vol. 74, pp. 31-39, 1993.
21. A. Majumdar, Microscale Heat Conduction in Dielectric Thin Films, *Journal of Heat Transfer*, vol. 115, pp. 7-16, 1993.
22. M. Ashegi, Y. K. Leung, S. S. Wong, and K. E. Goodson, Phonon-Boundary Scattering in Thin Silicon Layers, *Applied Physics Letters*, vol. 71, pp. 1798-1800, 1997.
23. M. Ashegi, Y. K. Leung, S. S. Wong, M. N. Touzelbaev, and K. E. Goodson, Temperature-Dependent Thermal Conductivity of Single-Crystal Silicon Layers in SOI Substrates, *Journal of Heat Transfer*, vol. 120, pp. 30-36, 1998.
24. Y. S. Ju and K. E. Goodson, Phonon Scattering in Silicon Films with Thickness of Order 100 nm, *Applied Physics Letters*, vol. 74, pp. 3004-3007, 1999.
25. P. Kim, L. Shi, A. Majumdar, and P. L. McEuen, Thermal Transport Measurements of Individual Multiwalled Nanotubes, *Physical Review Letters*, vol. 87, pp. 215502, 2001.
26. D. Li, Y. Wu, P. Kim, L. Shi, P. Yang, and A. Majumdar, Thermal Conductivity of Individual Silicon Nanowires, *Applied Physics Letters*, vol. 83, pp. 2934-2936, 2003.
27. C. Dames and G. Chen, Theoretical Phonon Thermal Conductivity of Si/Ge Superlattice Nanowires, *Journal of Applied Physics*, vol. 95, pp. 682-693, 2004.
28. D. Song and G. Chen, Thermal Conductivity of Periodic Microporous Silicon Films, *Applied Physics Letters*, vol. 84, pp. 687-689, 2004.
29. J. Chen, G. Zhang, and B. Li, Tunable Thermal Conductivity of  $\text{Si}_{1-x}\text{Ge}_x$  Nanowires, *Applied Physics Letters*, vol. 95, pp. 073117, 2009.

30. Z. Wang, J. E. Alaniz, W. Jang, J. E. Garay, and C. Dames, Thermal Conductivity of Nanocrystalline Silicon: Importance of Grain Size and Frequency-Dependent Mean Free Paths, *Nano Letters*, vol. 11, pp. 2206-2213, 2011.
31. A. A. Balandin, Thermal Properties of Graphene and Nanostructured Carbon Materials, *Nature Materials*, vol. 10, pp. 569-581, 2011.
32. A. A. Maznev, Onset of Size Effect in Lattice Thermal Conductivity of Thin Films, *Journal of Applied Physics*, vol. 113, pp. 113511, 2013.
33. X. Xu, L. F. C. Pereira, Y. Wang, J. Wu, K. Zhang, X. Zhao, S. Bae, C. T. Bui, R. Xie, J. T. L. Thong, B. H. Hong, K. P. Loh, D. Donadio, B. Li, and B. Ozyilmaz, Length-Dependent Thermal Conductivity in Suspended Single-Layer Graphene, *Nature Communications*, vol. 5, pp. 3689, 2014.
34. J. Maassen and M. Lundstrom, Steady-State Heat Transport: Ballistic-to-Diffusive with Fourier's Law, *arXiv:1408.1631*, vol., 2014.
35. M. E. Siemens, Q. Li, R. Yang, K. A. Nelson, E. H. Anderson, M. M. Murnane, and H. C. Kapteyn, Quasi-Ballistic Thermal Transport from Nanoscale Interfaces Observed Using Ultrafast Coherent Soft X-Ray Beams, *Nature Materials*, vol. 9, pp. 26-30, 2009.
36. S. Mansoor and B. S. Yilbas, Phonon Transport in Silicon Thin Film: Effect of Temperature Oscillation on Effective Thermal Conductivity, *Transport Theory and Statistical Physics*, vol. 42, pp. 179-201, 2013.
37. A. S. Henry and G. Chen, Spectral Phonon Transport Properties of Silicon Based on Molecular Dynamics Simulations and Lattice Dynamics, *Journal of Computational and Theoretical Nanoscience*, vol. 5, pp. 1-12, 2008.
38. C. Dames and G. Chen, Thermal Conductivity of Nanostructured Thermoelectric Materials, in D. M. Rowe (ed.), *Thermoelectrics Handbook: Macro to Nano*, CRC Press, Boca Raton, FL, 2006.
39. G. Chen. *Nanoscale Energy Transport and Conversion* (Oxford University Press, Inc., New York, 2005).

40. A. Majumdar, Microscale Energy Transport in Solids, in C. L. Tien, A. Majumdar, & F. M. Gerner (ed.), *Microscale Energy Transport*, Taylor & Francis, Washington, DC, 1998.
41. F. Yang and C. Dames, Mean Free Path Spectra as a Tool to Understand Thermal Conductivity in Bulk and Nanostructures, *Physical Review B*, vol. 87, pp. 035437, 2013.
42. D. T. Morelli, J. P. Heremans, and G. A. Slack, Estimation of the Isotope Effect on the Lattice Thermal Conductivity of Group IV and Group III-V Semiconductors, *Physical Review B*, vol. 66, pp. 195304, 2002.
43. G. A. Slack and S. Galginaitis, Thermal Conductivity and Phonon Scattering by Magnetic Impurities in CdTe, *Physical Review*, vol. 133, pp. A253-A268, 1964.
44. M. G. Holland, Analysis of Lattice Thermal Conductivity, *Physical Review*, vol. 132, pp. 2461-2471, 1963.
45. K. Esfarjani and G. Chen, Heat Transport in Silicon from First-Principles Calculations, *Physical Review B*, vol. 84, pp. 085204, 2011.
46. J. E. Turney, E. S. Landry, A. J. H. McGaughey, and C. H. Amon, Predicting Phonon Properties and Thermal Conductivity from Anharmonic Lattice Dynamics Calculations and Molecular Dynamics Simulations, *Physical Review B*, vol. 79, pp. 064301, 2009.
47. J. A. Reissland. *The Physics of Phonons* (John Wiley & Sons Ltd, New York, NY, 1973).
48. D. A. Broido, M. Malorny, G. Birner, N. Mingo, and D. A. Stewart, Intrinsic Lattice Thermal Conductivity of Semiconductors from First Principles, *Applied Physics Letters*, vol. 91, pp. 231922, 2007.
49. A. Ward and D. A. Broido, Ab Initio Theory of the Lattice Thermal Conductivity in Diamond, *Physical Review B*, vol. 80, pp. 125203, 2009.
50. L. Lindsay, D. A. Broido, and T. L. Reinecke, Ab Initio Thermal Transport in Compound Semiconductors, *Physical Review B*, vol. 87, pp. 165201, 2013.
51. M. T. Dove. *Introduction of Lattice Dynamics* (Cambridge University Press, Cambridge, UK, 1993).

52. M. Omini and A. Sparavigna, Beyond the Isotropic-Model Approximation in the Theory of Thermal Conductivity, *Physical Review B*, vol. 53, pp. 9064-9073, 1996.
53. L. Lindsay, D. A. Broido, and N. Mingo, Flexural Phonons and Thermal Transport in Graphene, *Physical Review B*, vol. 82, pp. 115427, 2010.
54. L. Zeng and G. Chen, Disparate Quasiballistic Heat Conduction Regimes for Periodic Heat Sources on a Substrate, *Journal of Applied Physics*, vol. 116, pp. 064307, 2014.
55. O. Delaire, J. Ma, K. Marty, A. F. May, M. A. McGuire, M.-H. Du, D. J. Singh, A. Podlesnyak, G. Ehlers, M. D. Lumsden, and B. C. Sales, Giant Anharmonic Phonon Scattering in Pbte, *Nature Materials*, vol. 10, pp. 614-619, 2011.
56. M. Trigo, M. Fuchs, J. Chen, M. P. Jiang, M. Cammarata, S. Fahy, D. M. Fritz, K. Gaffney, S. Ghimire, A. Higginbotham, S. L. Johnson, M. E. Kozina, J. Larsson, H. Lemke, A. M. Lindenberg, G. Ndabashimiye, F. Quirin, K. Sokolowski-Tinten, C. Uher, G. Wang, J. S. Wark, D. Zhu, and D. A. Reis, Fourier-Transform Inelastic X-Ray Scattering from Time- and Momentum-Dependent Phonon-Phonon Correlations, *Nature Physics*, vol. 9, pp. 790-794, 2013.
57. K. A. Nelson, D. R. Lutz, M. D. Fayer, and L. Madison, Laser-Induced Phonon Spectroscopy. Optical Generation of Ultrasonic Waves and Investigation of Electronic Excited-State Interactions in Solids, *Physical Review B*, vol. 24, pp. 3261-3275, 1981.
58. J. S. Meth, C. D. Marshall, and M. D. Fayer, Generation and Detection of Acoustic Waveguide Modes in Ultrathin Crystals Using the Transient Grating Technique, *Chemical Physics Letters*, vol. 162, pp. 306-312, 1989.
59. A. Harata, H. Nishimura, and T. Sawada, Laser-Induced Surface Acoustic Waves and Photothermal Surface Gratings Generated by Crossing Two Pulsed Laser Beams, *Applied Physics Letters*, vol. 57, pp. 132-134, 1990.
60. A. R. Duggal, J. A. Rogers, K. A. Nelson, and M. Rothschild, Realtime Characterization of Acoustic Modes of Polyimide Thinfilm Coatings Using Impulsive Stimulated Thermal Scattering, *Applied Physics Letters*, vol. 60, pp. 692-694, 1992.

61. J. A. Rogers and K. A. Nelson, Study of Lamb Acoustic Waveguide Modes in Unsupported Polyimide Thin Films Using Real-Time Impulsive Stimulated Thermal Scattering, *Journal of Applied Physics*, vol. 75, pp. 1534-1556, 1994.
62. J. A. Rogers, A. A. Maznev, M. J. Banet, and K. A. Nelson, Optical Generation and Characterization of Acoustic Waves in Thin Films - Fundamentals and Applications, *Annual Review of Materials Science*, vol. 30, pp. 117-157, 2000.
63. J. A. Johnson, A. A. Maznev, J. K. Eliason, A. J. Minnich, K. Collins, G. Chen, J. Cuffe, T. Kehoe, C. M. Sotomayor Torres, and K. A. Nelson, Experimental Evidence of Non-Diffusive Thermal Transport in Si and GaAs, *MRS Proceedings*, vol. 1347, 2011.
64. J. A. Johnson, A. A. Maznev, M. T. Bulsara, E. A. Fitzgerald, T. C. Harman, S. Calawa, C. J. Vineis, G. Turner, and K. A. Nelson, Phase-Controlled, Heterodyne Laser-Induced Transient Grating Measurements of Thermal Transport Properties in Opaque Materials, *Journal of Applied Physics*, vol. 111, pp. 023503, 2012.
65. J. A. Johnson, A. A. Maznev, J. Cuffe, J. K. Eliason, A. J. Minnich, T. Kehoe, C. M. Sotomayor Torres, G. Chen, and K. A. Nelson, Direct Measurement of Room-Temperature Nondiffusive Thermal Transport over Micron Distances in a Silicon Membrane, *Physical Review Letters*, vol. 110, pp. 025901, 2013.
66. C. A. Paddock and G. L. Eesley, Transient Thermoreflectance from Thin Metal Films, *Journal of Applied Physics*, vol. 60, pp. 285-290, 1986.
67. W. S. Capinski and H. J. Maris, Improved Apparatus for Picosecond Pump-and-Probe Optical Measurements, *Review of Scientific Instruments*, vol. 67, pp. 2720-2726, 1996.
68. B. Bonello, B. Perrin, and C. Rossignol, Photothermal Properties of Bulk and Layered Materials by the Picosecond Acoustics Technique, *Journal of Applied Physics*, vol. 83, pp. 3081-3088, 1998.

69. N. Taketoshi, T. Baba, E. Schaub, and A. Ono, Homodyne Detection Technique Using Spontaneously Generated Reference Signal in Picosecond Thermoreflectance Measurements, *Review of Scientific Instruments*, vol. 74, pp. 5226-5230, 2003.
70. D. G. Cahill, Analysis of Heat Flow in Layered Structures for Time-Domain Thermoreflectance, *Review of Scientific Instruments*, vol. 75, pp. 5119-5122, 2004.
71. Y. K. Koh and D. G. Cahill, Frequency Dependence of the Thermal Conductivity of Semiconductor Alloys, *Physical Review B*, vol. 76, pp. 075207, 2007.
72. D. Ding, X. Chen, and A. J. Minnich, Radial Quasiballistic Transport in Time-Domain Thermoreflectance Studied Using Monte Carlo Simulations, *Applied Physics Letters*, vol. 104, pp. 143104, 2014.
73. K. T. Regner, D. P. Sellan, Z. Su, C. H. Amon, A. J. H. McGaughey, and J. A. Malen, Broadband Phonon Mean Free Path Contributions to Thermal Conductivity Measured Using Frequency Domain Thermoreflectance, *Nature Communications*, vol. 4, pp. 1640, 2013.
74. K. T. Regner, S. Majumdar, and J. A. Malen, Instrumentation of Broadband Frequency Domain Thermoreflectance for Measuring Thermal Conductivity Accumulation Functions, *Review of Scientific Instruments*, vol. 84, pp. 064901, 2013.
75. J. P. Freedman, J. H. Leach, E. A. Preble, Z. Sitar, R. F. Davis, and J. A. Malen, Universal Phonon Mean Free Path Spectra in Crystalline Semiconductors at High Temperature, *Scientific Reports*, vol. 3, pp. 2963, 2013.
76. J. A. Schmidt, R. Cheaito, and M. Chiesa, A Frequency-Domain Thermoreflectance Method for the Characterization of Thermal Properties, *Review of Scientific Instruments*, vol. 80, pp. 094901, 2009.
77. K. C. Collins, A. A. Maznev, J. Cuffe, K. A. Nelson, and G. Chen, Examining Thermal Transport through a Frequency-Domain Representation of Time-Domain Thermoreflectance Data, *Review of Scientific Instruments*, vol. 85, pp. 124903, 2014.

78. R. B. Wilson and D. G. Cahill, Anisotropic Failure of Fourier Theory in Time-Domain Thermoreflectance Experiments, *Nature Communications*, vol. 5, pp. 5075, 2014.
79. A. A. Maznev, J. A. Johnson, and K. A. Nelson, Onset of Nondiffusive Phonon Transport in Transient Thermal Grating Decay, *Physical Review B*, vol. 84, pp. 195206, 2011.
80. A. J. Minnich, Determining Phonon Mean Free Paths from Observations of Quasiballistic Thermal Transport, *Physical Review Letters*, vol. 109, pp. 205901, 2012.
81. K. C. Collins, A. A. Maznev, Z. Tian, K. Esfarjani, K. A. Nelson, and G. Chen, Non-Diffusive Relaxation of a Transient Thermal Grating Analyzed with the Boltzmann Transport Equation, *Journal of Applied Physics*, vol. 114, pp. 104302, 2013.
82. C. Hua and A. J. Minnich, Transport Regimes in Quasiballistic Heat Conduction, *Physical Review B*, vol. 89, pp. 094302, 2014.
83. K. T. Regner, A. J. H. McGaughey, and J. A. Malen, Analytical Interpretation of Non-Diffusive Phonon Transport in Thermoreflectance Thermal Conductivity Measurements, *Physical Review B*, vol. 90, pp. 064302, 2014.
84. A. J. Minnich, G. Chen, S. Mansoor, and B. S. Yilbas, Quasiballistic Heat Transfer Studied Using the Frequency-Dependent Boltzmann Transport Equation, *Physical Review B*, vol. 84, pp. 235207, 2011.
85. A. Jain, Y. J. Yu, and A. J. H. McGaughey, Phonon Transport in Periodic Silicon Nanoporous Films with Feature Sizes Greater Than 100 nm, *Physical Review B*, vol. 87, pp. 195301, 2013.
86. A. J. H. McGaughey and A. Jain, Nanostructure Thermal Conductivity Prediction by Monte Carlo Sampling of Phonon Mean Free Paths, *Applied Physics Letters*, vol. 100, pp. 061911, 2012.
87. J. A. Malen, K. Baheti, T. Tong, Y. Zhao, J. A. Hudgings, and A. Majumdar, Optical Measurement of Thermal Conductivity Using Fiber Aligned Frequency Domain Thermoreflectance, *Journal of Heat Transfer*, vol. 133, pp. 081601, 2011.

88. N. Taketoshi, M. Ozawa, H. Ohta, and T. Baba, Thermal Effusivity Distribution Measurements Using a Thermoreflectance Technique, *AIP Conference Proceedings*, vol. 463, pp. 315-317, 1999.
89. K. Hatori, N. Taketoshi, T. Baba, and H. Ohta, Thermoreflectance Technique to Measure Thermal Effusivity Distribution with High Spatial Resolution, *Review of Scientific Instruments*, vol. 76, pp. 114901, 2005.
90. F. Lepoutre, D. Balageas, P. Forge, S. Hirschi, J. L. Joulaud, D. Rochais, and F. C. Chen, Micron-Scale Thermal Characterizations of Interfaces Parallel or Perpendicular to the Surface, *Journal of Applied Physics*, vol. 78, pp. 2208-2223, 1995.
91. L. Pottier, Micrometer Scale Visualization of Thermal Waves by Photoreflectance Microscopy, *Applied Physics Letters*, vol. 64, pp. 1618-1619, 1994.
92. W. J. Scouler, Temperature-Modulated Reflectance of Gold from 2 to 10 eV, *Physical Review Letters*, vol. 18, pp. 445-448, 1967.
93. H. S. Carslaw and J. C. Jaeger. *Conduction of Heat in Solids* 2 ed. (Oxford University Press, New York, 1959).
94. R. M. Costescu, M. A. Wall, and D. G. Cahill, Thermal Conductance of Epitaxial Interfaces, *Physical Review B*, vol. 67, pp. 054302, 2003.
95. A. V. Inyushkin, A. N. Taldenkov, A. M. Gibin, A. V. Gusev, and H. J. Pohl, On the Isotope Effect in Thermal Conductivity of Silicon, *Physica Status Solidi C*, vol. 1, pp. 2995-2998, 2004.
96. Z. Yan, G. Liu, J. M. Khan, and A. A. Balandin, Graphene Quilts for Thermal Management of High-Power GaN Transistors, *Nature Communications*, vol. 3, pp. 827, 2012.
97. D. P. Sellan, J. E. Turney, A. J. H. McGaughey, and C. H. Amon, Cross-Plane Phonon Transport in Thin Films, *Journal of Applied Physics*, vol. 108, pp. 113524, 2010.
98. J. Callaway, Model for Lattice Thermal Conductivity at Low Temperatures, *Physical Review*, vol. 113, pp. 1046-1051, 1959.

99. T. Yamane, N. Nagai, S. Katayama, and M. Todoki, Measurement of Thermal Conductivity of Silicon Dioxide Thin Films Using a  $3\omega$  Method, *Journal of Applied Physics*, vol. 91, pp. 9772-9776, 2002.
100. N. W. Ashcroft and N. D. Mermin. *Solid State Physics* (Thomson Learning, Inc., New York, 1976).
101. A. Nabovati, D. P. Sellan, and C. H. Amon, On the Lattice Boltzmann Method for Phonon Transport, *J. Comput. Phys.*, vol. 230, pp. 5864-5876, 2011.
102. G. A. Slack, Thermal Conductivity of Pure and Impure Silicon, Silicon Carbide, and Diamond, *Journal of Applied Physics*, vol. 35, pp. 3460-3466, 1964.
103. F. P. Incropera, D. P. Dewitt, T. L. Bergman, and A. S. Lavine. *Fundamentals of Heat and Mass Transfer*, 6 ed. (John Wiley & Sons, Hoboken, 2007).
104. C. J. Glassbrenner and G. A. Slack, Thermal Conductivity of Silicon and Germanium from 3 K to the Melting Point, *Physical Review*, vol. 134, pp. A1058-A1069, 1964.
105. P. B. Allen and A. Feldman, Thermal Conductivity of Disordered Harmonic Solids, *Physical Review B*, vol. 48, pp. 12581-12588, 1993.
106. S. M. Lee and D. G. Cahill, Heat Transport in Thin Dielectric Films, *Journal of Applied Physics*, vol. 81, pp. 2590-2595, 1997.
107. G. Fischer, H. Hoffmann, and J. Vancea, Mean Free Path and Density of Conductance Electrons in Platinum Determined by the Size Effect in Extremely Thin Films, *Physical Review B*, vol. 22, pp. 6065-6073, 1980.
108. W. Wang and D. G. Cahill, Limits to Thermal Transport in Nanoscale Metal Bilayers Due to Weak Electron-Phonon Coupling in Au and Cu, *Physical Review Letters*, vol. 109, pp. 175503, 2012.
109. X. Liu, J. L. Feldman, D. G. Cahill, R. S. Crandall, N. Bernstein, D. M. Photiadis, M. J. Mehl, and D. A. Papaconstantopoulos, High Thermal Conductivity of a Hydrogenated Amorphous Silicon Film, *Physical Review Letters*, vol. 102, pp. 035901, 2009.

110. D. G. Cahill, M. Katiyar, and J. R. Abelson, Thermal Conductivity of a-Si:H Thin Films, *Physical Review B*, vol. 50, pp. 6077-6081, 1994.
111. Y. He, D. Donadio, and G. Galli, Heat Transport in Amorphous Silicon - Interplay between Morphology and Disorder, *Applied Physics Letters*, vol. 98, pp. 144101, 2011.
112. B. L. Zink, R. Pietri, and F. Hellman, Thermal Conductivity and Specific Heat of Thin-Film Amorphous Silicon, *Physical Review Letters*, vol. 96, pp. 055902, 2006.
113. H. Yang, D. G. Cahill, X. Liu, J. L. Feldman, R. S. Crandall, B. A. Sperling, and J. R. Abelson, Anomalously High Thermal Conductivity of Amorphous Si Deposited by Hot-Wire Chemical Vapor Deposition, *Physical Review B*, vol. 81, pp. 104203, 2010.
114. R. J. Stevens, A. N. Smith, and P. M. Norris, Measurement of Thermal Boundary Conductance of a Series of Metal-Dielectric Interfaces by the Transient Thermoreflectance Technique, *Journal of Heat Transfer*, vol. 127, pp. 315-322, 2005.
115. P. D. Desai, Thermodynamic Properties of Iron and Silicon, *Journal of Physical and Chemical Reference Data*, vol. 15, pp. 967-983, 1986.
116. K. Esfarjani and H. T. Stokes, Method to Extract Anharmonic Force Constants from First Principles Calculations, *Physical Review B*, vol. 77, pp. 144112, 2008.
117. For a range of simple and compound semiconductors at a temperature of 300 K, Lindsay et al. find that using the relaxation time approximation introduces an error of less than 10% compared to an iterative solution of the Boltzmann transport equation (see Ref. 50).
118. M. F. Modest. *Radiative Heat Transfer* (Academic Press, San Diego, CA, 1993).
119. G. Chen and C. L. Tien, Thermal Conductivities of Quantum Well Structures, *Journal of Thermophysics and Heat Transfer*, vol. 7, pp. 311-318, 1993.
120. T. L. Bergman, A. S. Lavine, F. P. Incropera, and D. P. Dewitt. *Fundamentals of Heat and Mass Transfer* 7 ed. (John Wiley & Sons, Hoboken, 2011).
121. T. Klitsner, J. E. VanCleve, H. E. Fischer, and R. O. Pohl, Phonon Radiative Heat Transfer and Surface Scattering, *Physical Review B*, vol. 38, pp. 7576-7594, 1988.

122. R. G. Deissler, Diffusion Approximation for Thermal Radiation in Gases with Jump Boundary Condition, *Journal of Heat Transfer*, vol. 86, pp. 240-246, 1964.
123. G. Chen, Thermal Conductivity and Ballistic-Phonon Transport in the Cross-Plane Direction of Superlattices, *Physical Review B*, vol. 57, pp. 14958, 1998.
124. R. E. Marshak, Note on the Spherical Harmonic Method as Applied to the Milne Problem for a Sphere, *Physical Review*, vol. 71, pp. 443-446, 1947.
125. R. Viskanta and A. L. Crosbie, Radiative Transfer through a Spherical Shell of an Absorbing-Emitting Gray Medium, *Journal of Quantitative Spectroscopy and Radiative Transfer*, vol. 7, pp. 871-889, 1967.
126. S. C. Traugott, An Improved Differential Approximation for Radiative Transfer with Spherical Symmetry, *AIAA Journal*, vol. 7, pp. 1825-1831, 1969.
127. D. A. Broido, L. Lindsay, and A. Ward, Thermal Conductivity of Diamond under Extreme Pressure: A First Principles Study, *Physical Review B*, vol. 86, pp. 115203, 2012.
128. Following the procedure of Ref. 48, the phonon properties needed to predict thermal conductivity are obtained from lattice dynamics calculations and an iterative solution of the Boltzmann transport equation. The required force constants are obtained from density functional theory calculations.
129. E. T. Swartz and R. O. Pohl, Thermal Boundary Resistance, *Review of Modern Physics*, vol. 61, pp. 605-668, 1989.
130. A. Nabovati, D. P. Sellan, and C. H. Amon, On the Lattice Boltzmann Method for Phonon Transport, *Journal of Computational Physics*, vol. 230, pp. 5864-5876, 2011.
131. K. T. Regner, J. P. Freedman, and J. A. Malen, Advances in Studying Phonon Mean-Free-Path-Dependent Contributions to Thermal Conductivity, *Nanoscale and Microscale Thermophysical Engineering*, vol. 19, pp. 183-205, 2015.
132. G. M. Choi, R. B. Wilson, and D. G. Cahill, Indirect Heating of Pt by Short-Pulse Laser Irradiation of Au in a Nanoscale Pt/Au Bilayer, *Physical Review B*, vol. 89, pp. 064307, 2014.

133. J. L. Hostetler, A. N. Smith, D. M. Czajkowsky, and P. M. Norris, Measurement of the Electron-Phonon Coupling Factor Dependence on Film Thickness and Grain Size in Au, Cr, and Al, *Applied Optics*, vol. 38, pp. 3614-3620, 1999.
134. M. I. Kaganov, I. M. Lifshitz, and L. V. Tanatarov, Relaxation between Electrons and Crystalline Lattices, *Soviet Physics JETP*, vol. 4, pp. 173-178, 1957.
135. T. Q. Qiu and C. L. Tien, Short-Pulse Laser Heating on Metals, *International Journal of Heat and Mass Transfer*, vol. 35, pp. 719-726, 1992.
136. G. Tas and H. J. Maris, Electron Diffusion in Metals Studied by Picosecond Ultrasonics, *Physical Review B*, vol. 49, pp. 15046-15054, 1994.
137. L. Jiang and H. Tsai, Improved Two-Temperature Model and Its Application in Ultrashort Laser Heating of Metal Films, *Journal of Heat Transfer*, vol. 127, pp. 1167-1111, 2005.
138. B. Liao, J. Zhou, and G. Chen, Generalized Two-Temperature Model for Coupled Phonon-Magnon Diffusion, *Physical Review Letters*, vol. 113, pp. 025902, 2014.
139. R. B. Wilson, J. P. Feser, G. T. Hohensee, and D. G. Cahill, Two-Channel Model for Nonequilibrium Thermal Transport in Pump-Probe Experiments, *Physical Review B*, vol. 88, pp. 144305, 2013.
140. K. T. Regner, L. C. Wei, and J. A. Malen, Interpretation of Thermoreflectance Measurements with a Two-Temperature Model Including Non-Surface Heat Deposition, *Journal of Applied Physics*, vol. 118, pp. 235101, 2015.
141. A. J. Schmidt, X. Chen, and G. Chen, Pulse Accumulation, Radial Heat Conduction, and Anisotropic Thermal Conductivity in Pump-Probe Transient Thermoreflectance, *Review of Scientific Instruments*, vol. 79, pp. 114902, 2008.
142. R. B. Wilson, B. A. Apgar, L. W. Martin, and D. G. Cahill, Thermoreflectance of Metal Transducers for Optical Pump-Probe Studies of Thermal Properties, *Optics Express*, vol. 20, pp. 28829-28838, 2012.

143. A. Giri, B. Foley, and P. E. Hopkins, Influence of Hot Electron Scattering and Electron-Phonon Interactions on Thermal Boundary Conductance at Metal/Nonmetal Interfaces, *Journal of Heat Transfer*, vol. 136, pp. 092401, 2014.
144. G. L. Eesley, Generation of Nonequilibrium Electron and Lattice Temperatures in Copper by Picosecond Laser Pulses, *Physical Review B*, vol. 33, pp. 2144-2151, 1986.
145. A. Majumdar and P. Reddy, Role of Electron-Phonon Coupling in Thermal Conductance of Metal-Nonmetal Interfaces, *Applied Physics Letters*, vol. 84, pp. 4768-4770, 2004.
146. Y. Hu, L. Zeng, A. J. Minnich, M. S. Dresselhaus, and G. Chen, Spectral Mapping of Thermal Conductivity through Nanoscale Ballistic Transport, *Nature Nanotechnology*, vol. 10, pp. 701-706, 2015.
147. C. Kittel. *Introduction to Solid State Physics* 8 ed. (John Wiley & Sons, Inc., Hoboken, NJ, 2005).
148. J. G. Cook and M. P. van der Meer, The Thermal Conductivity and Electrical Resistivity of Gold from 80 to 340 K, *Canadian Journal of Physics*, vol. 48, pp. 254-263, 1970.
149. J. P. Moore, R. K. Williams, and R. S. Graves, Thermal Conductivity, Electrical Resistivity, and Seebeck Coefficient of High-Purity Chromium from 280 to 1000 K, *Journal of Applied Physics*, vol. 48, pp. 610-617, 1977.
150. M. J. Duggin, Thermal Conductivities of Aluminium and Platinum, *Journal of Physics D: Applied Physics*, vol. 3, pp. L21-L23, 1970.
151. S. D. Brorson, A. Kazeroonian, J. S. Moodera, D. W. Face, T. K. Cheng, E. P. Ippen, M. S. Dresselhaus, and G. Dresselhaus, Femtosecond Room-Temperature Measurement of the Electron-Phonon Coupling Constant  $\Lambda$  in Metallic Superconductors, *Physical Review Letters*, vol. 64, pp. 2172-2175, 1990.
152. A. P. Caffrey, P. E. Hopkins, J. M. Klopff, and P. M. Norris, Thin Film Non-Noble Transition Metal Thermophysical Properties, *Microscale Thermophysical Engineering*, vol. 9, pp. 365-377, 2005.

153. J. Hohlfeld, S.-S. Wellershoff, J. Gdde, U. Conrad, V. Jhnke, and E. Matthias, Electron and Lattice Dynamics Following Optical Excitation of Metals, *Chemical Physics*, vol. 251, pp. 237-258, 2000.
154. B. C. Gundrum, D. G. Cahill, and R. S. Averback, Thermal Conductance of Metal-Metal Interfaces, *Physical Review B*, vol. 72, pp. 245426, 2005.
155. R. Waser and M. Aono, Nanoionics-Based Resistive Switching Memories, *Nature Materials*, vol. 6, pp. 833-840, 2007.
156. U. Russo, D. Ielmini, C. Cagli, and A. L. Lacaita, Filament Conduction and Reset Mechanism in NiO-Based Resistive-Switching Memory (RRAM) Devices, *IEEE Transactions on Electron Devices*, vol. 56, pp. 186-192, 2009.
157. U. Russo, D. Ielmini, C. Cagli, and A. L. Lacaita, Self-Accelerated Thermal Dissolution Model for Reset Programming in Unipolar Resistive-Switching Memory Devices, *IEEE Transactions on Electron Devices*, vol. 56, pp. 193-200, 2009.
158. L. Zhao, J. Zhang, Y. He, X. Guan, H. Qian, and Z. Yu, Dynamic Modeling and Atomistic Simulations of Set and Reset Operations in TiO<sub>2</sub>-Based Unipolar Resistive Memory, *IEEE Electron Device Letters*, vol. 32, pp. 677-679, 2011.
159. D. Ielmini, F. Nardi, and C. Cagli, Universal Reset Characteristics of Unipolar and Bipolar Metal-Oxide RRAM, *IEEE Transactions on Electron Devices*, vol. 58, pp. 3246-3253, 2011.
160. D. Ielmini, Modeling the Universal Set/Reset Characteristics of Bipolar RRAM by Field- and Temperature-Driven Filament Growth, *IEEE Transactions on Electron Devices*, vol. 58, pp. 4309-4317, 2011.
161. G. Bersuker, D. C. Gilmer, D. Veksler, P. Kirsch, L. Vandelli, A. Padovani, L. Larcher, K. McKenna, A. Shluger, V. Iglesias, M. Porti, and M. Nafria, Metal Oxide Resistive Memory Switching Mechanism Based on Conductive Filament Properties, *Journal of Applied Physics*, vol. 110, pp. 124518, 2011.

162. D. B. Strukov, F. Alibart, and R. S. Williams, Thermophoresis/Diffusion as a Plausible Mechanism for Unipolar Resistive Switching in Metal-Oxide-Metal Memristors, *Applied Physics A*, vol. 107, pp. 509-518, 2012.
163. S. Larentis, F. Nardi, S. Balatti, D. C. Gilmer, and D. Ielmini, Resistive Switching by Voltage-Driven Ion Migration in Bipolar RRAM - Part II: Modeling, *IEEE Transactions on Electron Devices*, vol. 59, pp. 2468, 2012.
164. K. Lin, T. Hou, Y. Lee, J. Chang, J. Lin, J. Shieh, C. Chou, T. Lei, W. Chang, W. Jang, and C. Lin, Switching Mode Mechanism in Binary Oxide Resistive Random Access Memory Using Ni Electrode, *Japanese Journal of Applied Physics*, vol. 52, pp. 031801, 2013.
165. D. Ielmini, S. Balatti, and S. Larentis, Filament Evolution During Set and Reset Transitions in Oxide Resistive Switching Memory, *Japanese Journal of Applied Physics*, vol. 52, pp. 04CD10, 2013.
166. B. Govoreanu, S. Clima, I. P. Radu, Y. Chen, D. J. Wouters, and M. Jurczak, Complementary Role of Field and Temperature in Triggering on/Off Switching Mechanisms in Hf/HfO<sub>2</sub> Resistive RAM Cells, *IEEE Transactions on Electron Devices*, vol. 60, pp. 2471-2478, 2013.
167. E. Yalon, I. Riess, and D. Ritter, Heat Dissipation in Resistive Switching Devices: Comparison of Thermal Simulations and Experimental Results, *IEEE Transactions on Electron Devices*, vol. 61, pp. 1137-1144, 2014.
168. S. Ambrogio, S. Balatti, D. C. Gilmer, and D. Ielmini, Analytical Modeling of Oxide-Based Bipolar Resistive Memories and Complementary Resistive Switches, *IEEE Transactions on Electron Devices*, vol. 61, pp. 2378-2386, 2014.
169. L. Larcher, O. Pirrotta, F. M. Puglisi, A. Padovani, P. Pavan, and L. Vandelli, Progresses in Modeling HfO<sub>x</sub> RRAM Operations and Variability, *ECS Transactions*, vol. 64, pp. 49-60, 2014.
170. T. Fang, S. Kaza, S. Haddad, A. Chen, Y. Wu, Z. Lan, S. Avanzino, D. Liao, C. Gopalan, S. Choi, S. Mahdavi, M. Buynoski, Y. Lin, C. Marrian, C. Bill, M. VanBuskirk, and M. Taguchi. in *IEDM Tech. Dig.* 789-792.

171. D. Kwon, K. M. Kim, J. H. Jang, J. M. Jeon, M. H. Lee, G. H. Kim, X. Li, G. Park, B. Lee, S. Han, M. Kim, and C. S. Hwang, Atomic Structure of Conducting Nanofilaments in TiO<sub>2</sub> Resistive Switching Memory, *Nature Nanotechnology*, vol. 5, pp. 148-153, 2010.
172. W. R. Thurber and A. J. Mante, Thermal Conductivity and Thermoelectric Power of Rutile (TiO<sub>2</sub>), *Physical Review*, vol. 139, pp. A1655-A1665, 1965.
173. C. Hua and A. J. Minnich, Analytical Green's Function of the Multidimensional Frequency-Dependent Phonon Boltzmann Equation, *Physical Review B*, vol. 90, pp. 214306, 2014.
174. K. T. Regner and J. A. Malen, Nondiffusive Thermal Transport Increases Temperature Rise in RRAM Filaments, *IEEE Electron Device Letters*, vol.
175. Y. S. Touloukian, R. W. Powell, C. Y. Ho, and P. G. Klemens. *Thermophysical Properties of Matter* (IFI/Plenum, New York, 1970).
176. B. Vermeersch, C. J., N. Mingo, and A. Shakouri, Superdiffusive Heat Conduction in Semiconductor Alloys -- I. Theoretical Foundations, *arXiv:1406.7341*, vol., 2014.
177. B. Vermeersch, A. M. S. Mohammed, G. Pernot, Y. R. Koh, and A. Shakouri, Superdiffusive Heat Conduction in Semiconductor Alloys -- II. Truncated Levy Formalism for Experimental Analysis, *arXiv:1406.7342*, vol., 2014.
178. H. Lee, D. Vashaee, D. Z. Wang, M. S. Dresselhaus, Z. F. Ren, and G. Chen, Effects of Nanoscale Porosity on Thermoelectric Properties of SiGe, *Journal of Applied Physics*, vol. 107, pp. 094308, 2010.
179. T. Q. Qiu and C. L. Tien, Size Effects on Nonequilibrium Laser Heating of Metal Films, *Journal of Heat Transfer*, vol. 115, pp. 842-847, 1993.
180. P. E. Hopkins, P. M. Norris, L. M. Phinney, S. A. Policastro, and R. G. Kelly, Thermal Conductivity in Nanoporous Gold Films During Electron-Phonon Nonequilibrium, *Journal of Nanomaterials*, vol. 2008, pp. 1-7, 2008.

181. P. E. Hopkins, J. R. Serrano, L. M. Phinney, H. Li, and A. Misra, Boundary Scattering Effects During Electron Thermalization in Nanoporous Gold, *Journal of Applied Physics*, vol. 109, pp. 013524, 2011.
182. M. C. Langner, C. L. S. Kantner, Y. H. Chu, L. M. Martin, P. Yu, R. Ramesh, and J. Orenstein, Effective Thermal Boundary Resistance from Thermal Decoupling of Magnons and Phonons in SrRuO<sub>3</sub> Thin Films, *Physical Review B*, vol. 82, pp. 054425, 2010.
183. G. T. Hohensee, R. B. Wilson, J. P. Feser, and D. G. Cahill, Magnon-Phonon Coupling in the Spin-Ladder Compound Ca<sub>9</sub>La<sub>5</sub>Cu<sub>24</sub>O<sub>41</sub> Measured by Time-Domain Thermoreflectance, *Physical Review B*, vol. 89, pp. 024422, 2014.
184. J. P. Freedman, R. F. Davis, and J. A. Malen, Nondiffusive Electron Transport in Metals Interpreted by Two-Temperature Boltzmann Transport Equation Analyses of Thermoreflectance Experiments, *submitted*, vol.
185. J. H. Seol, I. Jo, A. L. Moore, L. Lindsay, Z. H. Aitken, M. T. Pettes, X. Li, Z. Yao, R. Huang, D. A. Broido, N. Mingo, R. S. Ruoff, and L. Shi, Two-Dimensional Phonon Transport in Supported Graphene, *Science*, vol. 328, pp. 213-216, 2010.
186. K. Seibert, G. C. Cho, W. Kutt, H. Kurz, D. H. Reitze, J. I. Dadap, H. Ahn, M. C. Downer, and A. M. Malvezzi, Femtosecond Carrier Dynamics in Graphite, *Physical Review B*, vol. 42, pp. 2842-2851, 1990.
187. K. F. Mak, C. H. Lui, and T. F. Heinz, Measurement of the Thermal Conductance of the Graphene/SiO<sub>2</sub> Interface, *Applied Physics Letters*, vol. 97, pp. 221904, 2010.